Geophysical Journal International

Geophys. J. Int. (2021) **227,** 439–471
Advance Access publication 2021 June 09
GJI Geodynamics and tectonics

https://doi.org/10.1093/gji/ggab223

Longevity of small-scale ('baby') plumes and their role in lithospheric break-up

Alexander Koptev [1], Sierd Cloetingh [2] and Todd A. Ehlers [1]

[1] *Department of Geosciences, University of Tübingen, Tübingen* 72074, *Germany. E-mail: alexander.koptev@ifg.uni-tuebingen.de*
[2] *Tectonics Research Group, Utrecht University, Utrecht* 3584 *CS, Netherlands*

Accepted 2021 June 7. Received 2021 May 20; in original form 2021 February 3

SUMMARY

Controversy between advocates of 'active' (plume-activated) versus 'passive' (driven by external tectonic stresses) modes of continental rifting and break-up has persisted for decades. To a large extent, inconsistencies between observations and models are rooted in the conceptual model of plumes as voluminous upwellings of hot material sourced from the deep mantle. Such large-scale plumes are expected to induce intensive magmatism and topographic uplift, thereby triggering rifting. In this case of an 'active' rifting-to-break-up system, emplacement of plume-related magmatism should precede the onset of rifting that is not observed in many rifted continental margins, thus providing a primary argument in favour of an antiplume origin for continental break-up and supercontinent fragmentation. However, mantle plumes are not restricted to whole-mantle ('primary') plumes emanating from the mantle-core boundary but also include 'secondary' plumes originating from the upper mantle transition zone or shallower. Over the last decades a number of such 'secondary' plumes with horizontal diameters of only ∼100–200 km (therefore, sometimes also called 'baby' plumes) have been imaged in the upper mantle below Europe and China. The longevity of such small-scale plumes and their impact on geodynamics of continental break-up have so far not been explored. We present results of a systematic parametrical analysis of relatively small thermal anomalies seeded at the base of the lithosphere. In particular, we explore the effects of variations in initial plume temperature ($T = 1500$–$1700\,^{\circ}C$) and size (diameter of 80–116 km), characteristics of the overlying lithosphere (e.g. 'Cratonic', 'Variscan', 'Mesozoic' and oceanic) and intraplate tectonic regimes (neutral or far-field extension of 2–10 mm yr^{-1}). In tectonically neutral regimes, the expected decay time of a seismically detectable 'baby'-plume varies from ∼20 to >200 Myr and is mainly controlled by its initial size and temperature, whereas the effect of variations in the thermotectonic age of the overlying lithosphere is modest. These small but enduring plumes are able to trigger localized rifting and subsequent continental break-up occurring from ∼10 to >300 Myr after the onset of far-field extension. Regardless of the thermomechanical structure of the lithosphere, relatively rapid (tens of Myr) break-up (observed in models with a hot plume and fast extension) favours partial melting of plume material. In contrast, in the case of a long-lasting (a few hundreds of Myr) pre-break-up phase (relatively cold plume, low extension rate), rifting is accompanied by modest decompressional melting of only 'normal' sublithospheric mantle. On the basis of the models presented, we distinguish two additional modes of continental rifting and break-up: (1) 'semi-active' when syn-break-up magmatism is carrying geochemical signatures of the deep mantle with deformation localized above the plume head not anymore connected by its tail to the original source of hot material and (2) 'semi-passive' when the site of final lithospheric rupture is controlled by a thermal anomaly of plume origin but without invoking its syn-break-up melting. These intermediate mechanisms are applicable to several segments of the passive continental margins formed during Pangea fragmentation.

Key words: Continental tectonics: extensional; Dynamics of lithosphere and mantle; Hotspots; Intra-plate processes; Large igneous provinces; Rheology: crust and lithosphere.

1 INTRODUCTION

Most studies devoted to the interaction of the Earth's lithosphere with mantle hotspots are traditionally focused on classic Morgan-type plumes originating from the lower mantle (Morgan 1971). However, such 'primary' superplumes can stagnate beneath the 660 km phase change boundary and create numerous thermal perturbations in the upper mantle corresponding to so-called 'secondary' plumes (Courtillot *et al.* 2003). According to predictions by Griffiths & Campbell (1990) and Campbell & Griffiths (1990), mantle upwelling from the core–mantle boundary should develop plume heads of up to ∼2000 km in width after it flattens into a 'pancake' shape beneath the lithosphere (Stern *et al.* 2020), whereas the heads of plumes originating within the upper mantle would have a characteristic diameter of ∼600 km. Over the last decades a number of much smaller plumes with horizontal size of only ∼100–200 km ('baby' plumes) have been detected in the upper mantle below Europe (Granet *et al.* 1995; Ritter *et al.* 2001; Babuška *et al.* 2008) and China (Tang *et al.* 2014; Xia *et al.* 2016; Kuritani *et al.* 2017).

Despite the detected presence of these 'baby' plumes in various areas around the globe (Ritter 2007; Xia *et al.* 2016) and their potential importance for lithosphere break-up (Gac & Geoffroy 2009), a systematic and comprehensive quantitative analysis of their properties and impact on the overlying lithosphere has been lacking so far. The bulk of previous numerical and analogue modelling studies has explored consequences of plume-lithosphere interactions in very different tectonic settings, including rifting/continental break-up (Brune *et al.* 2013; Burov & Gerya 2014; Koptev *et al.* 2015, 2016; Beniest *et al.* 2017a, 2017b), subduction initiation (Burov & Cloetingh 2010; Gerya *et al.* 2015; Baes *et al.* 2020a, b, 2021; Cloetingh *et al.* 2021) and microcontinental separation (Dubinin *et al.* 2018; Koptev *et al.* 2019; Neuharth *et al.* 2021). However, all these studies have till now focused on relatively large (>>100 km in the resulting horizontal size of the 'pancake'-shaped head) mantle plume anomalies.

Here we provide the first systematic analysis of small thermal anomalies ('baby' plumes). In our experiments 'baby' plumes are initially seeded just below the bottom of the lithosphere. In this respect, it is important to note that the source and emplacement mechanism of these small-scale thermal anomalies remains beyond the scope of our study. We intentionally focus on the consequences of the implementation of the 'baby' plumes rather than on the scenarios for their origin, thus enabling a broad interpretation and application of obtained modelling results. First, we explore the longevity of 'baby' plumes of different temperatures and sizes seeded underneath different types of overlying lithosphere (i.e. lithospheres of different thicknesses and different thermorheological structure). Subsequently, we investigate the impact of 'baby' plumes on location, timing and style (magmatic/amagmatic) of the break-up when the overlying lithosphere is subjected to external tectonic extension. In our study, we pay particular attention to the temporal evolution of the width of the thermal anomaly that permits us to test seismic detectability of the 'baby' plumes over the modelled time period.

Our results are not only relevant for small plume anomalies presently detected in Europe and China, but also important for possible scenarios for Pangea fragmentation complementing existing end-member views on 'active' and 'passive' rifting and break-up. In particular, we resolve apparent contradictions and disputes on non-plume and plume-driven break-up by introducing intermediate ('semi-active' and 'semi-passive') modes which could be viable mechanisms for the formation of several modern continental rifted margins.

2 BACKGROUND

The origin of stresses in the lithosphere plays a key role in our understanding of geodynamic and geologic processes. Since the acceptance of continental drift (Holmes 1965) and plate tectonics (Wilson 1966) in the 1960s, three main sources have been recognized for plate motions and stresses in the lithosphere, including: (1) horizontal tractions at the base of the lithosphere arising from mantle convective flow ('basal drag'), (2) forces exerted by cold, dense oceanic plates sinking into the mantle at a subduction zone due to its own weight ('slab pull') and (3) lateral variations in the lithosphere's gravitational potential energy (topographic driving forces; e.g. 'ridge push'). These mechanisms have been thoroughly explored by global (Forsyth & Uyeda 1975; Harper 1975; Richardson *et al.* 1979; Coblentz *et al.* 1994; Conrad & Lithgow-Bertelloni 2002; Lithgow-Bertelloni & Guynn 2004; Bird *et al.* 2008; Koptev & Ershov 2010; Naliboff *et al.* 2012; Yang & Gurnis 2016) and regional (Wortel & Cloetingh 1985; Cloetingh & Wortel 1986; Richardson & Reding 1991; Coblentz & Sandiford 1994; Coblentz & Richardson 1996; Flesch *et al.* 2001; Liu & Bird 2002; Reynolds *et al.* 2002; Burbidge 2004; Rajabi *et al.* 2017; Tunini *et al.* 2017) numerical modelling. Nevertheless, the driving mechanism of plate tectonics still remains controversial. In particular, the role of upwelling mantle flow in the dynamics of continental rifting and break-up systems (namely, 'active' versus 'passive' rifting) is a long-debated topic (e.g. Fitton 1983; Foulger *et al.* 2000; Foulger & Hamilton 2014). In the 'active' or plume-assisted scenario (Morgan 1971; Hill 1991), rifting occurs as a result of active mantle diapirs rising through the mantle when extension is imparted by (1) horizontal viscous forces caused by radial flow of the plume head below the lithosphere and (2) buoyancy forces associated with topographic uplift over a plume (Westaway 1993). On the contrary, the 'passive' scenario (McKenzie 1978) calls for the processes originating far away from the rifting zone when tensional far-field forces (e.g. remote pull of the subducting slab) are transmitted through the lithospheric plate causing its extension and thinning within a localized area, while upwelling of underlying mantle and associated decompressional melting are both a passive consequence of rifting-related stretching of the lithosphere.

This controversy between 'active' and 'passive' modes of rifting becomes even more critical when considering mechanisms of supercontinent break-up, a key component of the Earth's tectonic and geodynamic evolution (Wilson 1966; Bradley 2011; Yoshida & Santosh 2011). On the one hand, slab rollback is proven as a viable mechanism to induce extension in the overriding plate (e.g. Schellart & Moresi 2013; Holt *et al.* 2015; Yoshida 2017), whereby the dragging force from slab retreat in oceanic subduction zones surrounding a supercontinent (Collins 2003; Zhong *et al.* 2007) has been proposed as the main driving mechanism for its dispersal (Bercovici & Long 2014). On the other hand, extension caused by subduction retreat has been shown to be focused along the marginal zones only while having far less impact on the interior of the supercontinent (Zhang *et al.* 2018). According to this (Zhang *et al.* 2018) and other recent numerical models of global mantle convection (Huang *et al.* 2019; Dang *et al.* 2020), the main reason for supercontinent break-up resides in the push by the rise of mantle plumes from the subcontinental mantle (Li *et al.* 1999, 2008). Thick mid-Jurassic oceanic crust in the Atlantic and Indian oceans is also

indicative of hotter upper mantle underneath Pangea before the disintegration of this supercontinent (Lenardic 2017; Van Avendonk *et al.* 2017). As a step to reconcile these end-member views on the dominant force responsible for supercontinent dispersal it has been demonstrated that deeply subducting slabs might penetrate into the lower mantle and trigger upwelling and return flow that results in mantle superplumes (Zhang *et al.* 2010; Heron *et al.* 2015; Dal Zilio *et al.* 2018).

The timing and volume of rift-related magmatism are traditionally considered as a primary proxy for identification of the 'active' component associated with mantle plume upwelling (Şengör & Burke 1978). As has been noted for almost five decades (Scrutton 1973), continental break-up in different parts of the Pangea supercontinent was shortly preceded by intensive and massive magmatic events leading to the formation of so-called Large Igneous Provinces (LIPs). LIPs are large volumes of predominantly mafic rocks that distinguish themselves from magma generated by processes at plate boundaries (Coffin & Eldholm 1994; Bryan & Ernst 2008; Ernst 2014). Based on an assumption of a genetic link between voluminous magmatism and the upwelling of hot mantle material (e.g. Richards *et al.* 1989), plume impingement has been postulated as a pre-requisite for continental break-up and subsequent formation of major oceanic basins during Pangea dispersal (Courtillot *et al.* 1999). However, at the same time it was found that presumably 'active' break-up of Pangea accompanied by LIP emplacement is frequently preceded by long-lasting (up ~200 Myr in the case of the North Atlantic) phases of almost amagmatic (and, therefore, 'passive') rifting (Ziegler & Cloetingh 2004, and references herein). Therefore, according to the classic interpretation by Şengör & Burke (1978), such a relative timing of rifting and volcanism (major rift formation predates magmatic activity) corresponds to a 'passive' scenario when extension is imparted by the horizontal movement of plates. Moreover, both location and orientation of the Pangea break-up axes frequently follow pre-existing orogenic sutures (Buiter & Torsvik 2014) which are mechanically weaker relative to the cratons surrounding them (Cloetingh *et al.* 1995; Ryan & Dewey 1997). These findings are complemented by suggestions on the presence of a sufficiently low (50–100 K) potential temperature anomaly beneath Iceland (Foulger & Anderson 2005), the region where a seismically detected (Bijwaard & Spakman 1999; Amaru 2007; Rickers *et al.* 2013) thermal plume rising from the deep mantle has been almost universally involved (e.g. Campbell & Davies 2006; Campbell 2007) to explain both massive magmatism (Saunders *et al.* 1997; Storey *et al.* 2007) and onshore and offshore topographic uplift (Rohrman *et al.* 1995; Rohrman & van der Beek 1996; Japsen & Chalmers 2000; Koptev *et al.* 2017) along the adjacent North Atlantic passive margins. The aforementioned contradictions to an idealized plume-impingement model inspire a fundamental reappraisal of the causes for (super)continental break-up and, in particular, their link to LIPs (Peace *et al.* 2020). This has fueled 'antiplume' conceptions and brought several authors to argue in favour of shallow tectonics (i.e. 'passive') mechanisms during break-up of different Pangea segments including those associated with LIPs and traditionally attributed to 'active' rifting mechanisms: break-up in North, Central and South Atlantic and in East and West Gondwana (Lundin & Doré 2005; Peace *et al.* 2020, and references herein).

However, all these 'antiplume'/'shallow tectonics' scenarios and views are in general at odds with findings from modern seismic tomography showing evidence for the widespread presence of low velocity anomalies extending down to the core–mantle boundary (Romanowicz & Gung 2002; Montelli *et al.* 2006; French & Romanowicz 2015; Davaille & Romanowicz 2020). In the proximity of these plumes mid-ocean ridges exhibit a greater overall content of volatiles and excess bathymetry (Gibson & Richards 2018). Moreover, the geochemistry of LIPs has demonstrated a major contribution of undepleted material derived from primitive, undegassed reservoirs located in the lowermost mantle (Jackson *et al.* 2010, 2017). Finally, the fact that LIPs occur close to final break-up (Buiter & Torsvik 2014), and are frequently preceded by long-lasting amagmatic phases of 'passive' rifting (Ziegler & Cloetingh 2004), cannot disprove a plume-triggered scenario when a mantle plume is emplaced below a lithosphere already extended over a wide area (Reemst & Cloetingh 2000) localizing distributed deformation in a narrow zone of break-up. By means of ultra-high resolution 3-D thermomechanical modelling, it has been shown that in the case of a combined 'active-passive' scenario initial impingement of a mantle plume can precede final break-up of the overlying lithosphere by up to 100 Myr under the condition of ultra-slow (half-rate of <3 mm yr^{-1}) tectonic extension (Koptev *et al.* 2018a), thus reconciling documented evidence for syn-break-up magmatism of deep-mantle geochemical signatures and long-lasting prior phases of quasi-amagmatic rifting.

Much of the focus in the current discussion on the impact of mantle plumes and their role in (super)continental break-up and LIPs formation has been restricted to the classical plume concept when a large and continuous plume body rises through the entire mantle from the core–mantle boundary (Morgan 1971; Koppers *et al.* 2021). As originally discovered by Burke & Torsvik (2004) and subsequently confirmed by statistical analysis by Doubrovine *et al.* (2016), the sources of LIPs-related plumes are not randomly distributed over the core–mantle boundary but, in contrast, are preferentially localized along the edges of two large low shear wave velocity provinces (LLSVPs) located beneath Africa and the Pacific Oceanic and christened by Kevin Burke as 'TUZO' and 'JASON', respectively (Burke 2011). The plumes arising from LLSVP borders are thought to be triggered by subducted slabs sinking in the lowermost mantle (Steinberger & Torsvik 2012). Alternatively, they could be just a result of the insulating thermal effect of LLSVPs making the conductive core–mantle heat transfer focused at their boundaries (Niu 2018). Regardless of the underlying mechanism, established correlations between reconstructed eruption sites of LIPs and kimberlites with LLSVP margins are in support of long-lived existence and fixed locations of LLSVPs during the last 200 Myr (Torsvik *et al.* 2006), 300 Myr (Torsvik *et al.* 2008) and possibly for the entire Phanerozoic (Torsvik *et al.* 2010, 2014) or even since early (>2 Ga) Earth history (Dziewonski *et al.* 2010; Burke 2011; Torsvik *et al.* 2016).

However, apart from this 'Burke Earth' end-member model (Torsvik *et al.* 2016) which is focused on first-order (or 'primary') hotspots originating from the deep mantle (Fig. 1a1), other types of plumes have been proposed (Courtillot *et al.* 2003). In particular, a 'primary' superplume stagnated at the base of, or within, the upper-lower mantle transition zone (MTZ: 410–660 km; Helffrich & Wood 2001) can create numerous thermal perturbations extending throughout the upper mantle, forming so-called 'secondary' plumes which can further generate or contribute to the shallow 'tertiary' hotspots (Fig. 1a2). In contrast to the 'primary' and 'secondary' plumes continuously fed from below (whether from LLSVPs at the core–mantle boundary or from bunched plume material at 660 km depth), 'tertiary' hotspots are traditionally thought to have an exclusively superficial origin being linked to tensile stresses and cracking in the lithosphere and decompressional melting (Courtillot *et al.* 2003; Torsvik *et al.* 2016). In another end-member scenario

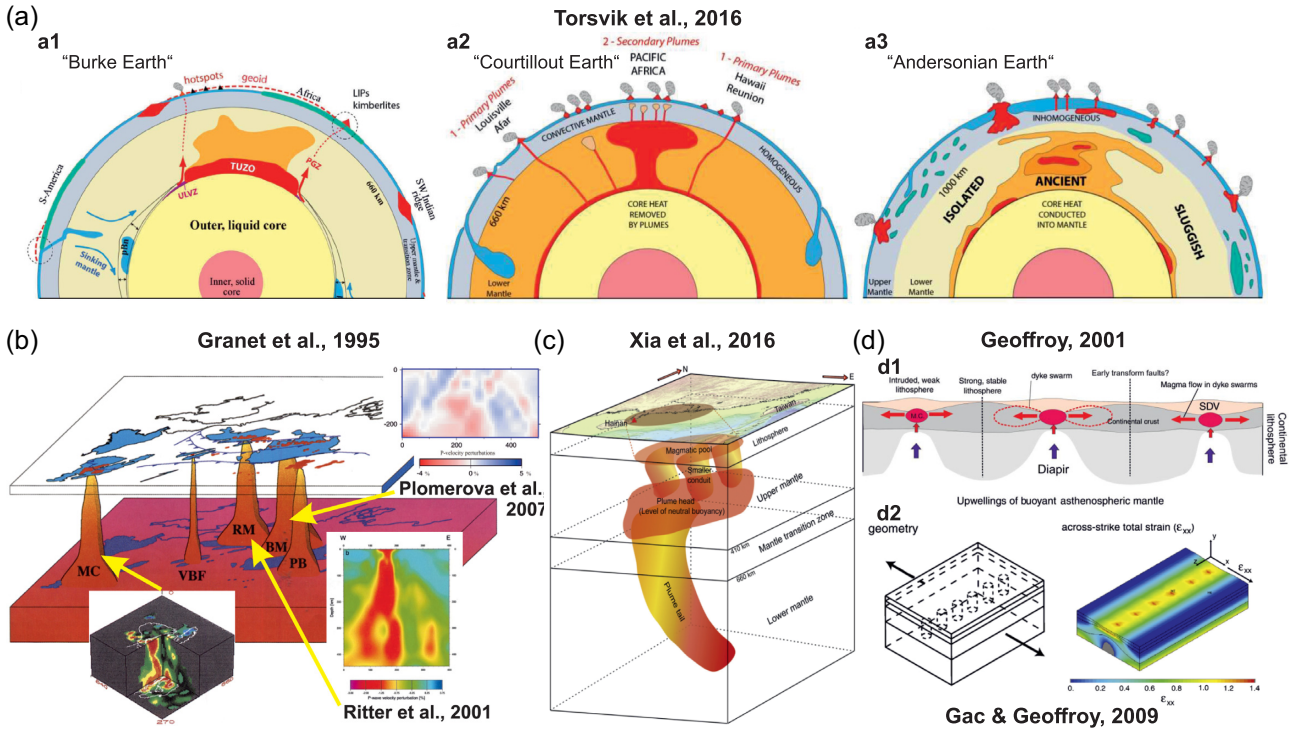

Figure 1. (a) Different models of internal Earth structure (from Torsvik *et al.* 2016): (a1) 'Burke Earth' with only 'primary' plumes derived from margins of thermochemical piles (LLSVPs) at core–mantle boundary (Burke 2011); (a2) 'Courtillot Earth' with three types of 'primary', 'secondary' and 'tertiary' plumes (Courtillot *et al.* 2003); and (a3) 'Andersonian Earth' with only superficial 'tertiary' hotspots (Anderson 2000). Abbreviations: pBn, post-Bridgmentite; PGZ, plume generation zone; ULVZ, ultra-low velocity zone. (b) Upwelling of small-scale mantle plumes ('baby' plumes) below European lithosphere (from Granet *et al.* 1995). Insets are images from seismic tomography for French Massif Central (from Granet *et al.* 1995), Rhenish Massif/Eifel volcanic area (from Ritter *et al.* 2001) and Bohemian Massif/Eger rift (from Plomerova *et al.* 2007). Abbreviations: MC, Massif Central; VBF, Vosges-Black Forest; RM, Rhenish Massif; BM, Bohemian Massif; PB, Pannonian Basin. Areas in blue and red are Variscan basement massifs and Tertiary–Quaternary volcanic fields, respectively. (c) Scenario illustrating hotspot organization in the Earth's mantle beneath southernmost China (from Xia *et al.* 2016); (d) Structure and models of volcanic passive margins: (d1) schematic cross-section along a volcanic passive margin: tectonic and magmatic segmentation controlled by asthenospheric diapirs (from Geoffroy 2001). Abbreviations: M.C., magma chamber; SDV, seaward-dipping volcanic formations; (d2) initial geometry (left-hand panel) and results (right-hand panel) of numerical modelling of the strain distribution in the lithosphere containing six aligned soft points corresponding to thermal instabilities related to small-scale mantle diapirs (from Gac & Geoffroy 2009).

corresponding to the so-called 'Andersonian Earth' (Anderson 2000) where any communication between the upper and lower mantle is excluded, these 'tertiary' hotspots become the only source of intraplate magmatism (Fig. 1a3).

Numerous examples can be given for each category of mantle upwelling and associated thermal perturbations in the mantle (Courtillot *et al.* 2003). Interaction of 'primary' plumes with oceanic lithosphere is known to generate hotspot tracks characterized by the time progression of magmatism as a result of tectonic plates motion over large-scale columnar upwelling in the mantle (Wilson 1963; Morgan 1972; Steinberger *et al.* 2004; Doubrovine *et al.* 2012; Torsvik *et al.* 2017). Within continents, the sudden onset of continental flood volcanism over a large area of up to 10^6 km^2 attributed to melting of hot material from plume sources (Campbell & Griffiths 1990) is usually manifested in tens of Myr after initial plume-related surface uplift (Rainbird & Ernst 2001) of ~0.5–2 km (Griffiths *et al.* 1989; Farnetani & Richards 1994; Şengör 2001). This rapid, transient domal uplift above the plume axis is followed by subsidence (Burov & Cloetingh 2009; Friedrich *et al.* 2018; Göğüş 2020) due to flattening of the plume head below the base of the lithosphere (White & McKenzie 1989). The radial flow away from a plume's axis leads to a mushroom-like shape of the plume: a large disk-shaped head (~1000 km in diameter) with a narrow long tail (Campbell & Davies 2006; Campbell 2007). Note that a symmetrical configuration might be complicated by preexisting zones of lithospheric thinning acting as sinks for a buoyant mantle plume (Sleep 1996, 1997). The resulting long-distance (>1000 km) propagation of hot plume material along the elevated lithosphere–asthenosphere boundary is reflected in alkaline volcanism (Ebinger & Sleep 1998) and regional uplift (Koptev *et al.* 2017) in the areas remote from the point of initial plume impingement. Given this strong filter of mantle plume activity by thick continental lithosphere, evidence for hotspot chains within continents is seldom. The commonly cited example of the Yellowstone hotspot (Smith *et al.* 2009) demonstrates a time-progressive track in a direction that is not consistent with North American plate motion (Jordan *et al.* 2004; Meigs *et al.* 2009; Wagner *et al.* 2010). The first confirmed example of a continental hotspot track aligned with plate motion has been recently detected in the eastern United States, where a linear (~200–250 km wide) seismic anomaly with reduced *P*-wave velocity in the lower lithosphere (Chu *et al.* 2013) has been formed as a result of the westward passage of the North American Plate (Cox & Arsdale 2002) over a 'primary', deep-sourced thermal mantle plume presently located beneath the Bermuda-Sargasso Sea region (Li *et al.* 2020). Based on combined analysis of seismic tomography, uplift, volcanism and heat-flow data, three trajectories of separate hotspots have been also detected

below Arabia and the Horn of Africa (Vicente de Gouveia *et al.* 2018). In this case, however, these tracks correspond to distinct 'secondary' plumes (Afar, East-Africa and Lake-Victoria) originated from the same deep-sourced (super)plume which raised from LLSVPs but subsequently stagnated below the upper mantle transition zone at 660 km (Vicente de Gouveia *et al.* 2018). Similar 'secondary' structures have been detected in the upper mantle beneath Europe by seismologists during the last decades (Granet *et al.* 1995; Ritter *et al.* 2000, 2001; Plomerova *et al.* 2007; Babuška *et al.* 2008; Fig. 1b). Given that they are characterized by extremely small horizontal sizes of ∼100 km, these structures have been dubbed 'baby' plumes (Cloetingh & Ziegler 2009). Apart from their small size, the 'baby' plumes also have a relatively small seismic velocity contrast (< 3 per cent) with respect to the surrounding mantle and, therefore, their detection requires specifically designed seismological experiments on a regional and local scale (Ritter 2005). The origin of these small-scale thermal anomalies characterized by a modest excess of potential temperature of ∼150–200 °C remains controversial. Based on a global tomographic model, a deep magma source in the lower mantle has been proposed (Goes *et al.* 1999, 2000). In contrast, the regional studies in the French Massif Central (Granet *et al.* 1995, Sobolev *et al.* 1997) and the Eifel volcanic fields of northwestern Germany (Ritter *et al.* 2000, 2001) provide evidence for the tail of a mantle plume extending only to a depth of 300–400 km, thus indicating their shallower origin from the MTZ. It should be noted, however, that the plume tails in the MTZ and deeper may not be visible in seismic tomography data because of their narrow width. The likely presence of plume conduits is indirectly confirmed by volcanic rocks and gases in these regions which often have the geochemical signatures of a deep source in the lower mantle (Hoernle *et al.* 1995; Buikin *et al.* 2005; Caracausi *et al.* 2016), although the interpretation of data is ambiguous (Lustrino & Carminati 2007). For the western Bohemian Massif, a low-velocity anomaly beneath the Tertiary Eger Rift system is confined to a depth of 250 km (Plomerová *et al.* 2007, 2016; Babuška *et al.* 2008; Koulakov *et al.* 2009). This anomaly and associated magmatism (Ulrych *et al.* 2011), therefore, could be attributed to the category of 'tertiary' hotspots which are presumably related to shallow tectonic processes and upwelling of the lithosphere–asthenosphere boundary. However, a possible link to deeper sources (and thus belonging to the category of 'secondary' plumes) is not to be excluded: the isolated bodies of thermal anomalies presently residing at shallow depths might only have lost their initial connection with the deep source of hot material either due to exhaustion of this source or just because of plate movement. In the latter case, the head of such 'secondary' plume has been attached to the bottom of the lithosphere and subjected to lateral shift with respect to the feeding channel in the sublithospheric mantle (i.e. plume tail).

More recently, seismological evidence for 'baby'-plume-like structures has been also obtained in the Western Pacific and adjacent areas of mainland China (Tang *et al.* 2014; Xia *et al.* 2016; Kuritani *et al.* 2017). In particular, a 'primary' plume with an extending columnar tail beneath southernmost China (Hainan Island area) appears to spread laterally within the MTZ, thus ponding at the level of the lower part of the upper mantle. This 'plume head' is seated deeper than 'normal' 'primary' plumes (which are usually flattened below the lithospheric bottom), and is further decomposed into smaller separate patches (Xia *et al.* 2016), identical to 'secondary' 'baby' plumes proposed by Granet *et al.* (1995) for the European region (compare Figs 1b and c). Similar finger-like upper mantle structures have been also detected below northeast China near the border between China and North Korea (Tang *et al.* 2014). There, the ascent of the mantle plumes has been presumably caused by decompressional melting of nearly water-saturated material (so-called 'hydrous plumes'; Kuritani *et al.* 2017, 2019) in the MTZ (Fei *et al.* 2017; Fomin & Schiffer 2019; Long *et al.* 2019) where an excess of fluids is commonly attributed to subduction of oceanic fluid-rich plates and their subsequent accumulation at the 660 km discontinuity boundary (Hetényi *et al.* 2009; Kovács *et al.* 2020). Alternatively, widespread intraplate volcanism in northeast China above a stagnated Pacific slab has been explained by a return flow of sublithospheric mantle material entrained beneath the subducting plate and then escaped through a gap in the slab resulting in focused 'baby'-plume-like upwelling in the upper mantle (Tang *et al.* 2014). It is important to note that European 'baby' plumes are developed in conjunction with the Cenozoic rift system (Bourgeois *et al.* 2007) formed within a continental foreland on the subducting plate (Ziegler & Dèzes 2007). This indicates, therefore, that emplacement of small-scale mantle anomalies might occur in a broad spectrum of possible geodynamic settings across the subduction zone from foreland (Europe) to hinterland (China).

Another observation that is known since almost two decades, but so far not taken into consideration in the 'baby' plumes context, is that volcanic passive margins are frequently punctuated every 50–150 km by long-lived igneous centers (Geoffroy 2001; Fig. 1d1). These are related to large crustal magma chambers developed over mantle diapirs which have been interpreted as a consequence of small-scale convection cells at the level of the shallowest asthenosphere (Geoffroy 2005). In view of their small (∼100 km) characteristic size and moderate (∼150–200 K) temperature contrast it seem to be reasonable to consider the mantle diapirs described by Geoffroy (2001) as the equivalent of the 'baby' plumes discussed above. It is also noteworthy that despite the relatively shallow depth extent of these mantle diapirs, the question on the origin of such 'baby' plumes of 'tertiary' class remains open and a potential role of a deep mantle source in their establishment is feasible.

Despite their modest dimension and magnitude and regardless of the mechanism of their emplacement, thermal instabilities related to 'baby' plumes are known to have a pronounced expression not only in magmatism (Wilson & Downes 1992) and vertical surface motions (Guillou-Frottier *et al.* 2007; Fauquette *et al.* 2020; Kreemer *et al.* 2020) but also in the rheological structure of the overlying lithosphere (Garcia-Castellanos *et al.* 2000; Tesauro *et al.* 2009a, b). This appears to be also the case for asthenospheric diapiric instabilities emplaced in volcanic rifted margin settings (Geoffroy 2001). There, the thermal consequences of mantle diapirs (or 'baby' plumes as we call them here) lead to the development of the rheological soft-points which expectedly concentrate the regional extension around them. As shown by analogue (Callot *et al.* 2002) and numerical (Gac & Geoffroy 2009) modelling, initially isolated mantle soft points produce not only simultaneous localized extension over them but also, given their narrow spacing, interconnect zones of localized stretching ultimately leading to continental break-up and volcanic passive margin formation (Fig. 1d2).

Below two fundamental aspects are central. The first principal question concerns the preservation in time of the plumes of different scales after their emplacement. Because of long-term stability of LLSVPs (from 200 Myr to >2 Gyr; see Burke 2011; Torsvik *et al.* 2016), 'primary' large-scale plumes can be preserved and remain seismologically detectable during hundreds of Myr. 'Primary' plumes of intermediate size potentially resulting in 'hidden' hotspot tracks (as, for example, detected in the eastern USA by a few hundred km wide corridor of low seismic velocities in the lithospheric

mantle, see Chu *et al.* 2013) can survive more than 100 Myr according to thermochemical numerical models by Yang & Leng (2014). In contrast, small-scale mantle anomalies of 'secondary'/'tertiary' category are known to produce no hotspot tracks associated with the volcanism (e.g. Ritter *et al.* 2000, 2001) and the life span of these 'baby' plumes is still an open question. Although seismological evidence apparently underpins their existence, it remains unclear whether these tomographic snapshots are related to very recent emplacement or whether these 'baby' plumes have a life span long enough to still allow their detection for tens of million years or even longer after impingement. The second key question concerns the consequences of the small and isolated thermal anomalies for break-up tectonics (Gac & Geoffroy 2009). Important is in this context also their potential link to large-scale tectonic processes related to supercontinental fragmentation.

3 METHODS

3.1 Code description

The numerical experiments presented here were conducted with a 2-D version of the thermomechanical viscous-plastic code I3ELVIS (Gerya & Yuen 2007; Gerya 2010) that solves Stokes flow and heat conservation equations using finite-differences combined with a marker-in-cell technique. In this numerical scheme, physical properties are transported by Lagrangian markers that move according to the velocity field interpolated from the fixed fully staggered Eulerian grid.

The Stokes flow approximation is given by conservation of momentum:

$$\nabla \cdot \eta \nabla v = \nabla P - \rho g, \tag{1}$$

and conservation of mass which is ensured by the incompressible continuity equation:

$$\nabla \cdot v = 0, \tag{2}$$

where η is the material viscosity, v is the velocity field, P is the pressure, ρ is the density and g is the gravity acceleration (9.8 m $\times$ s^{-2}).

The mechanical equations are coupled to the heat conservation equation that takes the following form:

$$\rho c_p \left(\frac{\partial T}{\partial t}\right) = \nabla \cdot k \nabla T + \rho H_r, \tag{3}$$

where T is the temperature, c_p is the heat capacity, k is the thermal conductivity and H_r is the radiogenic heat production (Table 1).

The code uses non-Newtonian viscoplastic rheologies (Burov 2011) where the viscosity for dislocation creep (η_{creep}) is defined as follow (Karato & Wu 1993; Ranalli 1995; Ershov & Stephenson 2006):

$$\eta_{\text{creep}} = {}^1\!/_2 \left(A_D \exp\left(\frac{E + PV}{RT}\right)\right)^{\frac{1}{n}} \dot{\varepsilon}_{\text{II}}^{\frac{1-n}{n}}, \tag{4}$$

where $\dot{\varepsilon}_{\text{II}} = \sqrt{1/2 \dot{\varepsilon}_{ij} \dot{\varepsilon}_{ij}}$ is the second invariant of the strain rate tensor and A_D, E, V, n and R are the pre-exponential constant, the activation energy, the activation volume, the stress exponent, and the gas constant (8.314 J $\times$ K^{-1} $\times$ mol^{-1}), respectively (see also Table 1). Different ductile flow law mechanisms such as diffusion (Karato 1986), grain boundary sliding (Précigout *et al.* 2007) and Peierls (Karato 2008) creep are neglected.

In order to combine the ductile rheology with a brittle rheology, the Mohr–Coulomb yield criterion (Ranalli 1995) is implemented

Table 1. Rheological and thermal parameters.

		Rheological parameters									Thermal parameters		
		Ductile				C [MPa]		Brittle $\sin(\varphi)$		ε			
Material	Flow law	A_D [Pa^n $\times$ s]	E [kJ $\times$ mol^{-1}]	V [J $\times$ MPa^{-1} $\times$ mol^{-1}]	n	C_0	C_1	b_0	b_1	ε_0	ε_1	k [W $\times$ m^{-1} $\times$ K^{-1}]	H_r [μW $\times$ m^{-3}]
Upper crust	Wet quartzite	1.97×10^{17}	154	0	2.3	10	3	0.6	0.3	0.0	0.25	$0.64 + \frac{807}{T+77}$	2.00
Lower Crust Felsic	Wet quartzite	1.97×10^{17}	154	0	2.3	10	3	0.6	0.3	0.0	0.25	$0.64 + \frac{807}{T+77}$	1.00
Mafic	Plagioclase (An75)	4.80×10^{22}	238	0	3.2	10	3	0.6	0.3	0.0	0.25	$1.18 + \frac{474}{T+77}$	0.25
Lithospheric/ sublithospheric mantle	Dry olivine	3.98×10^{16}	532	1.6	3.5	10	3	0.6	0.3	0.0	0.25	$0.73 + \frac{1293}{T+77}$	0.022
Mantle plume	Wet olivine	5.01×10^{20}	470	1.6	4.0	3	3	0.1	0.0	0.0	0.25	$0.73 + \frac{1293}{T+77}$	0.024

Mantle density and heat capacity are computed as function of pressure and temperature using the Perple_X algorithm (Connolly 2005) with the thermodynamic database taken from Holland & Powell (1998, revised 2002) and the LOSIMAG composition by Hart & Zindler (1986). For the crustal rocks, heat capacity c_p = 1000 J $\times$ kg^{-1}K^{-1}, whereas density is calculated from Boussinesq approximation: $\rho = \rho_0 [1 - \alpha(T - T_0)][1 + \beta(P - P_0)]$, where $\alpha = 3 \times 10^{-5}$ K^{-1} is thermal expansion coefficient, $\beta = 1 \times 10^{-5}$ MPa^{-1} is adiabatic compressibility, and ρ_0 is reference density (at P_0 = 0.1 MPa and T_0 = 298 K) which is taken as 2700 and 3000 kg $\times$ m^{-3} for upper and lower crust, respectively. Basaltic oceanic crust is modelled with the same material properties as mafic lower continental crust.

by limiting creep viscosity (η_{creep}) as follows:

$$\eta_{creep} \leq \frac{\sigma_{yield}}{2\dot{\varepsilon}_{II}}, \quad (5)$$

with the plastic strength (σ_{yield}) determined as:

$$\sigma_{yield} = C + P\sin(\varphi), \quad (6)$$

where C and φ are the residual rock strength and the internal frictional angle that decrease with increasing values of total strain due to linear strain softening (Huismans & Beaumont 2002; Brune & Autin 2013):

$$C = C_0 + (C_1 - C_0)\frac{\varepsilon - \varepsilon_0}{\varepsilon_1 - \varepsilon_0}, \quad (7)$$

$$\in(\varphi) = b_0 + (b_1 - b_0)\frac{\varepsilon - \varepsilon_0}{\varepsilon_1 - \varepsilon_0}, \quad (8)$$

where ε is the second invariant of strain and C_0, C_1, b_0, b_1, ε_0 and ε_1 are softening parameters (maximal and minimal cohesion, sines of frictional angle and strains, respectively) provided in Table 1.

Partial melting is introduced using the most common parametrization (Katz *et al.* 2003; Gerya 2013a) applied for dry peridotite at mantle conditions. Thermomechanical effects of magmatic weakening due to upward migration of extracted melts (Ueda *et al.* 2008; Gerya & Meilick 2011; Gerya *et al.* 2015; Bahadori & Holt 2019) are neglected.

For a detailed description of the code we refer to Gerya & Yuen (2007) and Gerya (2010).

3.2 Model design

The model setup encompasses an area of 1500 km in length and 400 km in depth. The regular rectangular grid contains 430 × 115 nodes, resulting in a spatial resolution of ~3.5 km in each direction.

This study incorporates two groups of kinematic boundary conditions: (1) a tectonically neutral regime with free slip commonly adopted for all border elements and (2) a regime of tectonic extension when a constant, time-independent extensional tectonic forcing is applied along the entire length of the vertical sides of the model domain with a half-rate (V_{ext}) varying from 2 mm × yr^{-1} to 10 mm × yr^{-1}. In the latter group of experiments, compensating vertical velocities are introduced along the upper and lower model boundaries in order to ensure mass conservation within the model box.

In all simulations, the uppermost part of the model consists of a 30-km-thick layer of low-viscosity (10^{18} Pa × s) and low-density (1.0 kg × m^{-3}) 'sticky air' (Fig. 2) allowing to approximate the upper surface of the crust as a free surface (Duretz *et al.* 2011; Crameri *et al.* 2012).

The internal model structure corresponds to a laterally homogenous crust and mantle lithosphere overlying the sublithospheric (asthenospheric) mantle. We test four types of lithosphere: three continental of different thermotectonic ages ('Cratonic', 'Variscan' and 'Mesozoic') and one oceanic (~40 Myr old). For this purpose, we vary the thickness and composition of the crustal layers, and the depth of the lithosphere–asthenosphere boundary (LAB). In the 'continental' experiments, the crustal thickness has a constant value of 36 km (equally divided into upper and lower crust), whereas the LAB depth changes from 250 km ('Cratonic' lithosphere; Fig. 2a) through 150 km ('Variscan' lithosphere; Fig. 2b) to 125 km ('Mesozoic' lithosphere; Fig. 2c). The oceanic lithosphere with an age of ~40 Myr has a thickness of 80 km including 8 km of one-layered crust (Fig. 2d).

Regardless the type and thickness of the overlying lithosphere, the mantle plume is always seeded by a circular-shaped temperature anomaly within the asthenospheric mantle maintaining 10 km distance between the LAB and the uppermost point of this anomaly (Figs 2a–d). Together with the applied velocity of far-field extension (V_{ext}) and lithospheric type, the initial diameter (d_{init}: 80, 100 or 116 km) and initial temperature (T_{init}: 1500, 1600 or 1700 °C) of the mantle plume represent the key variable parameters of our study (see Section 3.3 and Table 2). The range of tested initial temperatures is adopted following previous studies indicating that plume excess temperatures in the upper mantle vary between 200 and 350 °C (e.g. Schilling 1991; White & McKenzie 1995; Thompson & Gibson 2000; Herzberg & Gazel 2009). Note that modelled mantle plumes are assumed to be purely thermal, that is without compositional buoyancy component commonly attributed to so-called 'thermal–chemical' plumes (e.g. Dobretsov *et al.* 2008; Sobolev *et al.* 2011; Baes *et al.* 2016).

We use a felsic composition described by a wet quartzite rheology for the upper crust in all 'continental' models (Figs 2a–c) and for the lower crust of 'Variscan' and 'Mesozoic' lithospheres (Figs 2b and c). In contrast, a mafic composition and rheology (plagioclase flow law) is adopted for the lower crust of the 'Cratonic' lithosphere (Fig. 2a). The basaltic crust of the oceanic lithosphere (Fig. 2d) is assumed to have the same properties as mafic lower continental crust. Both lithospheric and sublithospheric mantle are approximated by an ultra-mafic composition with the rheology of dry olivine, whereas the mantle plume is supposed to be slightly 'moist' with a wet olivine rheology (Table 1).

The initial temperature distribution within the continental lithosphere is approximated by a nonlinear steady-state geotherm defined by temperatures of 0 and 1300 °C at the top of the upper crust (depth of 0 km) and the bottom of the lithosphere (depth of 125, 150 or 250 km depending on the type of lithosphere—see above) while taking into account heat production in the upper and lower crust and lithospheric mantle (Table 1; Figs 2a–c). For the oceanic lithosphere, the initial temperatures are computed using a semi-infinite half-space cooling model (Turcotte & Schubert 2002) for the adopted age of ~40 Myr (Fig. 2d). In all experiments, the sublithosphere geotherm is defined by an adiabatic thermal gradient of 0.3 °C km^{-1} (Sleep 2003). As thermal boundary conditions, we apply a constant temperature at the upper surface of the model domain, a constant conductive heat flux at the model bottom, and thermally insulating (zero conductive heat flux) vertical sides.

3.3 Modelling procedure

In total, we performed numerical calculations for a set of 42 models by varying four controlling parameters (Table 2): (1) initial temperature (T_{init}) and (2) diameter (d_{init}) of the mantle plume; (3) type of lithosphere and (4) half-rate of applied tectonic extension (V_{ext}).

The first group of the experiments (models **1–18**) is characterized by a tectonically neutral regime (V_{ext}: 0 mm × yr^{-1}; see Section 4.1). Here we start with a series of models where the mantle plume of different initial temperatures (T_{init}: 1500, 1600 or 1700 °C) and sizes (d_{init}: 80, 100 or 116 km) is seeded below 'Variscan' continental lithosphere (models **1–9**; Section 4.1.1). Subsequently, we test various types of overlying lithosphere (models **10–18**; Section 4.1.2)—'Cratonic' (models **10–12**), 'Mesozoic' (models **13–15**) and oceanic (models **16–18**)—with the plume of different temperatures (T_{init}: 1500, 1600 or 1700 °C) but of constant diameter (d_{init}: 100 km). For the tectonically neutral thermomechanical simulations, we have

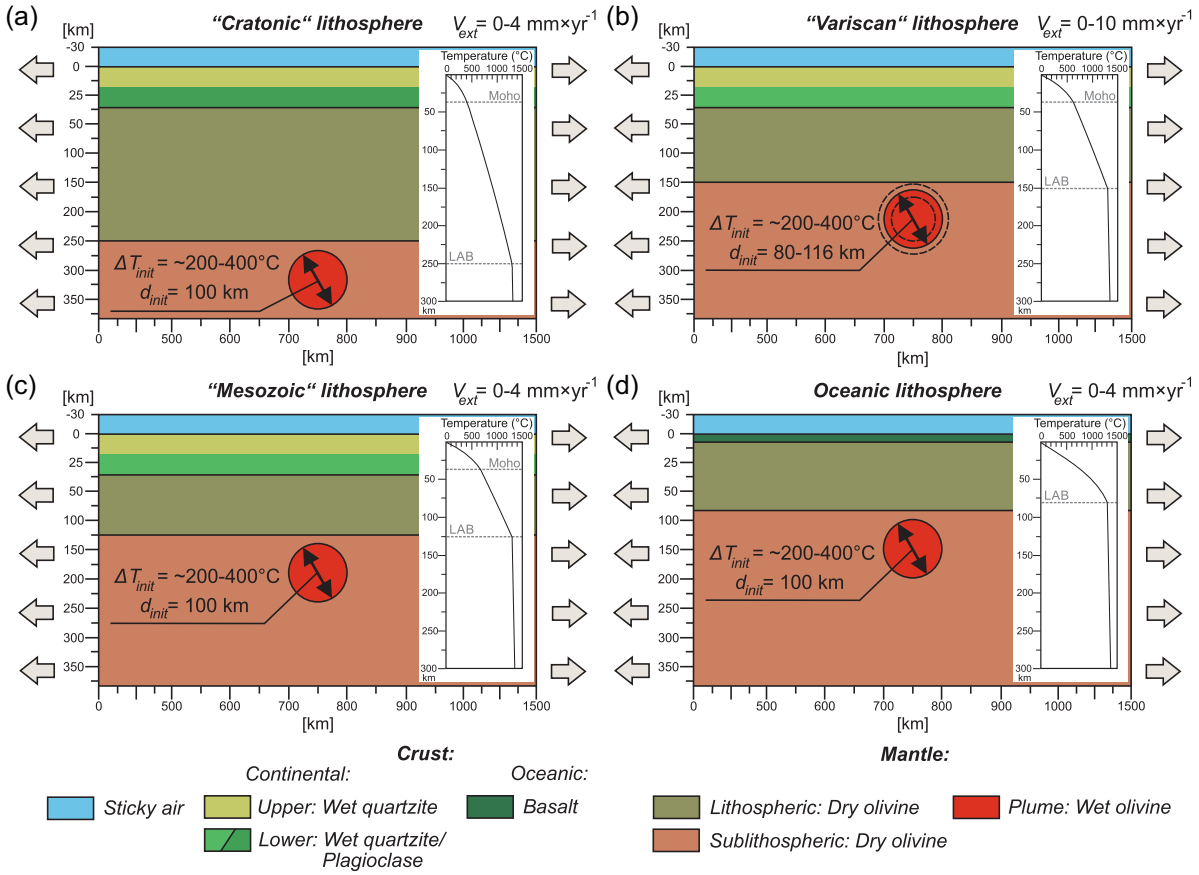

Figure 2. Design of 2-D model setup for four tested types of lithosphere: (a–c) Continental lithosphere: (a) 'Cratonic', (b) 'Variscan', (c) 'Mesozoic' and (d) oceanic lithosphere (~40 Ma old). Insets show the initial temperature distributions. A circular-shaped mantle plume anomaly is seeded just below the bottom of the lithosphere. Lateral velocities (V_{ext}) are applied at vertical sides of the model.

additionally performed their thermal model analogues that exclude a kinematic component aiming to determine the purely thermal effect of the seeded anomaly. The time span of all models with a tectonically neutral regime is 300 Myr.

In the second group of models (models **19–42**), we study the impact of external tectonic extension (V_{ext}: 2–10 mm × yr^{-1}; see Section 4.2). Similarly to tectonically neutral models, we first investigate the case of 'Variscan' lithosphere (models **19–33**; Section 4.2.1) which is subjected to far-field extension with a broad range of applied half-rates (V_{ext}: 2, 3, 4, 5 or 10 mm × yr^{-1}) also in combination with various plume temperatures (T_{init}: 1500, 1600 or 1700 °C). Finally, we explore (see Section 4.2.2) other lithospheric types—'Cratonic' (models **34–36**), 'Mesozoic' (models **37–39**) and oceanic (models **40–42**)—in the context of relatively slow extension (V_{ext}: 2, 3 or 4 mm × yr^{-1}) and a non-changing initial temperature of the plume (T_{init}: 1600 °C). Simulations of the second group models have been terminated when lithospheric break-up was reached.

4 RESULTS

4.1 Tectonically neutral regime (Models 1–18)

*4.1.1 Effect of initial plume temperature and diameter (models **1–9**)*

As mentioned above, we start our modelling with a series of experiments aimed to explore the variations in initial temperature (T_{init}) and size (d_{init}) of the circular thermal anomaly (mantle plume) seeded underneath unstressed (V_{ext}: 0 mm × yr^{-1}) 'Variscan' continental lithosphere.

In the first three experiments (models **1–3**), the mantle plume anomaly has the same initial diameter (d_{init}: 100 km) whereas its initial temperature (T_{init}) varies from 1500 °C (model **1**: 'cold' plume) through 1600 °C (model **2**: 'warm' plume) to 1700 °C (model **3**: 'hot' plume), that corresponds to maximum temperature contrasts with surrounding sublithospheric mantle (ΔT_{init}) of ~200, ~300 and ~400 °C, respectively.

In the case of an intermediate plume temperature (model **2**; T_{init}: 1600 °C), vertical and horizontal movement of the plume body results in the configuration dubbed an 'inverted pear' (Figs 3a and 4b1). Limited buoyancy contrasts in the experiment with the lowest plume temperature (model **1**; T_{init}: 1500 °C) prohibit almost any motion in the compositional field making indistinguishable the modifications in the circular shape of the original mantle plume which keeps its initial configuration throughout the entire modelling time interval (Figs 4a1 and A1a). The plume material of the hottest thermal anomaly (model **3**; T_{init}: 1700 °C) first flows upwards and then spreads laterally below the LAB (Figs 4c1 and A2a). As a result, the plume body changes its shape from an original circular (Fig. 2b) into a heart-like configuration (Fig. A2a; time slice of 15 Myr). Subsequently, the latter evolves into a quasi-elliptical form with an aspect ratio of vertical height (d_{ver}) to horizontal length (d_{hor}) of ~1:2 (Figs 4c1 and A2a; time slices of ≥60 Myr). Note that in both models **2** and **3**, the final figure of the plume is established at

Table 2. Controlling parameters of the numerical experiments.

№	Controlling parameters: Plume properties: Temperature, T_{init} [°C]	Plume properties: Diameter, d_{init} [km]	Type of lithosphere	Extension half-rate, V_{ext} [mm × yr^{-1}]	Figure	Section
1	1500	100	'Variscan'	0	A1, 4, 5, A3, 9, 11, 12, A10	4.1.1
2	1600	100	'Variscan'	0	3, 4, 5, 6, 9, 10, 11, 12, A11	
3	1700	100	'Variscan'	0	A2, 4, 5, A4, 9, 11, 12, A12	
4	1500	80	'Variscan'	0	A3, 9	
5	1600	80	'Variscan'	0	6, 9	
6	1700	80	'Variscan'	0	A4, 9	
7	1500	116	'Variscan'	0	A3, 9	
8	1600	116	'Variscan'	0	6, 9	
9	1700	116	'Variscan'	0	A4, 7, 8, 9	
10	1500	100	'Cratonic'	0	A5, 11, 12	4.1.2
11	1600	100	'Cratonic'	0	A5, 10, 11, 12	
12	1700	100	'Cratonic'	0	A5, 11, 12	
13	1500	100	'Mesozoic'	0	A6, 11, 12	
14	1600	100	'Mesozoic'	0	A6, 10, 11, 12	
15	1700	100	'Mesozoic'	0	A6, 11, 12	
16	1500	100	oceanic	0	A7, 11, 12	
17	1600	100	oceanic	0	A7, 10, 11, 12	
18	1700	100	oceanic	0	A7, 11, 12	
19	1500	100	'Variscan'	2	A8, A10, 14	4.2.1
20	1600	100	'Variscan'	2	13, A11, 14, 15, 16	
21	1700	100	'Variscan'	2	A9, A12, 14	
22	1500	100	'Variscan'	3	A10, 14	
23	1600	100	'Variscan'	3	A11, 14, 16	
24	1700	100	'Variscan'	3	A12, 14	
25	1500	100	'Variscan'	4	14	
26	1600	100	'Variscan'	4	14, 16	
27	1700	100	'Variscan'	4	14	
28	1500	100	'Variscan'	5	14	
29	1600	100	'Variscan'	5	14, 16	
30	1700	100	'Variscan'	5	14	
31	1500	100	'Variscan'	10	14	
32	1600	100	'Variscan'	10	14, 16	
33	1700	100	'Variscan'	10	14	
34	1600	100	'Cratonic'	2	15, 16	4.2.2
35	1600	100	'Cratonic'	3	16	
36	1600	100	'Cratonic'	4	16	
37	1600	100	'Mesozoic'	2	15, 16	
38	1600	100	'Mesozoic'	3	16	
39	1600	100	'Mesozoic'	4	16	
40	1600	100	oceanic	2	15, 16	
41	1600	100	oceanic	3	16	
42	1600	100	oceanic	4	16	

Note: The depths of Moho and LAB for different types of lithosphere: 'Cratonic' (Moho: 36 km, LAB: 250 km); 'Variscan' (Moho: 36 km, LAB: 150 km); 'Mesozoic' (Moho: 36 km, LAB: 125 km); oceanic (Moho: 8 km, LAB: 80 km). See Section 3 for more detail.

~50–60 Myr after model onset without subsequent changes (Figs 3a and A2a).

The presence of the thermal anomaly seeded just below the lithospheric bottom leads to upward deflection of the 1300 °C isotherm by several tens of km (e.g. model **2**; Fig. 3b) This deflection not only remains discernible over the whole time span of all models (including the experiment with the 'cold' mantle plume—see model **1** in Figs 4a2 and A1b) but also appears to be more pronounced (in terms of both width and amplitude; Figs 4c2 and A2b) when the plume is 'hot' (model **3**; T_{init}: 1700 °C). In the latter case a stronger thermal impact is accompanied by a mechanical component of the vertical uplift combined with horizontal propagation of the plume material underneath the lithosphere (Figs 4c1 and A2a).

However, regardless the adopted initial temperature T_{init} the mantle plumes themselves become almost invisible in the temperature fields (T) after several tens to 100 Myr (see Figs 3b, A1b and A2b). In order to illustrate in more detail the evolution of explored plume-related thermal anomalies, we compute the temperature contrast (ΔT) defined as the difference between the current temperature in the corresponding grid node and the temperature from the near-edge column taken at the same vertical level. Distributions of the temperature contrast (ΔT) are calculated for each time step (see Figs 3c and 4, lower row; Figs A1c and A2c) allowing to explore the evolution of plume-induced thermal disturbances in space and time with the following parameters (Fig. 5):

1) Maximum temperature contrast detected over the entire modelling area at the current time step (ΔT_{max});

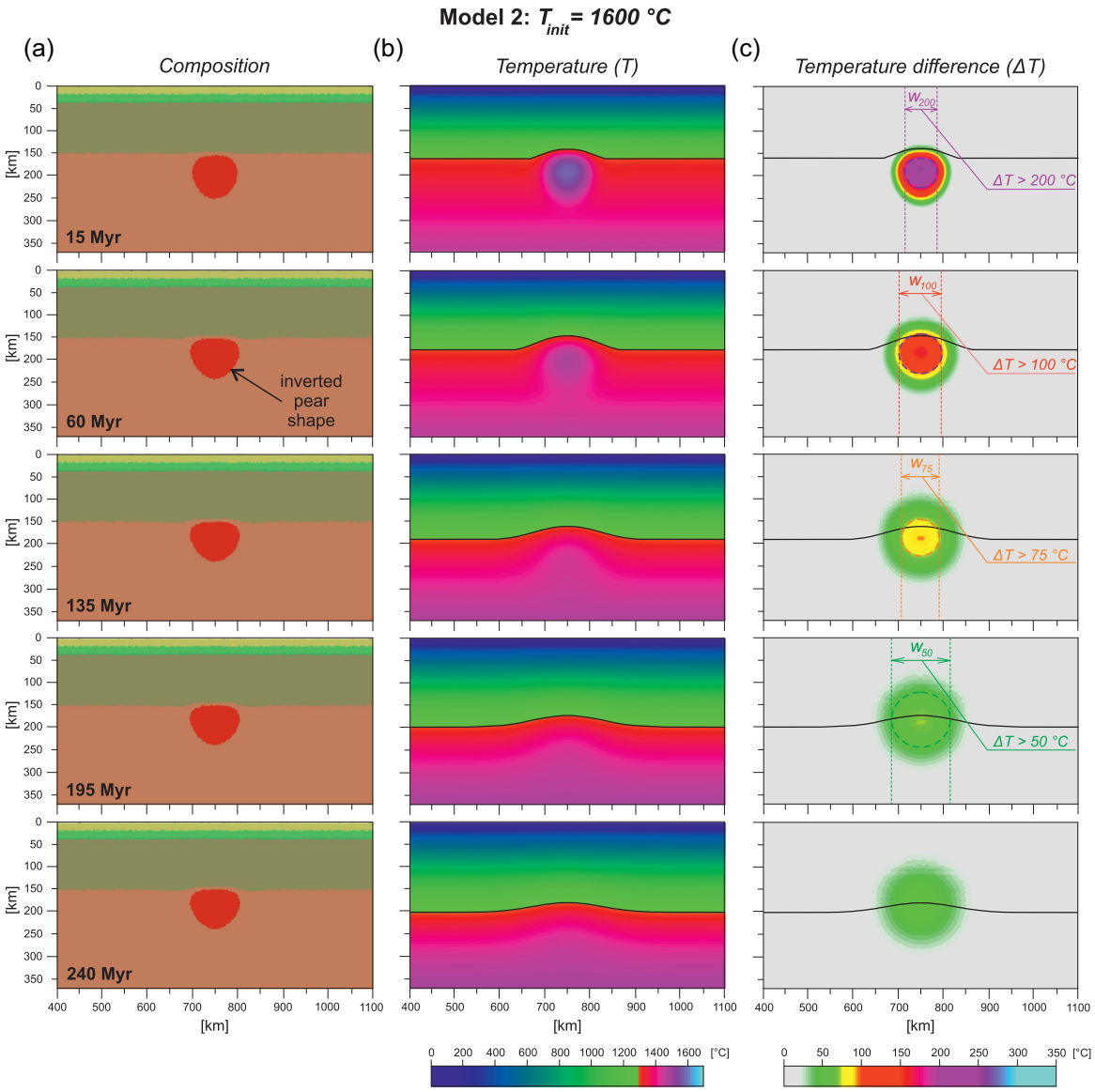

Figure 3. Temporal evolution of model **2** (T_{init}: 1600 °C; d_{init}: 100 km; type of lithosphere: 'Variscan'; V_{ext}: 0 mm × yr^{-1}): (a) material phase field. Since 60 Myr the plume has an inverted pear (or a light bulb) shape; (b) distribution of the temperatures (T) and (c) temperature contrasts (ΔT). The areas A_x and corresponding w_x are shown in the panel 'c' for the following ΔT thresholds: $x = 200$, 100, 75 and 50 °C.

2) Maximum horizontal extent or width (w_x) of the area (A_x) characterized by a temperature contrast (ΔT) higher than a predefined threshold value (x). We present here w_x estimated for A_x corresponding to $x = 300$, 200, 100, 75 and 50 °C (i.e. w_{300}, w_{200}, w_{100}, w_{75} and w_{50}, respectively). Examples of areas A_x defined for various x as well as corresponding w_x are illustrated in Fig. 3c;

3) Temperature contrast integral (ΔT_x^{int}) taken over the area A_x (see above) as follow: $\Delta T_x^{int} = \iint_{A_x} \Delta T dA_x$. Similar to w_x, we estimate five values of ΔT_x^{int}: ΔT_{300}^{int}, ΔT_{200}^{int}, ΔT_{100}^{int}, ΔT_{75}^{int} and ΔT_{50}^{int}.

As mentioned above, the initial maximum temperature contrast (ΔT_{max} at 0 Myr or ΔT_{init}) varies from of ~200 to ~400 °C depending on the initial plume temperature (T_{init}). In all experiments, ΔT_{max} decreases quickly during the first ~50–100 Myr after that cooling slows down (Fig. 5, upper row). Although all curves of ΔT_{max} look at first sight similar, the time points when they descent below the reference temperature values (e.g. 200, 100 or 75 °C) appear to vary over a wide range from one experiment to another. In particular, the difference in the timing of cooling below 100 °C between 'cold' plume model **1** (T_{init}: 1500 °C) and 'hot' plume model **3** (T_{init}: 1700 °C) is exceeding 100 Myr.

The temporal evolution of w_{100} (horizontal width of the plume segment where ΔT_{max} remains higher than 100 °C) also significantly differs within these models (Fig. 5, middle row). The 'cold' model **1** shows a quick decrease of w_{100} in a quasi-parabolic manner from initial 100 km (at 0 Myr) to 0 km at ~55 Myr. On the contrary, w_{100} of the 'warm' experiment (model **2**) remains close to the original value of 100 km over the first ~60 Myr before its parabolic drop to zero during the following ~65 Myr. As mentioned above, the 'hot' plume anomaly (model **3**; T_{init}: 1700 °C) flattens below the LAB thus subjecting the originally circular plume to significant horizontal stretching (Fig. 4c1). As a result, at the early stage of evolution w_{100} becomes wider than its initial value of 100 km reaching ~150 km at ~20–60 Myr whereas its subsequent quasi-parabolic descent lasts

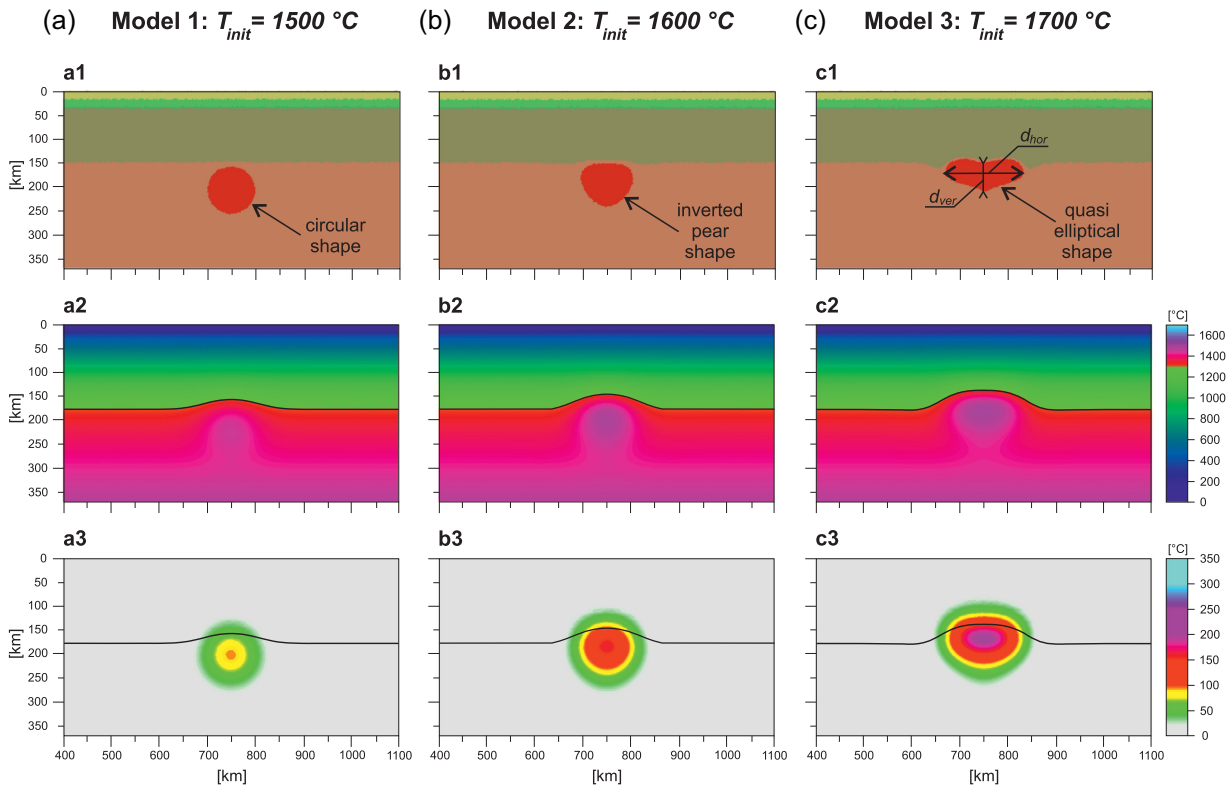

Figure 4. (a) Model **1** (T_{init}: 1500 °C; *); (b) model **2** (T_{init}: 1600 °C; *) and (c) model **3** (T_{init}: 1700 °C; *) represented by (1) material phase field (upper row); (2) distribution of the temperatures (T; middle row); (3) temperature contrasts (ΔT; lower row) at the time slice of 60 Myr. *Other experimental parameters: d_{init}: 100 km; type of lithosphere: 'Variscan'; V_{ext}: 0 mm × yr^{-1}.

more than a hundred Myr (~130 Myr, i.e. >2 time longer than in models **1** and **2**) ending at ~190 Myr.

Given that a temperature contrast of 100 °C is close to the minimum ΔT value detectable by seismic tomography imaging (e.g. Cammarano *et al.* 2003), we exploit w_{100} to identify quantitatively the moment in time when the plume evolution enters into the terminal phase. For this purpose, we introduce a new parameter $t(w_{100}^{50})$ which refers to the time point when w_{100} subsides below 50 km (i.e. half of original w_{100}; Fig. 5b2), thus approaching the resolution limit of modern seismic tomography (e.g. Rickers *et al.* 2013; Plomerová *et al.* 2016). While $t(w_{100}^{50})$ characterizes a 'decay time' of the thermal anomaly, a plume 'lifespan' corresponds to the time period between model onset (0 Myr) and $t(w_{100}^{50})$. Despite the extremely small size (d_{init}: 100 km) of the 'baby' plumes explored here, their lifespan appears to cover long time intervals varying from ~40 Myr (model **1**; T_{init}: 1500 °C) through ~110 Myr (model **2**; T_{init}: 1600 °C) to ~170 Myr (model **3**; T_{init}: 1700 °C).

Graphs of integrated temperature contrasts (ΔT_x^{int}) for the models **1–3** are summarized in the lower row of Fig. 5. The quasi-parabolic reduction of each ΔT_x^{int} during the first ~20–30 Myr is faster than their subsequent quasi-linear decrease. Expectedly, the steepness of both non-linear and linear trends of ΔT_x^{int} evolution is mainly controlled by the ΔT threshold limit (i.e. x) which defines integrating area A_x for each ΔT_x^{int} (see above): higher x values result in a steeper decrease of ΔT_x^{int}. On the contrary, the initial value of ΔT_x^{int} (i.e. ΔT_x^{int} at 0 Myr) is independent from x because an original A_x coincides with the circular area of the imposed thermal anomaly for all tested ΔT threshold limits (i.e. x) that are lower than ΔT_{init} (i.e. ΔT_{max} at 0 Myr). Thus, the initial ΔT_x^{int} in the model **1** (T_{init}: 1500 °C) is ~1.2 × 10^{12} °C × m^2 for all $x \leq 100$ °C (see grey star in Fig. 5a3). This initial ΔT_x^{int} corresponds to an integrated value of plume buoyancy of ~1.2 × 10^{11} kg × m^{-1}. In the models **2** (T_{init}: 1600 °C) and **3** (T_{init}: 1700 °C), ΔT_x^{int} for x = 100 °C (i.e. ΔT_{100}^{int}) decreases to the same value (~1.2 × 10^{12} °C × m^2) at ~35 and ~95 Myr, respectively (see grey stars in Figs 5b3 and c3). Note also that the values of w_{100} corresponding to these time points (~35 and ~95 Myr) in these experiments (models **2** and **3**) are close to or even slightly exceed the initial d_{init} of 100 km. Therefore, it appears that the evolution of 'warm' (model **2**; T_{init}: 1600 °C) and 'hot' (model **3**; T_{init}: 1700 °C) mantle plumes is characterized by time intervals of tens to 100 Myr when the sum temperature excess concentrated within the area of a seismically detectable thermal anomaly (ΔT >100 °C; $w_{100} \geq$100 km) remains higher or roughly equal to the original (i.e. at 0 Myr) temperature contrast integrated over the surface of a 'cold' mantle plume (model **1**; T_{init}: 1500 °C).

In order to investigate the role of initial plume size we performed the models with different d_{init}: 80 km (models **4–6**) and 116 km (models **7–9**). The values of 80 and 116 km are chosen to ensure that variations in the initial plume area are by a factor of ~2 between the smallest and largest end-members: given that $A = \frac{\pi d^2}{4}$, $A(T_{\text{init}} = 116 \text{ km}) \approx 2 \times A(T_{\text{init}} = 80 \text{ km})$ because $116^2 \approx 2 \times 80^2$.

For intermediate temperature (T_{init}: 1600 °C), variations in the initial diameter (d_{init}: 80, 100 or 116 km) of the plume anomaly appear to have a similar effect to that of initial temperature changes (T_{init}: 1500, 1600 or 1700 °C) in the 'standard' diameter (d_{init}: 100 km) models (compare Figs 5 and 6). A plume with a reduced initial diameter (d_{init}: 80 km) starts to decay ~55 Myr earlier (at ~55 Myr) than in the standard (d_{init}: 100 km) case (~110 Myr)—see decay time $t(w_{100}^{50})$ indicated in Figs 6a2 and b2, respectively. On the contrary, an increased diameter (d_{init}: 116 km) extends the

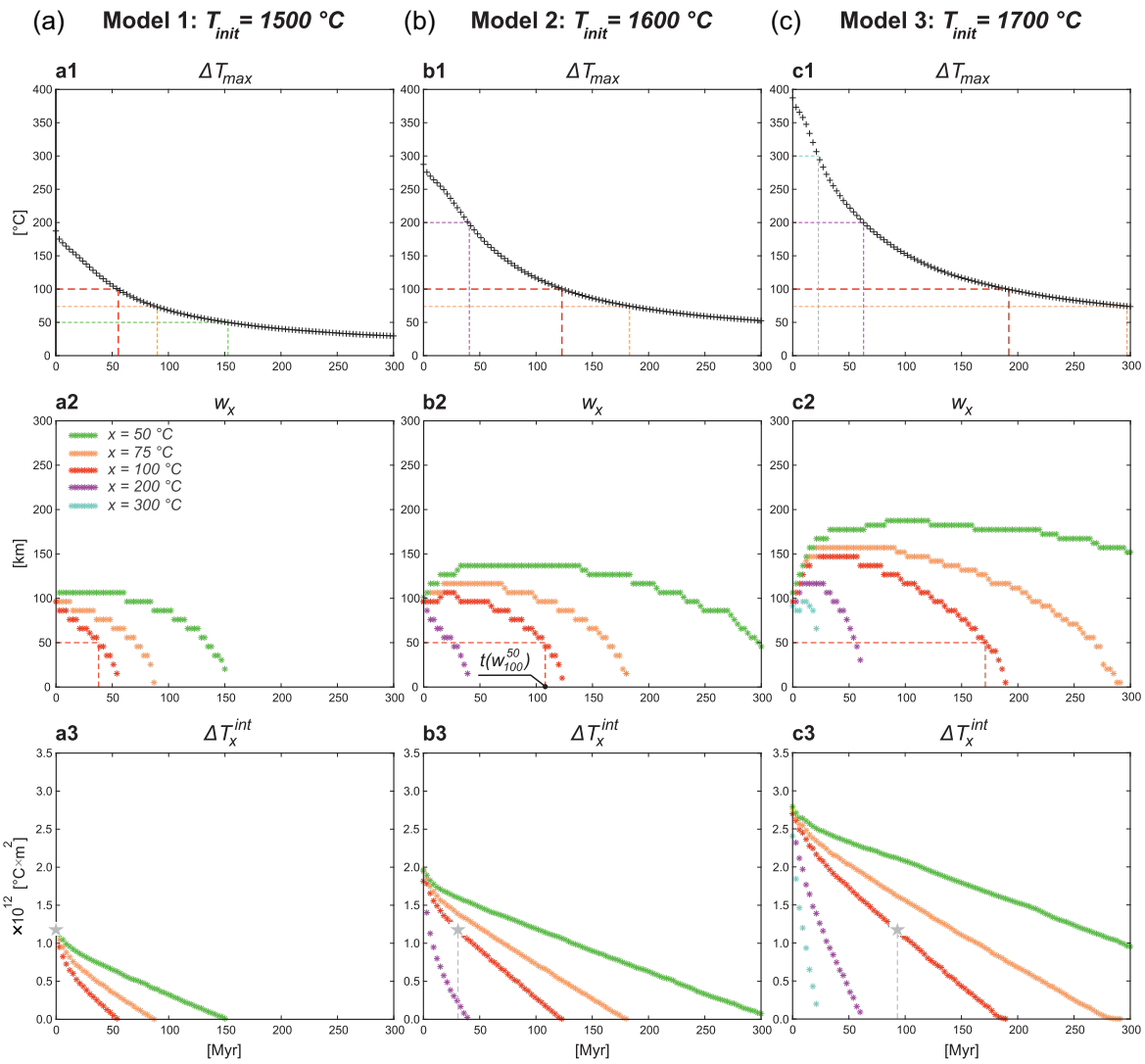

Figure 5. Temporal evolution of (a) model **1** (T_{init}: 1500 °C; *); (b) model **2** (T_{init}: 1600 °C; *) and (c) model **3** (T_{init}: 1700 °C; *) represented by the following parameters derived from the distributions of temperature contrasts (ΔT): (1) maximum temperature contrast ($\Delta T_{\max}$; upper row); (2) maximum horizontal width of the area A_x (w_x; middle row) and (3) temperature contrast integrated over the area A_x (ΔT_x^{int}; lower row). A_x is the area where ΔT is higher than a threshold limit x. The values of x vary from 300 to 50 °C. Grey stars mark the value of ΔT_{100}^{int} corresponding to the initial value of ΔT_x^{int} in the model **1** (~1.2 × 10^{12} °C × m^2). *Other experimental parameters: d_{init}: 100 km; type of lithosphere: 'Variscan'; V_{ext}: 0 mm × yr^{-1}.

lifespan of the plume by ~50 Myr up to ~160 Myr (Fig. 6c2). Note, however, that the total range of $t(w_{100}^{50})$ resulting from temperature variations (T_{init}: 1500, 1600 or 1700 °C) for a standard diameter (d_{init}: 100 km) is wider than that caused by diameter changes for intermediate temperature (T_{init}: 1600 °C): ~130 (~170–40) Myr and ~105 (~160–55) Myr, respectively.

The minimum plume lifespan ($t(w_{100}^{50})$ of ~20 Myr) is detected in the model **4** with the minimum initial temperature (T_{init}: 1500 °C) and diameter (d_{init}: 80 km) whereas the maximum plume size (d_{init}: 116 km) combined in the model **9** with the hottest temperature (T_{init}: 1700 °C) leads to >10 times longer ($t(w_{100}^{50})$ of ~245 Myr) life expectancy (see Figs A3 and A4, respectively).

The end-member model **9** (T_{init}: 1700 °C; d_{init}: 116 km) is characterized by the most pronounced 'mechanical' component expressed in vertical and horizontal movements of the plume material leading to significant changes in the configuration of an initially circular plume body (see also model **3** in Fig. 4c1). Fig. 7 illustrates the differences in the evolution of temperature (T) and temperature contrast (ΔT) fields for the thermomechanical model **9** (Fig. 7a) and its purely thermal analogue (Fig. 7b). While the plume anomaly of the thermal model remains symmetrical in both directions, in the thermomechanical case it takes the shape of an ellipse stretched horizontally. As a result, the plume-related upward deflection of the LAB (corresponding to uplift of the 1300 °C isotherm) becomes significantly wider in the thermomechanical model during the first tens to 100 Myr while this difference in 'thermomechanical' and 'thermal' LAB configurations recedes over the final stage (>200 Myr) of system evolution (compare Figs 7a and b).

During the first ~100–150 Myr the immovable circular plume of the thermal model cools slower than its thermomechanical counterpart: the maximum temperature contrast (ΔT_{max}) descends below 300 and 200 °C at ~45 and ~95 Myr only (Fig. 8b1), that is ~25–30 Myr later than in the thermomechanical experiment (Fig. 8a1). At the same time, lateral displacements allowed in the thermomechanical model favour a rapid increase in all examined w_x from

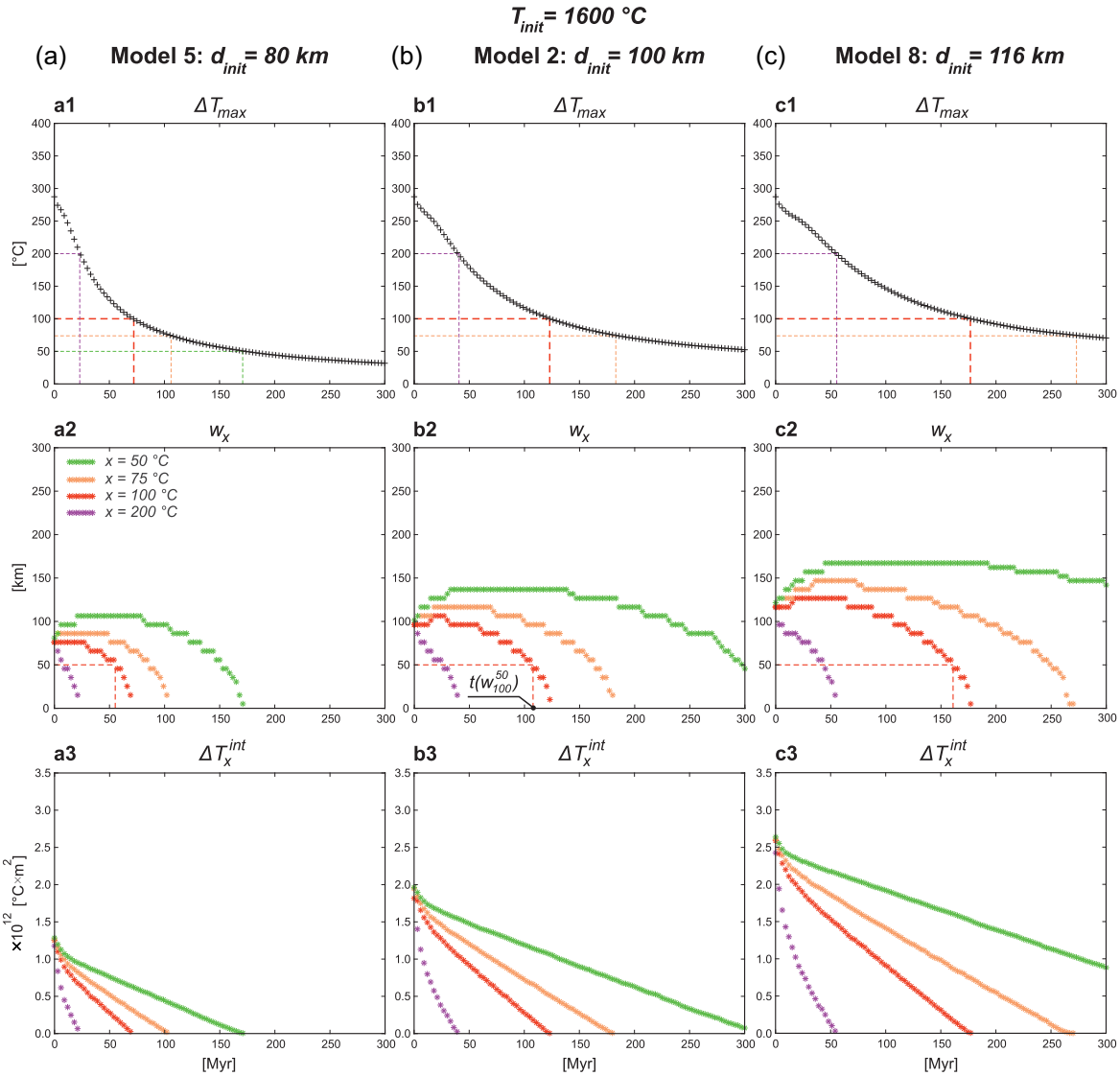

Figure 6. Temporal evolution of the experiments characterized by T_{init} of 1600 °C and different d_{init}: (a) model **5** (d_{init}: 80 km; *); (b) model **2** (d_{init}: 100 km; *); and (c) model **8** (d_{init}: 116 km; *) represented by parameters derived from ΔT. Figure conventions as in Fig. 5. *Other experimental parameters: type of lithosphere: 'Variscan'; V_{ext}: 0 mm × yr^{-1}.

w_{300} to w_{50} during the first 15–30 Myr (Fig. 8a2). This is in striking contrast to the thermal model where w_{300} and w_{200} start to decrease immediately after model onset while growth in w_{100}, w_{75} and w_{50} is of more moderate magnitudes (Fig. 8b2). In particular, w_{100} of the thermomechanical model reaches the maximum value of ~200 km (at ~25–65 Myr) whereas its thermal counterpart hardly exceeds ~130 km. Moreover, the value of 'thermomechanical' w_{100} remains higher than that of the 'thermal' one over the entire time interval when ΔT_{max} exceeds 100 °C (~255 Myr in the thermomechanical case; Fig. 8a1). Therefore, the plume lifespan (defined as $t(w_{100}^{50})$) is paradoxically shorter (~235 Myr) in the thermal version of model **9** (Fig. 8b2) than in its thermomechanical analogue (~245 Myr; Fig. 8a2) which, at first sight, seems to be faster-cooled (compare Figs 8a1 and b1). Note also that in both thermomechanical and thermal versions of the model **9** the value of ΔT_{100}^{int} becomes lower than ~1.2 × 10^{12} °C × m^2 (initial ΔT_x^{int} in the model **1**; Fig. 5a3) after 150 Myr only (see grey stars in Figs 8a3 and b3).

In general, models **1–9** show that plume life expectancy (or lifespan)—time period $t(w_{100}^{50})$ when the thermal anomaly is seismically detectable ($\Delta T > 100$ °C; $w_{100} \geq 50$ km)—is mainly controlled by initial temperature contrasts (initial ΔT_x^{int}) integrated over the surface of the imposed thermal anomaly (Fig. 9). In most cases, values of $t(w_{100}^{50})$ in the thermomechanical model and its purely thermal analogues coincide: only two experiments with a plume of large size (d_{init}: 116 km) and intermediate (T_{init}: 1600 °C) to hot (T_{init}: 1700 °C) temperatures (models **8–9**) demonstrate a ~10 Myr delay of the decay time in the thermomechanical model version (see red stars in Fig. 9). A detailed explanation of this phenomenon is given above based on an examination of the end-member case of the model **9** (see also Figs 7 and 8). Interestingly, $t(w_{100}^{50})$ defined in thermal models can be approximated by linear functions of initial ΔT_x^{int} for each d_{init} (see blue, green, and red lines in Fig. 9 corresponding to d_{init} of 80, 100 and 116 km, respectively). The vertical shifts by ~10 Myr between neighboring lines indicate that for the same amount of integrated temperature excess plume bodies

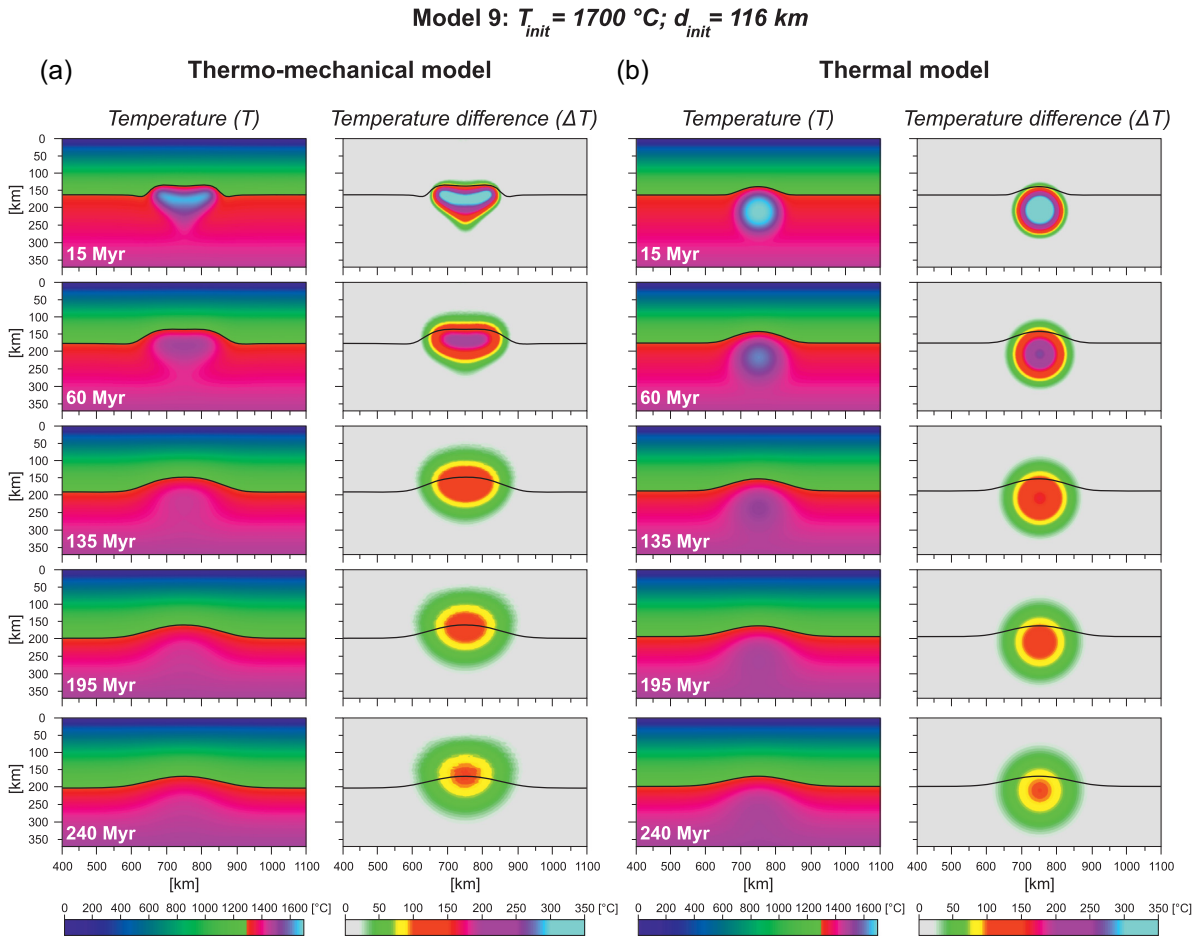

Figure 7. Temporal evolution of model **9** (T_{init}: 1700 °C; d_{init}: 116 km; type of lithosphere: 'Variscan'; V_{ext}: 0 mm × yr^{-1}) for (a) thermomechanical and (b) thermal versions represented by the distribution of the temperatures (T) and temperature contrasts (ΔT).

of smaller size will have longer lifespans in comparison with their larger counterparts.

*4.1.2 Effect of the lithospheric type (models **10–18**)*

In order to explore the consequences of different types of overlying lithosphere, we present the three following groups of experiments characterized by (1) 'Cratonic' (models **10–12**; Fig. A5); (2) 'Mesozoic' (models **13–15**; Fig. A6) and (3) oceanic (models **16–18**; Fig. A7) lithosphere. In these models, we also vary initial plume temperature (T_{init}: 1500, 1600, or 1700 °C) while keeping its diameter constant (d_{init}: 100 km).

Fig. 10. summarizes the results for thermomechanical models (Fig. 10a) and their thermal analogues (Fig. 10b) for an unchanged initial temperature of the plume (T_{init}: 1600 °C) but different types of overlying lithosphere corresponding to the four configurations tested in our study ('Cratonic', 'Variscan', 'Mesozoic' and oceanic: models **11**, **2**, **14** and **17**, respectively). In contrast to parameters characterizing the plume itself (initial temperature and diameter; see Section 4.1.1), the type of lithosphere appears to have a much more limited impact on the evolution of w_x (horizontal width of the plume sector with $\Delta T_{max} > x$, where x varies from 200 to 50 °C). In fact, w_x variations in the thermal versions of the models are almost visually undistinguishable (Fig. 10b): 'Cratonic' (model **11**) and oceanic (model **17**) end-members give a relatively small total difference (∼15 Myr) in the plume lifespans (i.e. $t(w_{100}^{50})$) expected in these models. On the contrary, thermomechanical experiments with 'Mesozoic' (Fig. 10a2) and oceanic (Fig. 10a1) lithosphere differ by an abrupt (i.e. during the first ∼10–20 Myr) increase of w_{100} up to ∼130 and ∼210 km, respectively (resulting from a kinematic effect related to lateral spreading of the plume material below the lithosphere—see above, Section 4.1.1). In the case of oceanic lithosphere (model **17**), fast growth in w_{100} quickly doubling its initial value of 100 km is followed by an almost equally rapid drop leading to a 'premature death' of the plume: its lifespan $t(w_{100}^{50})$ of ∼65 Myr appears to be significantly shorter (by ∼35–50 Myr) than in other thermomechanical and thermal experiments presented in Fig. 10 (∼100–115 Myr). This shortening of the plume life span in the thermomechanical model is due to faster heat exchange of the moving plume body in comparison to purely diffuse cooling in the thermal model. Note, however, that under specific conditions ('Variscan' lithosphere, d_{init} of 100 km) a 'thermomechanical' plume could be, in contrast, formally 'longer-lived' than its fixed and, therefore, slower-cooled 'thermal' counterpart (see models **8** and **9** in Figs 8 and 9). As mentioned above (Section 4.1.1), this counter-intuitive phenomenon is related to initial mechanical widening of w_{100} that increases decay time $t(w_{100}^{50})$ thus paradoxically slightly (by ∼10 Myr) extending the apparent life-span of a 'thermomechanical' plume (which remains, however, 'faster-cooled' in terms of initial speed of ΔT_{max} descent below 300 and 200 °C; see Fig. 8).

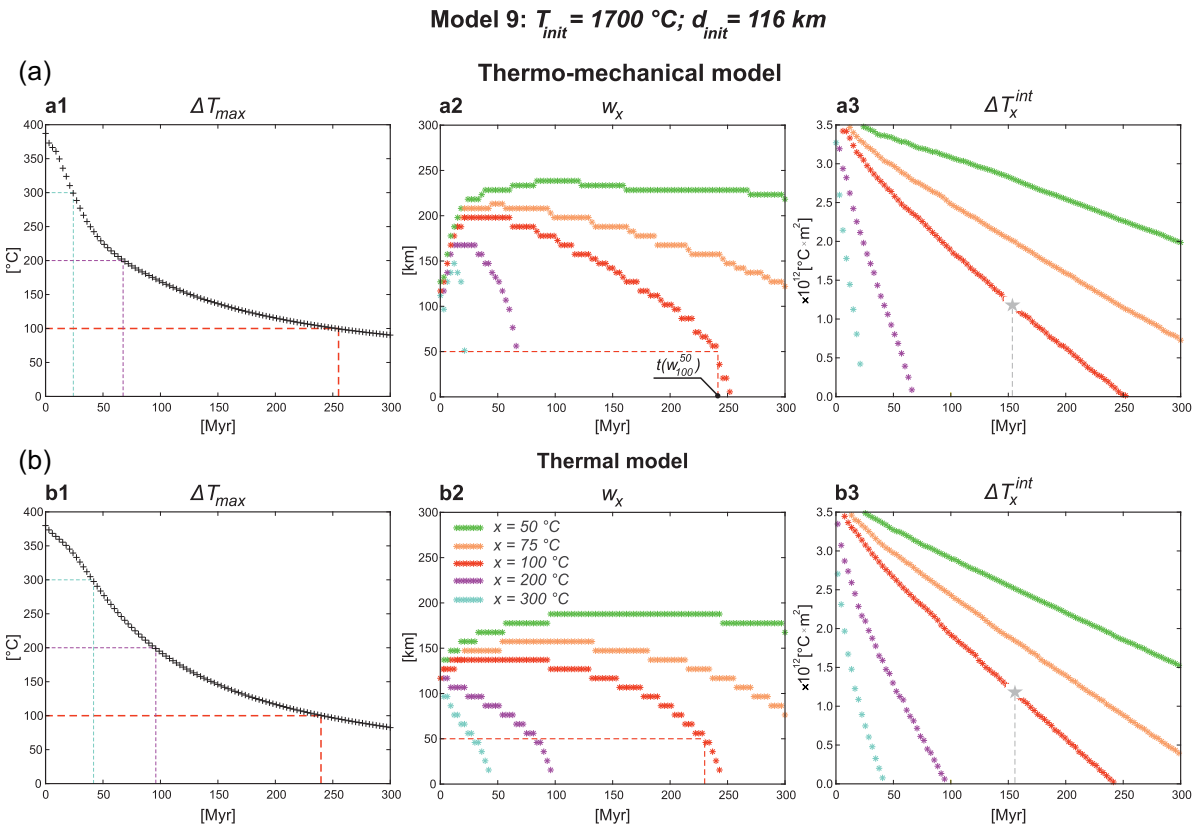

Figure 8. Temporal evolution of model **9** (T_{init}: 1700 °C; d_{init}: 116 km; type of lithosphere: 'Variscan'; V_{ext}: 0 mm × yr^{-1}) for (a) thermomechanical and (b) thermal versions represented by parameters derived from ΔT. Figure conventions as in Fig. 5.

Given that plume anomalies in all experiments shown in Fig. 10 have the same initial temperature and size (and, therefore, similar values for their buoyancies), variations in their mechanical behaviour (i.e. immovable circle under 'Cratonic' lithosphere versus uplift and horizontal stretching below an oceanic lithosphere) should be controlled by the differences in viscosity of the surrounding sublithospheric mantle. In order to characterize quantitatively the relation between buoyancy of the plume and viscosity of the asthenosphere, we use a simplified approximation of the Rayleigh number analogue (d'Acremont *et al.* 2003; Burov & Guillou-Frottier 2005) for the plume seeded underneath the lithosphere: $R'_a = \frac{g \cdot \frac{2}{3} \cdot d \iint_A \Delta\rho dA}{\chi \cdot \eta}$ where g is the gravity acceleration (9.8 m × s^{-2}), d is initial plume diameter (d_{init}: 100 km), $\iint_A \Delta\rho dA$ is the density contrast $\Delta\rho$ between plume material and its surroundings integrated over the initial plume surface A (both plume and non-plume mantle density are calculated from thermodynamic model Perple_X by Connolly 2005), χ is thermal diffusivity of the mantle (10^{-6} m^2 × s), and η is viscosity of the sublithospheric mantle defined as a function of pressure and temperature (Section 3.1, eq. 4) and, therefore, characterized by increased values in the models with thicker lithosphere because it gives higher lithostatic pressure within the asthenospheric zone of roughly equal temperatures.

Analysis of R'_a estimated for different initial plume temperatures (T_{init}: 1500, 1600 or 1700 °C; see blue, green, and red curves in the graph of Fig. 11a, respectively) seeded below different types of the lithosphere ('Cratonic', 'Variscan', 'Mesozoic' and oceanic; the horizontal axis of the graph in Fig. 11a) shows that the kinematic behaviour of the system (see compositional fields at the time slice of 15 Myr in Fig. 11b) actually depends on the relation between buoyancy of the plume and viscosity of the mantle under the lithosphere. Low values of R'_a (< 20; blue dashed ellipse in Fig. 11a) correspond to a minimum (almost negligible) mechanical component in the system evolution resulting in the circular (unchanged; models **1** and **10**–**13**) to inverted pear (slightly deformed; model **2**) plume configuration (see plots bounded by blue polygon in Fig. 11b). On the contrary, intermediate buoyancy/viscosity relations (15 < R'_a < 25; green dashed ellipse in Fig. 11a) lead to a heart-like plume shape (models **3**, **14** and **16**; green polygon in Fig. 11b) while elevated ones (R'_a > 25; red dashed ellipse in Fig. 11a) favour its further transformation with establishment of a horizontally stretched ellipse (red polygon in Fig. 11b) characterized by aspect ratios varying from ~1/3 (model **15**) through ~1/4 (model **17**) to ~1/5–1/6 (model **18**). Thus, it appears that a relatively high viscosity of subcratonic asthenosphere (i.e. mantle under 'Cratonic' lithosphere) always prevents any motions of the plume body (Fig. 11b, low row) even in the case of the hottest (and, therefore, the most buoyant) plume anomaly (T_{init}: 1700 °C; model **12**). At the same time, regardless the type of overlying plate and, therefore, viscosity of the sublithospheric mantle, a low buoyancy contrast in the models with a cold plume anomaly (T_{init}: 1500 °C) in all cases produces very limited intra-plume deformation as well (Fig. 11b, right-hand column). Only specific parameter combinations corresponding to the highest values of R'_a—that is warm to hot thermal anomaly (T_{init}: 1600–1700 °C) placed under sufficiently thin overlying lithosphere ('Mesozoic' or oceanic)—allow for significant mechanical movements of the mantle plume mass associated with its stretching and spreading below the

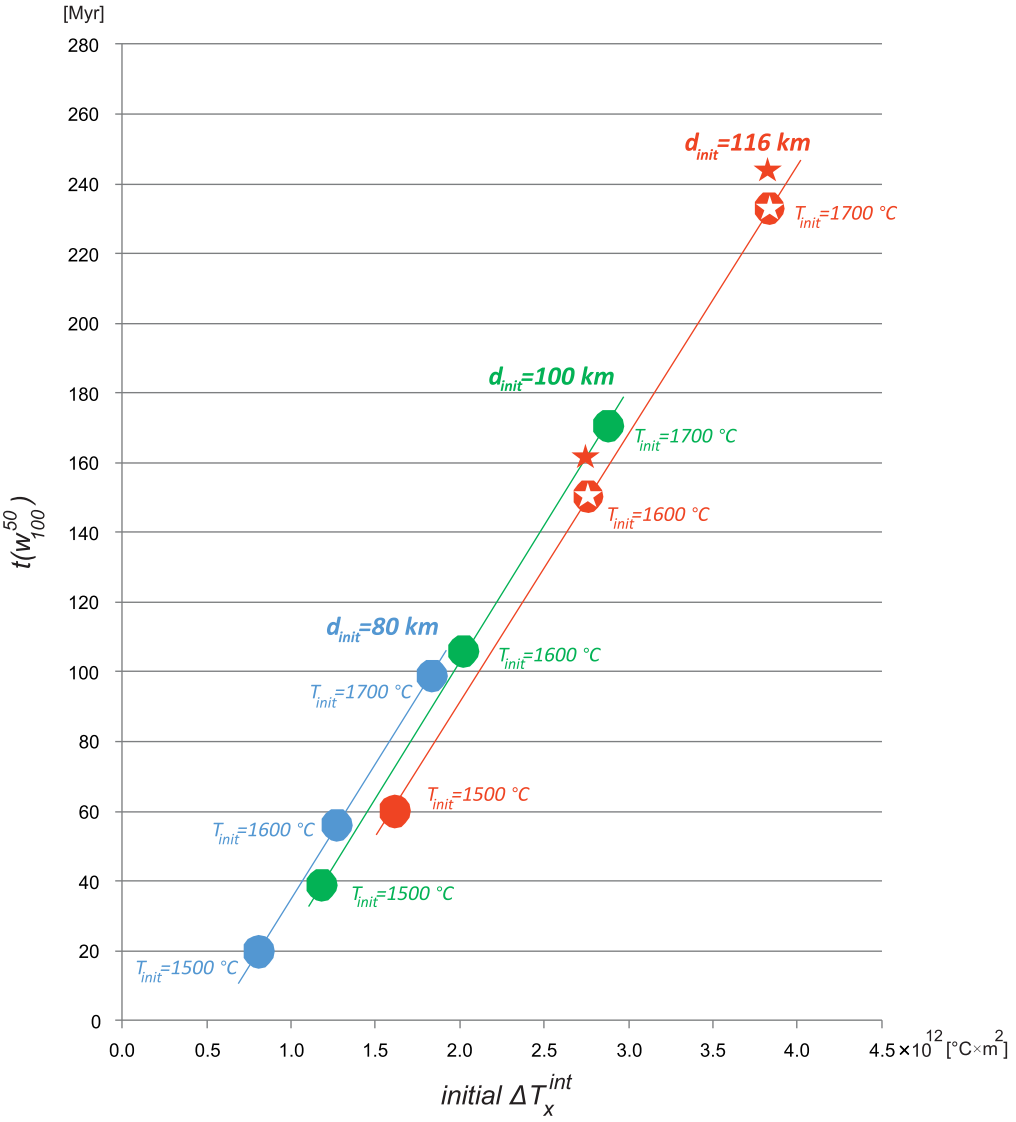

Figure 9. Models **1–9** (T_{init}: 1500–1700 °C; d_{init}: 80–116 km; type of lithosphere: 'Variscan'; V_{ext}: 0 mm × yr^{-1}): plume lifespan $t(w_{100}^{50})$ as a function of initial ΔT_x^{int}. Blue, green, and red colours correspond to d_{init} of 80, 100 and 116 km, respectively. Values obtained in thermal models are shown by circles whereas these from thermomechanical experiments (when different) are indicated by stars. Star-shaped hole inside the circle means that the value of $t(w_{100}^{50})$ for the corresponding thermomechanical experiment is different.

LAB (Fig. 11b, top right-hand corner). It is also noteworthy that in all cases the system behavior is controlled by the total thermal thickness of the overlying lithosphere (Artemieva 2006; Koptev & Ershov 2011), whereas its internal rheological stratification (Burov 2011) is irrelevant.

As mentioned above, faster cooling in the thermomechanical model **17** (T_{init}: 1600 °C; oceanic lithosphere) than in its thermal analogue leads to a significant difference (~50 Myr) in expected plume life spans: 'thermal' $t(w_{100}^{50})$ reaches ~115 Myr whereas $t(w_{100}^{50})$ in the thermomechanical version is ~65 Myr only (see green star in Fig. 12). In two other models characterized by high values of R'_a (models **15** and **18**) 'thermomechanical' $t(w_{100}^{50})$ is also reduced by ~30 and ~100 Myr, respectively (see red stars in Fig. 12). Apart from these advection-related deviations, in the experiments with the same initial plume temperature (T_{init}) the life span $t(w_{100}^{50})$ varies within a relatively narrow time interval of <30 Myr (Fig. 12). This means that in general (i.e. excluding particular cases of the highest R'_a) the type of overlying lithosphere appears to have only limited impact on the system evolution in comparison to variations in initial plume temperature and size (Section 4.1.1).

4.2 Effect of far-field tectonic extension (Models 19–42)

*4.2.1 The case of 'Variscan' continental lithosphere (Models **19–33**)*

With the aim to investigate the impact of far-field tectonic extension (V_{ext}), we test a broad range of boundary half-rates—V_{ext} of 2 mm × yr^{-1} (models **19–21**), 3 mm × yr^{-1} (models **22–24**), 4 mm × yr^{-1} (models **25–27**), 5 mm × yr^{-1} (models **28–30**) and 10 mm × yr^{-1} (models **31–33**)—for the case of an unchanged ('Variscan') type of lithosphere while varying initial plume temperatures (T_{init}: 1500, 1600 or 1700 °C).

The temporal evolution of the model **20** (T_{init}: 1600 °C; V_{ext}: 2 mm × yr^{-1}) is presented in Fig. 13. In contrast to the corresponding experiment with a neutral tectonic regime (V_{ext}: 0 mm × yr^{-1};

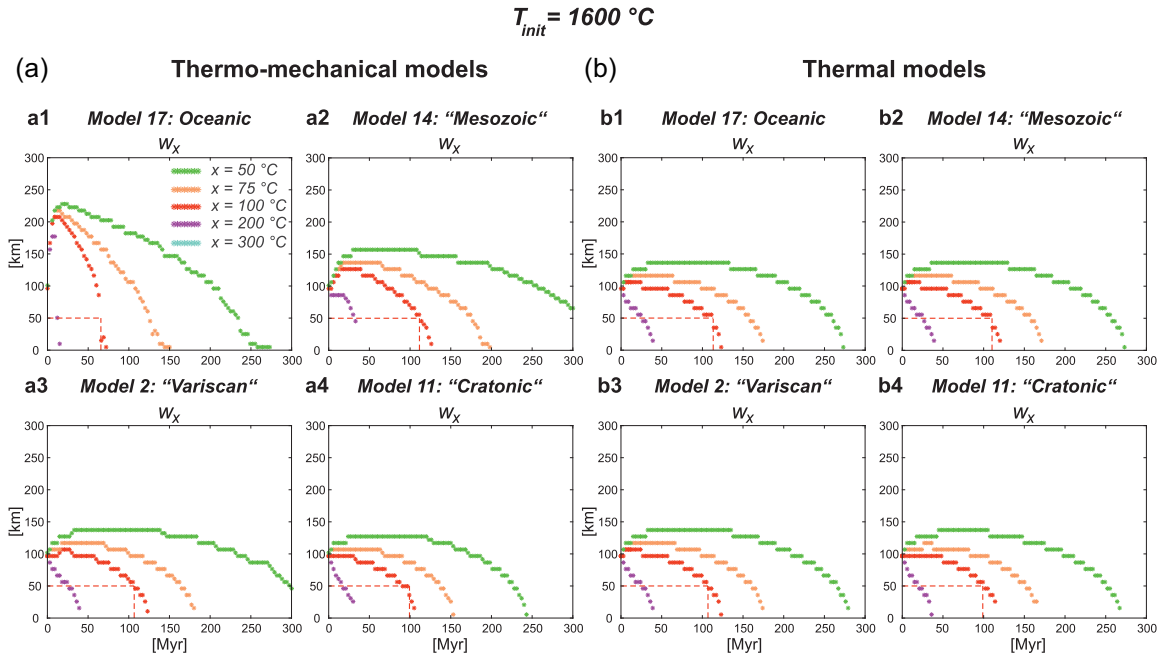

Figure 10. Temporal evolution of the experiments characterized by T_{init} of 1600 °C and different types of the lithosphere: model **17** (oceanic lithosphere; *); model **14** ('Mesozoic' lithosphere; *); model **2** ('Variscan' lithosphere; *); and model **11** ('Cratonic' lithosphere; *) for (a) thermomechanical and (b) thermal versions represented by w_x (maximum horizontal width of the area A_x where $\Delta T_{max} > 200$, 100, 75 or 50 °C). *Other experimental parameters: d_{init}: 100 km; V_{ext}: 0 mm × yr^{-1}.

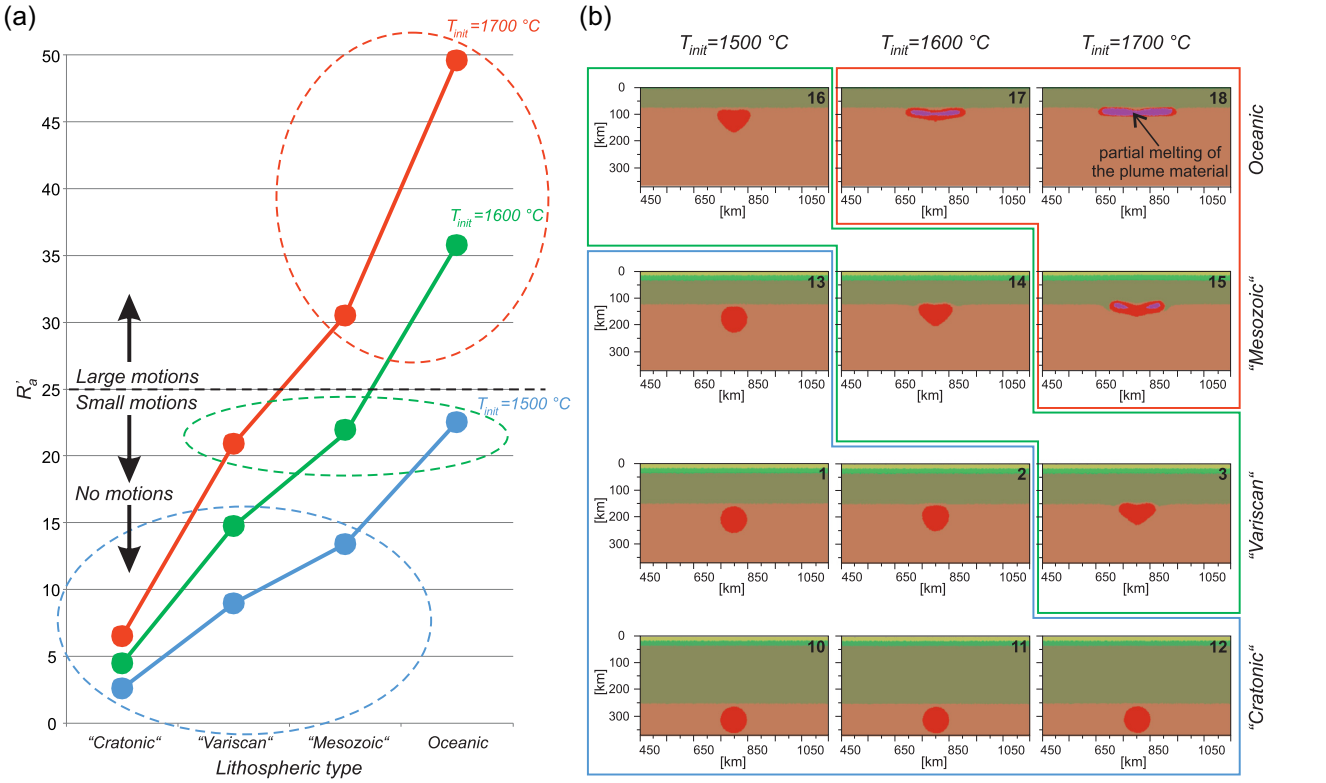

Figure 11. Models **1–3, 10–18** (T_{init}: 1500–1700 °C; type of lithosphere: 'Cratonic', 'Variscan', 'Mesozoic' and oceanic; d_{init}: 100 km; V_{ext}: 0 mm × yr^{-1}): (a) Rayleigh number analogue R'_a as a function of lithospheric type. Blue, green and red lines correspond to T_{init} of 1500, 1600 and 1700 °C, respectively. Low values of R'_a (< 20; blue dashed ellipse) correspond to a negligible mechanical component making the thermomechanical evolution almost indistinguishable from the thermal one. Therefore, further modelling efforts in exploration of such systems can be limited to the purely thermal modelling which is significantly less demanding in terms of computational resources with respect to the thermomechanical approach; (b) material phase fields at the time slice of 15 Myr. Note that in certain cases mantle plume bodies could be subjected to further modifications during subsequent time evolution (see Figs 3 and 4). The numbers of the models are indicated in top right-hand corner of each plot.

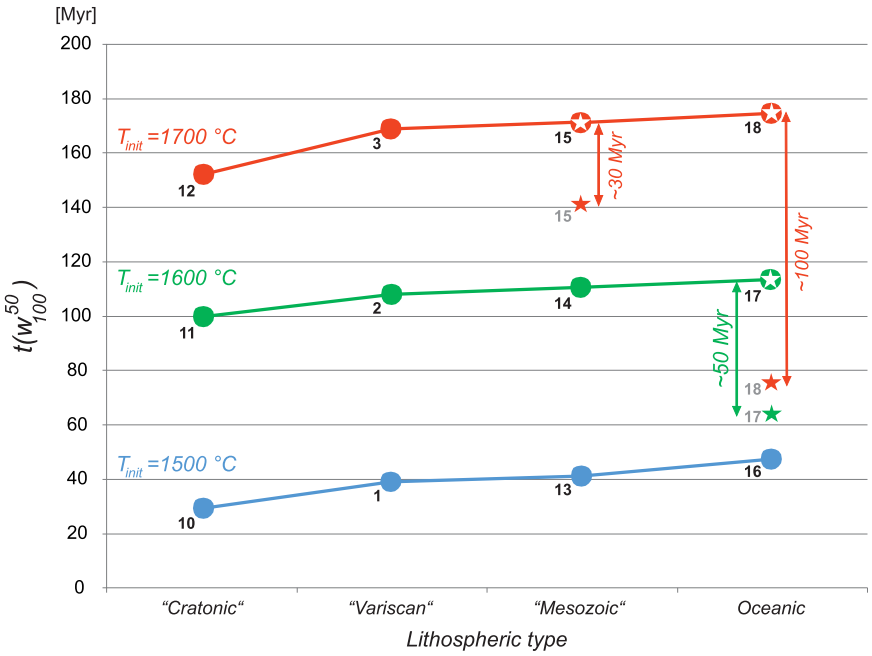

Figure 12. Models **1–3, 10–18** ($T_{\rm init}$: 1500–1700 °C; type of lithosphere: 'Cratonic', 'Variscan', 'Mesozoic' and oceanic; $d_{\rm init}$: 100 km; $V_{\rm ext}$: 0 mm × yr^{-1}): plume lifespan $t(w_{100}^{50})$ as a function of lithospheric type. Blue, green and red colours correspond to $T_{\rm init}$ of 1500, 1600 and 1700 °C, respectively. The numbers of the models are labelled. Other figure conventions as in Fig. 9.

model **2**) where the inverted pear shape of the plume does not change after ∼60 Myr (see Fig. 3), slow and constant extension applied in model **20** leads to permanent stretching of the plume body attached to the bottom of the tectonically extending lithosphere. At the final stages of the experiment the plume 'pancake' width reaches values of ∼400–500 km (Fig.13a). Brittle deformation at the crustal level which is equally distributed over the entire model domain at ∼90 Myr becomes more concentrated within the area overlying the mantle plume at ∼165 Myr to be subsequently transformed into a narrow zone of localized lithospheric thinning at ∼195 Myr (Fig. 13c). Continental break-up occurs soon after (i.e. ∼15 Myr later) at ∼210 Myr (Fig. 13a). Note that at the final stage of lithospheric rupture the asthenosphere below the break-up axis is subjected to partial melting whereas plume material attached to the LAB at both sides of the broken lithosphere remains unmelted (Fig. 13a).

The models with the same extension velocity ($V_{\rm ext}$: 2 mm × yr^{-1}) but different initial temperatures of the plume ($T_{\rm init}$: 1500 and 1700 °C; Figs A8 and A9, respectively) demonstrate similar evolutional behaviour but significantly different timing: lithospheric rupture takes place either ∼65 Myr later (at ∼275 Myr; 'cold' plume model **19**) or ∼35 Myr earlier (at ∼175 Myr; 'hot' plume model **21**) with respect to break-up time (∼210 Myr) in the model of intermediate plume temperature ($T_{\rm init}$: 1600 °C; model **20**).

In contrast to models with a tectonically neutral regime demonstrating an inexorable fading of the thermal anomaly with time, in the models with applied tectonic extension an initial decrease of ΔT_{max} (maximum temperature contrast with respect to 'standard' near-edge column; see Section 4.1.1) is followed by its accelerating growth (Figs A10–A12) due to localized uplift of plume material and/or underlying asthenosphere through the lithospheric mantle in the central part of the modelling area (Figs 13a, b and 14b). This raise in ΔT_{max} lasts until break-up during the time period varying from ∼100 to 170 Myr in the experiments with V_{ext} of 2 mm × yr^{-1} (models **19–21**) to ∼20–70 Myr when $V_{\rm ext}$ is 3 mm × yr^{-1} (models **22–24**). Higher values of $V_{\rm ext}$ (4, 5 and 10 mm × yr^{-1}) result in shorter pre-break-up phases (∼10–40 Myr) sometimes initiated immediately after onset of the experiments (i.e. without initial cooling stage when ΔT_{max} decreases). Note also that the 'pre-break-up phase' of growing ΔT_{max} is also characterized by a quick increase of w_x and ΔT_x^{int} (Figs A10–A12). Importantly, in the case of the coldest plume ($T_{\rm init}$: 1500 °C) and slowest extension ($V_{\rm ext}$: 2 mm × yr^{-1}) the initial cooling stage is characterized by a w_{100} that is less than 50 km during the time interval of ∼60–110 Myr (model **19**; Fig. A10b2). This indicates that a thermal anomaly controlling the location of the future break-up center could remain invisible in seismic tomography data for time periods on the order of tens of Myr.

The timing of lithospheric break-up (Fig. 14) appears to be mainly a function of boundary half-rate ($V_{\rm ext}$): under the slowest extension ($V_{\rm ext}$: 2 mm × yr^{-1}) break-up times always exceed 150 Myr reaching ∼175–275 Myr while they shorten by a factor of >10 (up to ∼10–15 Myr) when the rate of extension approaches the fastest value ($V_{\rm ext}$: 10 mm × yr^{-1}). The predicted impact of the initial plume temperature ($T_{\rm init}$) also decreases with the grow of $V_{\rm ext}$ (see relative positions of blue, green and red lines in Fig. 14a): when the value of $V_{\rm ext}$ is low (2 mm × yr^{-1}) the lithospheric rupture is postponed by ∼100 Myr in the 'cold' plume model ($T_{\rm init}$: 1500 °C; model **19**) with respect to its 'hot' plume counterpart ($T_{\rm init}$: 1700 °C; model **21**) whereas for $V_{\rm ext}$ of 10 mm × yr^{-1} this difference between 'hot' and 'cold' experiments (models **31** and **33**) becomes almost negligible (∼5 Myr). In the models **19–22** (break-up time is >100 Myr) mantle plume material remains unmelted whereas decompressional melting occurs within 'normal' (i.e. non-plume) sublithospheric mantle being usually confined to a depth of ∼50–75 km (Fig. 14b, upper row). On the contrary, for models **23–33** (break-up time is <100 Myr) partial melting resides exclusively within the body of the mantle plume penetrating through ruptured lithospheric mantle up to the bottom of extended and thinned crust (snapshots shown in Fig. 14b correspond to the moments in time just preceding rupture at crustal levels and establishment of oceanic spreading). Note that the volume of the plume material involved in

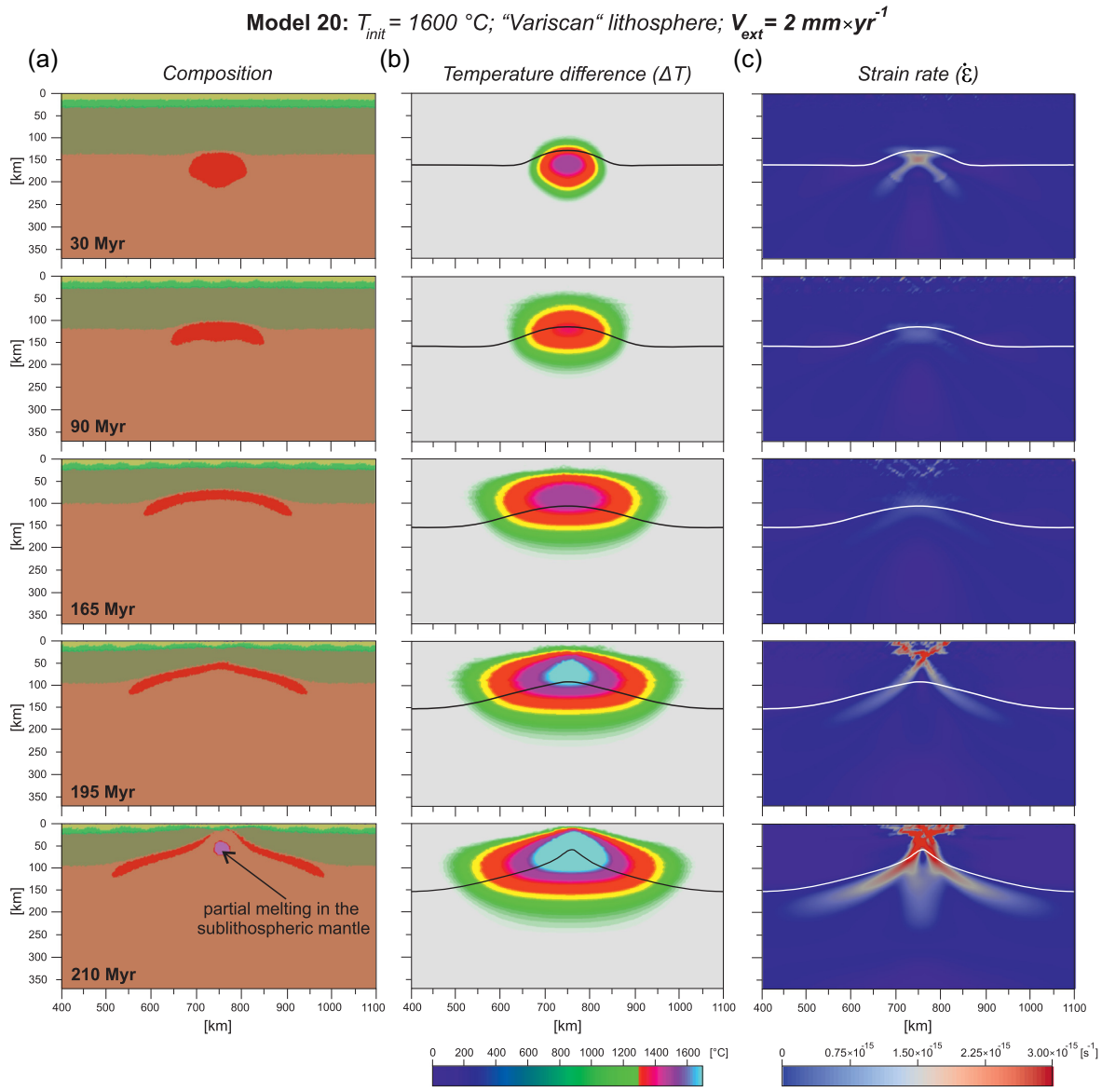

Figure 13. Temporal evolution of model **20** ($T_{\rm init}$: 1600 °C; type of lithosphere: 'Variscan'; $V_{\rm ext}$: 2 mm × yr^{-1}; $d_{\rm init}$: 100 km): (a) material phase field; (b) temperature contrasts (ΔT); (c) strain rates ($\dot{\varepsilon}$).

decompressional melting is sufficiently larger in the models with higher V_{ext} (compare models **23** and **33** in Fig. 14b). A break-up time of ∼100 Myr appears to be a 'characteristic threshold' separating the models involving and without partial melting of mantle plume material at the syn-break-up stage (Fig. 14a). We should note, however, that given some level of uncertainty in the initial thermal profile (Section 5.3) the modelled timing and extent of the melting are to be considered as estimates.

4.2.2 *Different types of lithosphere (Models **34–42**)*

In the final set of models, we analyse various lithospheric types—'Cratonic' (models **34–36**), 'Mesozoic' (models **37–39**) and oceanic (models **40–42**)—in the context of moderate values of $V_{\rm ext}$ (2, 3 or 4 mm × yr^{-1}) and invariable $T_{\rm init}$ (1600 °C).

As shown in Fig. 15 summarizing the models with slow extension ($V_{\rm ext}$: 2 mm × yr^{-1}), onset of 'pre-rift stage' (reflected in simultaneous growth in the parameters derived from temperature contrast ΔT: ΔT_{max}, w_x and ΔT_x^{int}) and subsequent break-up occur the earlier the thinner the lithosphere is: the time of break-up increases from 80 Myr in oceanic lithosphere (model **40**) through 170 Myr ('Mesozoic' lithosphere; model **37**) and 210 Myr ('Variscan' lithosphere; model **20**) to >300 Myr for the 'Cratonic' lithosphere case (model **34**).

A similar tendency (longer break-up time for thicker and stronger lithosphere) persists for $V_{\rm ext}$ of 3 and 4 mm × yr^{-1} as well (Fig. 16). Note that the most pronounced contrast in break-up time occurs for the transition from 'Cratonic' (250 km thick) to non-cratonic ('Variscan'; 150-km-thick) lithosphere whereas the difference in break-up times between the models with 'Variscan' and 'Mesozoic' lithosphere is much more limited, thus reflecting a moderate difference (by 25 km only) in their LAB depths (see model configurations for different lithospheric types in Fig. 2).

Similarly to the effect of initial plume temperatures ($T_{\rm init}$) explored in previous model series for a 'Variscan' type of lithosphere (Section 4.2.1 and Fig. 14), the role of the lithospheric structure in

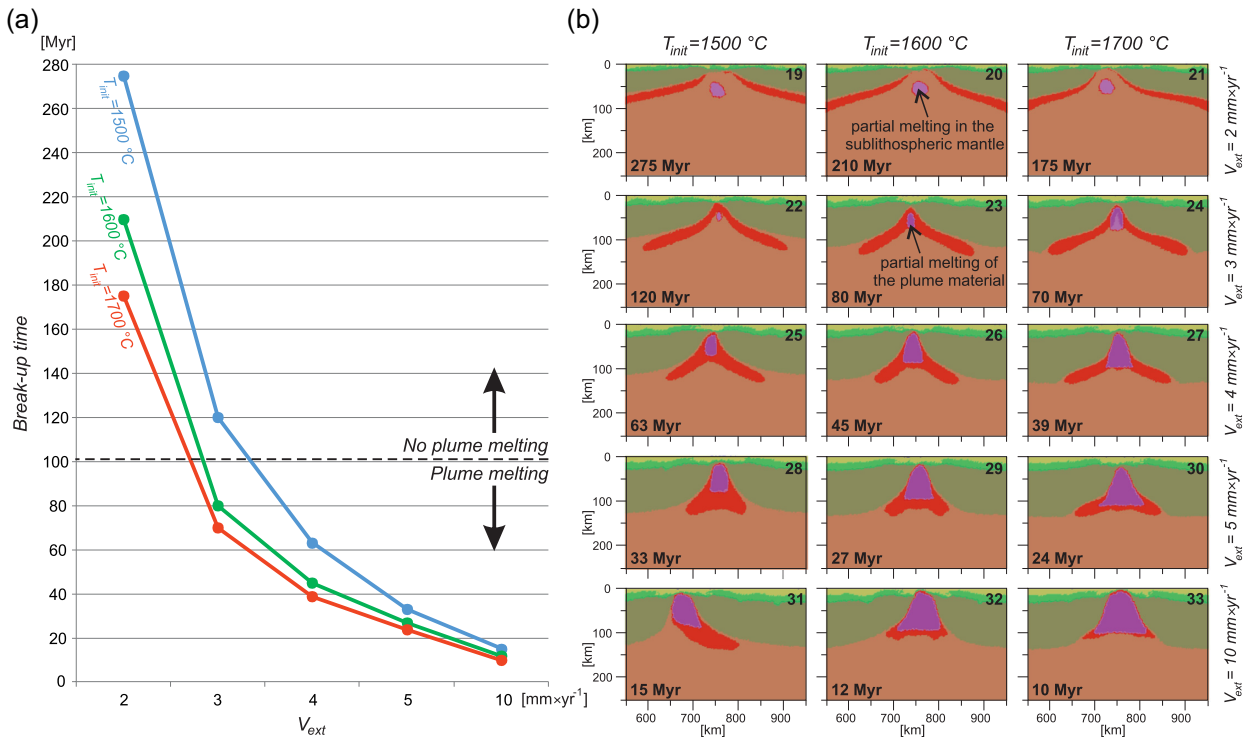

Figure 14. Models **19–33** (T_{init}: 1500–1700 °C; 'Variscan' lithosphere; V_{ext}: 2–10 mm × yr^{-1}; d_{init}: 100 km): (a) break-up time as a function of V_{ext}. Blue, green and red lines correspond to T_{init} of 1500, 1600 and 1700 °C, respectively; (b) material phase fields at break-up time. The numbers of the models are indicated in top right-hand corner of each plot.

the break-up timing becomes less pronounced when values of V_{ext} increase. Note also that a 'characteristic threshold' value for the break-up time defining the transition between melted and unmelted plumes remains to be close to ∼100 Myr (black dashed line in Figs 14a and 16).

5 DISCUSSION

5.1 Summary of numerical results

The presented numerical results show that predicted variations in the decay time of a 'baby' plume (defined by the parameter $t(w_{100}^{50})$ characterizing the time span for which the plume thermal anomaly remains seismically detectable: $\Delta T > 100$ °C; $w_{100} \geq 50$ km) mostly depend on plume buoyancy which is controlled in our models by its initial temperature (T_{init}) and size (d_{init}). In particular, expected plume life spans $t(w_{100}^{50})$ vary from ∼20 Myr when both temperature and diameter are minimum (model **4** with T_{init} of 1500 °C and d_{init} of 80 km) to ∼245 Myr when they are of maximum magnitudes (model **9** with T_{init} of 1700 °C and d_{init} of 116 km). It is also noteworthy that the sum of temperature excess defined within the seismically detectable part of the thermal anomaly ($\Delta T > 100$ °C; ΔT_{100}^{int}) for initially 'warm' (T_{init}: 1600 °C) and 'hot' (T_{init}: 1700 °C) plumes remains higher than that associated with a 'cold' (T_{init}: 1500 °C) plume at the moment of model initiation ($t = 0$ Myr) for more than tens or even 100 Myr (Figs 5 and 8).

In the experiments with extension, plumes usually persist over the entire model duration being a controlling factor in the location of lithosphere break-up (Fig. 13). We, therefore, selected as the main analysed parameter for this group of models the time span from model initiation to lithospheric break-up (Figs 14–16). Our modelling results demonstrate that the rate of applied extension appears to be the main controlling parameter of the break-up time. For slow extension (V_{ext}: 2 mm × yr^{-1}) it can exceed the maximum model span of 300 Myr (see 'Cratonic' lithosphere case in model **34**) whereas lithosphere rupture can be induced in only 10 Myr when V_{ext} is 10 mm × yr^{-1} (model **33**). The amount of plume material involved into partial melting as well as the presence of this melting at all are controlled by break-up time. For all experiments performed, a 'characteristic threshold' break-up time of roughly 100 Myr defines a transition between the models with melted and unmelted plumes. Therefore, it appears that even an initially 'cold' (T_{init}: 1500 °C) plume can produce melting under condition of sufficiently fast extension (V_{ext}: 4–10 mm × yr^{-1}) and, therefore, rapid break-up (break-up time of <100 Myr). On the contrary, a long duration of the rifting (break-up time is >100 Myr) typical for slow extension (V_{ext}: 2 mm × yr^{-1}) prevents melting in the plume even when the original anomaly was 'hot' (T_{init}: 1700 °C) restricting the melt formation only to 'normal' (depleted) asthenospheric mantle (Fig. 14b).

In summary, three striking features become apparent from our models:

1. Small-scale 'baby' plumes, despite their limited size and moderate value of initial temperature contrast, not only control the location of the break-up axis but also, when combined with sufficiently fast extension and rapid break-up, could be involved into decompressional melting during their ascent through the ruptured lithosphere in the syn-break-up phase. This could, therefore, contribute to the formation of volcanic passive margins bearing deep mantle plume geochemical signatures (Jackson *et al.* 2010, 2017). As mentioned above, initially 'warm' (T_{init}: 1600 °C) and 'hot' (T_{init}: 1700 °C) plumes can conserve the integrated temperature contrast

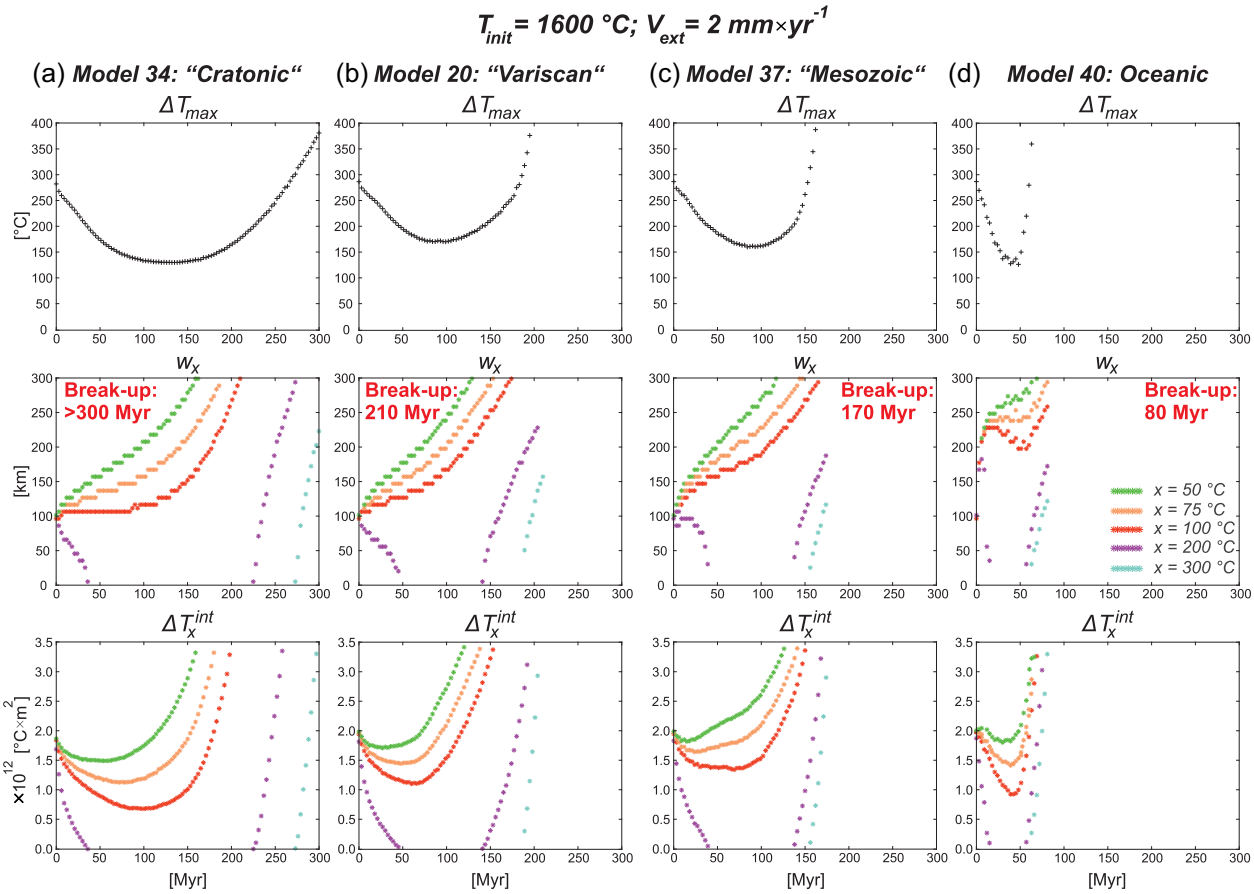

Figure 15. Temporal evolution of the experiments characterized by $T_{\rm init}$ of 1600 °C, $V_{\rm ext}$ of 2 mm × yr^{-1} and different types of lithosphere: (a) model **34** ('Cratonic' lithosphere; $d_{\rm init}$: 100 km); (b) model **20** ('Variscan' lithosphere; $d_{\rm init}$: 100 km); (c) model **37** ('Mesozoic' lithosphere; $d_{\rm init}$: 100 km) and (d) model **40** (oceanic lithosphere; $d_{\rm init}$: 100 km) represented via parameters derived from ΔT. Figure conventions as in Fig. 5.

(ΔT_{100}^{int}) which is higher or equivalent to the initial ΔT_{100}^{int} for a 'cold' ($T_{\rm init}$: 1500 °C) plume during time periods from ∼35 to ∼95 Myr (Fig. 5). This means that if a 'hot' ($T_{\rm init}$: 1700 °C) plume after about one hundred Myr of cooling would suddenly be subjected to fast tectonic extension, the evolution of this system could be quite similar to that of the model **31**: the plume is 'cold' ($T_{\rm init}$: 1500 °C) but extension is switched on immediately after its emplacement. Therefore, magmatic material at volcanic passive margins can be supplied from plume anomalies emplaced at different stages during pre-break-up history even if (i) the size of these plumes is limited and (ii) the time of their impingement is well in advance of not only the time of final break-up but even of the onset of prior tectonic extension and rifting.

2. Even for the cases when the mantle plume is not melted (under the condition of slow extension $V_{\rm ext}$ of 2 mm yr^{-1} with resulting break-up time in excess of 100 Myr) its initial location remains a controlling factor for positioning the break-up axis (rupture of the lithosphere always occurs directly above or close to the initial site of the plume—see Fig. 14b). Thus, it appears that an amagmatic passive margin could be formed due to this hidden effect of the mantle plume which was faded before break-up, not leading to plume-related magmatism usually observed at volcanic rifted margins. In this context, it should be noted that frequently in 'passive' rifting/break-up models a small temperature heterogeneity is applied at the bottom of the lithosphere at the site of the prospective rift (e.g. Gerya 2013b; Brune 2014). This could actually correspond to our fading 'baby' plume below the location of future break-up. Therefore, the question is raising on the actual 'passivity' of these classic 'passive' rifting models and, in particular, how rifting can be considered 'passive' when its location (being one of its key characteristics) is controlled by a thermal anomaly that could be of deep origin.

3. In a tectonically neutral regime in the overlying plate, the decay time of a 'baby' plume defined as $t(w_{100}^{50})$ can vary from 20 Myr to more than 200 Myr. Such a large temporal variability in the life span of small-scale plumes could explain why sometimes (e.g. Bohemian Massif) low-velocity anomalies reside at relatively shallow depths (200 km) without evidence for a plume tail below (Plomerová *et al.* 2007, 2016). In this case, the plume head attached to the bottom of the lithosphere could be shifted with respect to its original feeding channel (plume tail) due to lateral movements of the tectonic plates over geological time. This also implies that small-scale mantle diapirs below crustal magma chambers punctuated every 50–150 km along volcanic rifted margins are not a mandatory result of shallow convection within the uppermost asthenosphere as hitherto supposed (Geoffroy 2001, 2005) but could be potentially linked with deeper laterally displaced sources. This also points to a younger age for 'finger-like' 'baby' plumes such as detected under the Eifel volcanic fields and associated with present-day seismicity (Hinzen *et al.* 2007), active topographic uplift (Kreemer *et al.* 2020), Quaternary magmatic activity (Buikin *et al.* 2005) and mantle degassing (Berberich *et al.* 2019).

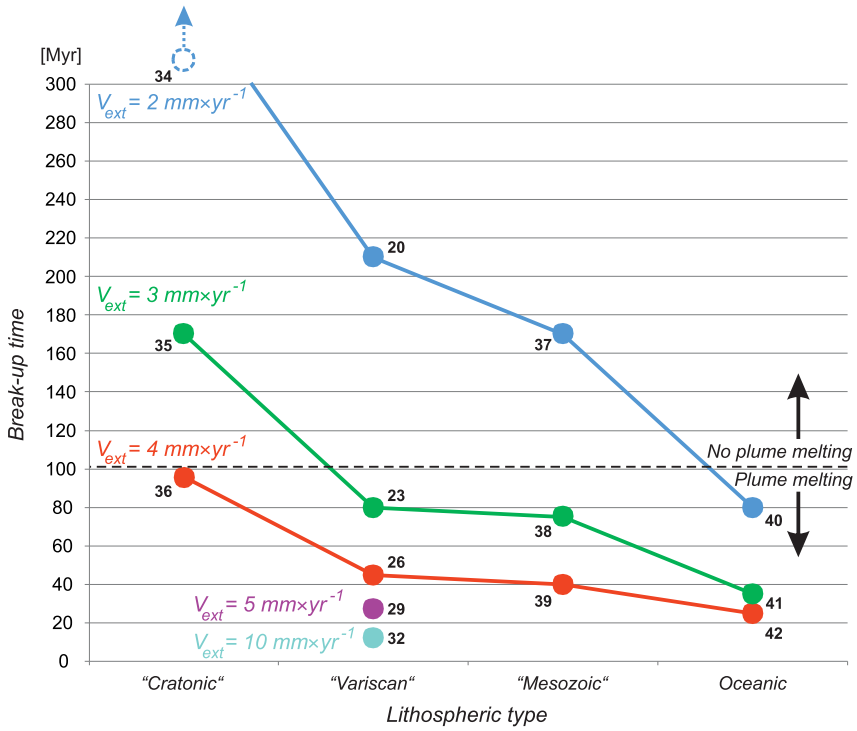

Figure 16. Models **20**, **23**, **26**, **29**, **32**, **34–42** (T_{init}: 1600 °C; type of lithosphere: 'Cratonic', 'Variscan', 'Mesozoic', oceanic; V_{ext}: 2–10 mm × yr^{-1}; d_{init}: 100 km): break-up time as a function of lithospheric type. Blue, green and red lines correspond to V_{ext} of 2, 3 and 4 mm × yr^{-1}, respectively. Magenta and aqua colours refer to the models of 'Variscan' lithosphere with V_{ext} of 5 and 10 mm × yr^{-1}. The numbers of the models are labelled.

5.2 Implications for modes of rifting and break-up

Our findings lead us to propose a new classification for the modes of continental rifting (Table 3). In doing so we complement the old classification separating 'passive' rifting (amagmatic, non-plume) from 'active' rifting (magmatic, plume-activated). Previously, several studies attempted to reconcile these end-member views. In particular, it was demonstrated that initially 'passive' extension and thinning of the lithosphere triggers convective upwelling of the asthenosphere during which thermal buoyancy may dominate the far-field intraplate stresses thus causing a change of the rifting mode to 'active' (Huismans *et al.* 2001). On the other hand, studies by Burov & Gerya (2014) and Koptev *et al.* (2015, 2016) have shown that in the scenario of ('active') mantle plume upwelling from the lower mantle the simultaneous presence of external ('passive') tectonic extension is a necessary prerequisite for localizing rifting deformation. Both these attempts to reconcile 'active' and 'passive' conceptions end up with the recognition of the importance of a so-called 'active/passive' mode when far-field forcing and mantle upwelling are acting together. Here we complement the concepts of 'active' and 'passive' with two principally new modes of rifting and break-up: 'semi-active' and 'semi-passive'. These new modes explain observed deviations from predictions of the end-member models (Fig. 17). In the following, we describe the key characteristics of these four different modes of 'active', 'passive' and 'semi-active' and 'semi-passive' rifting/break-up and provide natural examples for each of them (Table 3).

In the 'active' scenario (Fig. 17a), ascent of a large-scale hot/buoyant plume from the deep mantle initially results in symmetrical domal topographic uplift of the order of a few km (Şengör 2001). This is followed by a phase of widespread magmatism related to decompressional melting of the hot plume material spreading below the lithosphere (Campbell & Griffiths 1990). Subsequently, the gravity effect of dynamic topography in combination with a horizontal drag at the base of the lithosphere imparted by radial flow of the plume head induces an 'active' extension of the overlying lithosphere (Westaway 1993). Therefore, the main criterion of the 'active' (plume-induced) mechanism is the presence of plume-related (i.e. bearing corresponding geochemical signatures) magmatic events preceding the onset of the deformation associated with rifting (Şengör & Burke 1978). Some recent studies have pointed out that during fragmentation of Pangea, the most recent of Earth's supercontinents, extensional deformation in the areas of future continental break-up has been initiated before emplacement of corresponding LIPs, thus excluding 'active' mechanisms throughout Pangea dispersal (Peace *et al.* 2020 and references herein). However, it was also shown that in many cases pre-magmatic rift basins have orientations which are oblique to future passive margins, thus indicating that pre-LIP rifting and LIP-related continental break-up might be tectonically independent (Guan *et al.* 2021). For example, on the one hand, the Colorado Basin, Salado Basin and Punta del Este Basin in South America/South Africa are formed since the Early Jurassic (Max *et al.* 1999; Franke *et al.* 2006) indeed preceding the Parana-Etendeka LIP event which is roughly coeval with the Early Cretaceous break-up in South Atlantic (Franke 2013). On the other hand, these pre-LIP rift basins are oriented transversal with respect to the present passive margins thus advocating in favour of an 'active' scenario when mantle plume impingement not only results in a voluminous magmatic event (Parana-Etendeka LIP) but also generates extensional stresses which are (1) characterized by principally different orientation with respect to that most prevalent

Table 3. Modes of rifting and break-up.

Mode of rifting and break-up	Pre-break-up widespread magmatism: Large Igneous Provinces (LIP)	Syn-break-up volcanism: seaward-dipping reflectors (SDRs)	Syn-rift intrusive magmatism: high velocity lower crust bodies	Examples: Break-up area (associated LIP, if applicable)
'Active'	Yes: preceding onset of rifting or changing extension direction	Yes	Yes	South Atlantic (Parana-Etendeka) India—Madagascar (Madagascar) India—Seychelles (Deccan) Arabia—Africa (Afar)
'Semi-active'	No or Yes but preceded by rifting co-directional with final break-up	Yes	Yes	Central Atlantic (CAMP) South Africa—Antarctica (Karoo) North Atlantic (NAIP)
'Semi-passive'	No	No	Yes	Northern South Atlantic (Parana-Etendeka?) Australia—Antarctica (Kerguelen?)
'Passive'	No	No	No	Iberia—Newfoundland Equatorial Atlantic South-East India—Antarctica

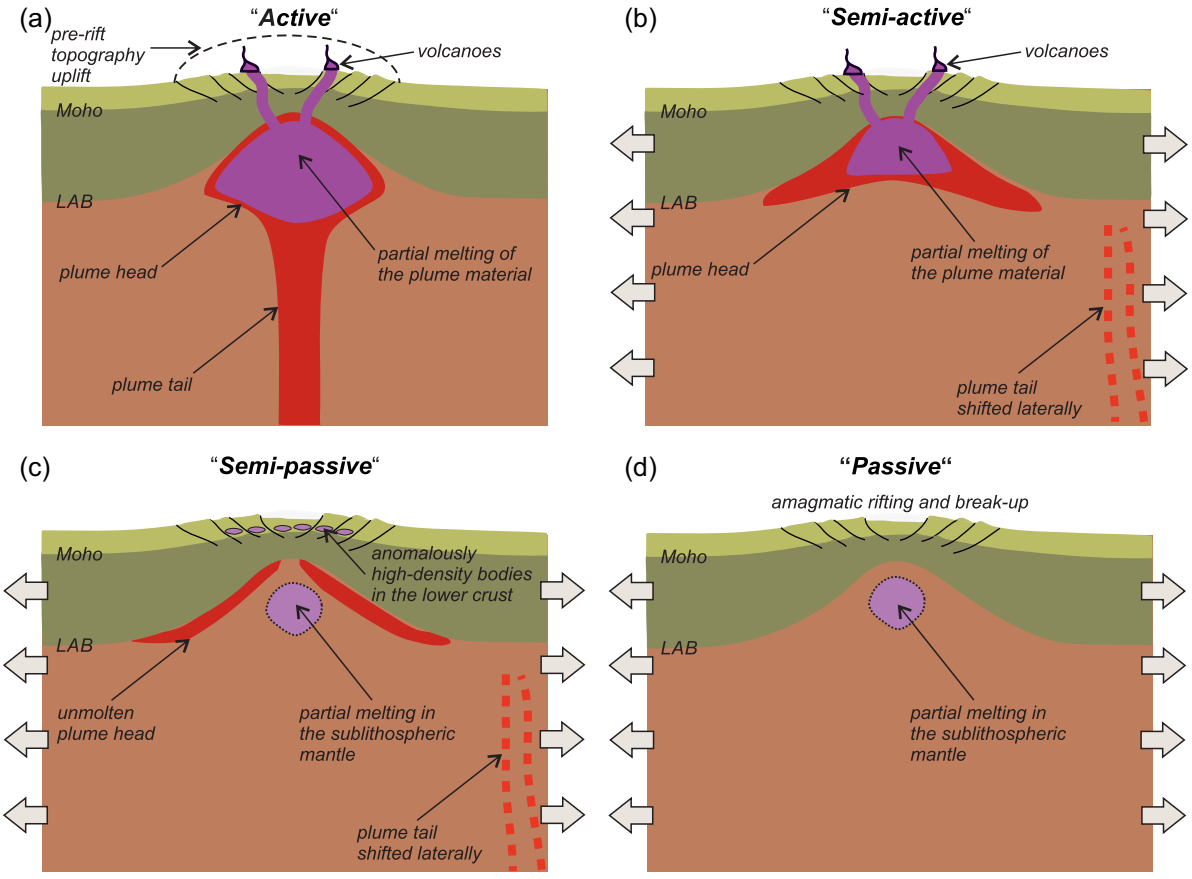

Figure 17. Four types of continental rifting and break-up according to a proposed new classification: (a) 'active'; (b) 'semi-active'; (c) 'semi-passive' and (d) 'passive'. In intermediate 'semi-active' and 'semi-passive' scenarios, extension and rupture of the continental lithosphere is mainly produced by far-field tectonic forces but in presence of 'secondary' mantle plume(s) of moderate temperature and size seeded below passively extended lithosphere. The 'semi-active' mode is characterized by syn-break-up volcanism carrying geochemical signatures of the deep mantle. On the contrary, lithospheric rupture operated by a 'semi-passive' mechanism occurs without aerial flood basalt eruptions but might be assisted by magmatic intrusions/underplating at the level of the lower crust.

before plume arrival and thus independent from the previous geodynamic regime controlling 'passive' extension and rifting and (2) sufficient to trigger continental break-up and subsequent opening of the ocean in the South Atlantic (Guan *et al.* 2021). Similar spatial and temporal relationships between pre-magmatic rifting, LIPs, and syn- or post-magmatic break-up can be also found in the areas of separation between India and the Seychelles (Deccan LIP; ~65 Ma) and Arabian Peninsula and Africa (Afar LIP; ~30–25 Ma), which are proven to be induced in an 'active' mode by sublithospheric mantle upwelling (Guan *et al.* 2021). The split between

India and Madagascar at ∼84 Ma (Coffin & Rabinowitz 1988; Müller *et al.* 1997) which is, according to all evidence, linked to the Madagascar LIP emplaced during 91–83 Ma interval (Torsvik *et al.* 1998, 2000; Cucciniello *et al.* 2010, 2021) could be another example of 'active' break-up contributing to fragmentation of Pangea. An additional argument in favour of a 'primary' plume origin for the Parana-Etendeka, Madagascar and Deccan LIPs is that they mark the spatial and temporal beginning of well-known oceanic hotspot tracks: Tristan (Gassmöller *et al.* 2016), Marion (Georgen *et al.* 2001) and Réunion (Bredow *et al.* 2017), respectively. The hotspot track created by the Afar plume on the continental part of the African plate has been also recently restored by means of global models of mantle convection (Hassan *et al.* 2020).

In contrast to the 'active' mechanisms described above, the 'passive' scenario (Fig. 17d) assumes neither (1) topographic uplift and widespread magmatism predating onset of rifting nor (2) large amounts of syn-break-up volcanism. Such a purely 'passive' rifting-to-break-up system evolves into non-volcanic passive margins (Wilson *et al.* 2001; Müntener & Hermann 2001; Pérez-Gussinyé *et al.* 2006) which are usually in contrast with volcanic passive margins (Skogseid 2001) characterized by concentrated volcanism coeval with plate break-up (Geoffroy 2001, 2005) forming large and thick wedges of so-called Seaward Dipping Reflectors (SDRs). These are clearly recognizable in seismic sections (Mutter *et al.* 1982; Franke *et al.* 2007; Funck *et al.* 2017; Jolivet *et al.* 2018) and frequently floored by high velocity bodies in the lower crust, with *P*-wave velocities of more than 7.0 km × s^{-1} (Mutter & Zehnder 1988; Schlindwein & Jokat 1999; Schnabel *et al.* 2008; Mjelde *et al.* 2016), which are interpreted as a result of magmatic intrusions/underplating (White *et al.* 2008; Mjelde *et al.* 2009). The conjugate Newfoundland-Iberia (Bronner *et al.* 2011; Brune *et al.* 2017; Peace *et al.* 2017), Equatorial Atlantic (Azevedo 1991; Basile *et al.* 2005; Heine & Brune 2014), and South-East India (Nemčok *et al.* 2013; Sinha *et al.* 2016; Tugend *et al.* 2020) passive margins represent the most typical examples of non-volcanic (magma-poor and, therefore, SDRs-free) passive margins (Table 3), likely formed in a purely 'passive' tectonic regime without any sign of related plume activity.

During fragmentation of Pangea, several break-up regions show a mixture of characteristics between 'active' and 'passive' end-members described above. The most prominent example of such 'intermediate' behaviour is the opening of Central Atlantic Ocean corresponding to the earliest break-up episode in Pangea. Seafloor spreading started in the Central Atlantic at around 195–175 Ma (Klitgord & Schouten 1986; Sahabi *et al.* 2004; Labails *et al.* 2010), almost contemporaneously with a significant magmatic event, namely the Central Atlantic Magmatic Province (CAMP; Marzoli *et al.* 1999) at ∼200 Ma (Leleu *et al.* 2016). Similar to many other areas of Pangea dispersal, continental rifting around the Central Atlantic was initiated before the emplacement of CAMP: formation of Triassic basins within the Appalachian orogenic suture (Swanson 1986) started earlier than 230 Ma (Olsen 1997). However, in contrast to, for example, the South Atlantic rifting-to-break-up system (see above), these Triassic pre-magmatic basins are oriented parallel to future volcanic passive margins formed by syn-LIP magmatic break-up in Early Cretaceous (Guan *et al.* 2021) at odds with a scenario advocated for 'active' segments of Pangea break-up where plume-induced forces leading to lithosphere rupture are tectonically independent (and thus oriented differently) with respect to those governing a prior phase of 'passive' extension. Combined with the lack of evidence for pre-LIP uplift, these observations currently fuel 'antiplume' conceptions and views on the mechanisms of the continental break-up in the Central Atlantic (Peace *et al.* 2020). However, geochemical investigations of CAMP dolerite dikes (Cebria *et al.* 2003) and of the oldest basalts sampled from the Central Atlantic oceanic crust (Janney & Castillo 2001) display clear isotopic and chemical signals of plume contamination.

In order to reconcile these apparent contradictions, we introduce here a new, 'semi-active' mode of continental rifting and break-up (Fig. 17b). This mode assumes extension and rupture of the plate produced by far-field tectonic stresses but in the presence of mantle plume(s) of modest size and temperature seeded below passively stretched lithosphere. In this scenario, thermal anomalies are initially of deep origin as equivalent to the 'secondary' plumes in the 'Courtillot Earth' (Fig. 1a). Given their relatively small size and moderate temperature contrast, 'secondary' plumes are not able to produce by their impingement either high domal topography or intensive widespread magmatism. However, as shown by our modelling, even extremely small end-members of these thermal anomalies corresponding to so-called 'baby' plumes with a characteristic diameter of the order of only 100 km might be preserved below the lithosphere during very long time spans varying from tens to hundreds Myr (Section 4.1). During such long time intervals the heads of these plumes which remain attached to the lithosphere after their emplacement could be significantly shifted with respect to their original sources in the lower mantle or MTZ due to plate movements. As demonstrated by our experiments, in the case of (re-)activation of a tectonic extensional regime by far-field tectonics, small and isolated thermal anomalies can be sufficient to localize deformation in the overlying lithosphere (Section 4.2). In the case of narrow spacing between these anomalies, they are able to interconnect the areas of localized stretching along-strike to form a continuous zone of continental break-up (Gac & Geoffroy 2009). Moreover, under condition of sufficiently high temperature excess and sufficiently fast transition to lithospheric rupture, the syn-break-up phase is accompanied by partial melting of plume material (Section 4.2; Fig. 14) leading to intensive volcanism concentrated at the ocean-continent boundary accompanied by formation of SDRs, the main indicator of volcanic passive margins. In case of thermal anomalies of slightly larger sizes than adopted in our models and in the study by Gac & Geoffroy (2009), pre-break-up thinning of the lithosphere would be also accompanied by plume-related magmatism, potentially even more voluminous and widespread, corresponding to LIPs erupted directly before the start of SDRs emplacement as observed in the Central Atlantic (Davis *et al.* 2018). Therefore, the 'semi-active' mechanism permits reconciliation of two (and apparently contradictory) lines of thinking which include: (1) prolonged tectonic activity which started in the Central Atlantic >30 Myr before CAMP magmatism and subsequently evolved to break-up without a change in extension direction after LIP emplacement and (2) the presence of magmatic rocks with depleted mantle plume geochemical signatures. Extremely voluminous and widely spread magmatism associated with CAMP (McHone 2003; Marzoli *et al.* 2018) can be thus explained by an ensemble of numerous 'secondary' plumes originally emerging from the deep-sourced 'primary' plume stagnated below the upper mantle transitional zone (Courtillot *et al.* 2003).

Interestingly, present-day hotspots in the adjacent oceanic area—Azores, Canaries, and Cape Verde (Córdoba & Ballmer 2019, 2021)—have been interpreted as 'secondary' plumes extending from a large thermal anomaly ponding beneath the endothermic 660 km phase transformation (Saki *et al.* 2015). Note, however, that these volcanic islands and seamounts are much younger than the Central Atlantic break-up (Geldmacher *et al.* 2005; Silveira *et al.* 2006; Long *et al.* 2020) and, therefore, no volcanic plume track from

CAMP is evident, in contrast to the LIPs associated with an 'active' break-up mechanism (see above). This might be explained by ancient emplacement of CAMP-related 'secondary' plumes (prior to break-up and, probably, even prior to onset of the rifting). As mentioned above, during the time interval between impingement of the mantle plumes at the lithosphere-asthenosphere boundary and their surface manifestation (LIP eruption), the feeding source in the lower mantle could be either exhausted or considerably shifted laterally due to horizontal motion of the lithosphere, thus precluding generation of a time-progressive hotspot track over newly-forming oceanic lithosphere.

Continental rupture between South Africa and Antarctica (Veevers 2012) and opening of the North Atlantic (Lundin & Doré 2005) could be other natural examples of the 'semi-active' rifting mode (Table 3). There, thin-skinned plate tectonics accomplished by exploitation of inherited suture zones provides the main control on the location and timing for both rifting and break-up processes, which are, nevertheless, accompanied by voluminous magmatism with plume-related geochemical signatures: Karoo LIP (Ellam *et al.* 1992; Duncan *et al.* 1997; Riley *et al.* 2005) and North Atlantic Igneous Province (NAIP; Saunders *et al.* 1997; Storey *et al.* 2007), respectively.

Finally, as shown by our modelling, the rupture of the lithosphere is not always accompanied by decompressional melts of mantle plume material. Under the condition of a relatively cold initial plume and slow tectonic extension, continental break-up is preceded by a long-lasting rift phase and thus occurs when the initial thermal anomaly becomes too cool to be subjected to partial melting even at the stage of lithospheric rupture when the plume material was uplifted and reached the shallowest depth levels (Fig. 14). In this case, the system evolves with only a small-volume of melting in deeper, non-plume, sublithospheric depleted mantle and likely resulted in minor to no syn-break-up volcanism. We call this regime a 'semi-passive' mode of rifting and break-up (Fig. 17c) as the location of the break-up axis is still controlled by a thermal anomaly of potentially deep origin ('secondary' mantle plume) but rupture of the lithosphere occurs without extrusion of large volumes of volcanic rocks. As a result, break-up in a 'semi-passive' regime evolves into non-volcanic (SDRs-free) passive margins, similarly to the 'passive' mode and in contrast to 'active' and 'semi-active' scenarios characterized by development of volcanic (SDRs bearing) passive margins (see above).

At first sight, the 'semi-passive' mode seems to be difficult to distinguish from a purely 'passive' mechanism based on available data for structural characteristics of passive margins. As mentioned above, aerial flood basalt eruptions leading to formation of SDRs are usually assisted by magmatic intrusions/underplating reflected in the high velocity bodies residing at the level of the lower crust along the volcanic passive margins. However, similar high velocity lower crust anomalies are also detected along non-volcanic (i.e. deprived of SDRs) passive margins: for example, in the northern part of the South Atlantic to the north of the Florianopolis (also referred to as Rio Grande) fracture zone (see e.g. Beniest *et al.* 2017a). According to Dupré *et al.* (2011), the underplated high density lower crust layer beneath the Gabon margin might be related to magmatism caused by the impact of a 'high thermal anomaly', which resides in the mantle part of the lithosphere since the early stage of rifting (Dupré *et al.* 2007). We attribute this 'high thermal anomaly' to 'secondary' mantle plume(s) potentially linked to the same source as the adjacent Parana-Etendeka LIP. Derived from partial melting of plume rocks during the rifting, the mafic magmas were intruded through a system of sills and dykes into the lower crust thus forming zones of anomalous seismic velocity. The following continental break-up, however, operated in a non-volcanic mode because plume material was cooled down before it reached the surface, in accordance with the 'semi-passive' scenario described above. Therefore, a possible criterion to identify a 'semi-passive' break-up regime could be the presence of anomalously high velocity/high density bodies located in the lower crust of non-volcanic margins, in contrast to totally amagmatic (or quasi-amagmatic) passive margins corresponding to a purely 'passive' mode.

Another example of 'semi-passive' break-up could be the separation between East Antarctica and Australia. Although East Antarctica and Australia have been connected since the Proterozoic in the Mawson-Gawler Craton (Flinn *et al.* 2006; Boger 2011), they were rifted obliquely to all Gondwana's orogenic structures and split at 99–84 Ma (Seton *et al.* 2012; Williams *et al.* 2013), at first sight, without evident plume influence (see review by Buiter & Torsvik 2014 and references herein). However, given the presence of a small amount of syn-rift magma intruded in the crust (Ball *et al.* 2013), the sublithospheric component of mantle activity, presumably associated with the Kerguelen plume (e.g. Coffin *et al.* 2002; Bredow & Steinberger 2018), can be suspected to be involved. The 'semi-passive' mechanism is, therefore, extremely important for understanding break-up in the areas where it does not follow pre-existing weak sutures. In particular, the role of 'hidden' plumes, which control the localization of deformation in the lithosphere and, therefore, define the position of rifting and break-up center but do not leave any volcanic evidences of its presence and participation, deserves to be explored in more detail in future research.

5.3 Model limitations and future perspectives

The 2-D approach adopted in this study lacks consideration of 3-D phenomena such as: (1) the alignment of the plume 'pancake' head with the rift axis (Burov & Gerya 2014) sometimes associated with irregular along-strike structure of the fault zone (Koptev *et al.* 2018b, c); (2) fast and distal propagation of hot plume material toward the areas remote from its initial emplacement (Ebinger & Sleep 1998; Faccenna *et al.* 2013; Koptev *et al.* 2017; François *et al.* 2018) and (3) oblique (Brune *et al.* 2012; Brune & Autin 2013) and/or multidirectional (Georgen 2011; Dordevic & Georgen 2016) tectonic extension which can act as selector between successful ocean basin formation and failed rifts (Heine & Brune 2014) and/or as a potential mechanism for (plume-triggered) initiation of a divergent triple junction (Gerya & Burov 2018; Koptev *et al.* 2018d). Although the relative importance of the aforementioned phenomena could be limited in the case of small-scale plumes with respect to their large-scale counterparts, the role of 'baby' plumes in lithospheric break-up warrants thorough further examination in forthcoming 3-D studies.

More detailed modelling procedures are also needed to evaluate the impact of uncertainties in the initial thermal profile of the lithosphere and sublithopsheric mantle. In particular, radiogenic heat generation in the continental crust is known to vary greatly across different tectonic units (Artemieva & Mooney 2001), thus requiring a systematic analysis of such parameters as near-surface heat production and characteristic depth of heat source distribution (Koptev *et al.* 2021). Moreover, variations in estimates of the adiabatic gradient for the asthenospheric (convecting) mantle from 0.3 °C km^{-1} (Turcotte & Schubert 2002; Sleep 2003) to 0.5 °C km^{-1} (Stixrude & Lithgow-Bertelloni 2005; Katsura *et al.* 2010) are also to be taken into account in future modelling studies. Finally, the temperature at the lithospheric base could have been adjusted to include the adiabatic gradient across the whole model depth (including the

conductive lithosphere). This would ensure similar values of the potential mantle temperature in the experiment with different LAB levels.

Future studies of 'baby' plumes and their role in plate tectonics and geodynamics are not limited to the consequences of their impingement at the base of the lithosphere. Various scenarios and mechanisms for the origin of such small-scale plume anomalies should be explored in different tectonic and geodynamical settings. Particular attention needs to be paid to the upwelling rates of 'secondary' plumes in the upper sublithospheric mantle as it might be the key factor controlling excess temperatures at the moment of their emplacement at the lithosphere-asthenosphere boundary (probably, the most uncertain parameter in the study presented here). In addition, buoyancy of a small-scale thermal anomaly and, therefore, mode of its interaction with the overlying lithosphere could be affected by the presence of plume conduit(s) in the upper and, potentially, lower mantle. Therefore, thermomechanical modelling of mantle plumes which are relatively small in terms of their horizontal extent but which are continuously 'fed' from below represents an extremely important and promising topic in geodynamics for further investigation.

6 CONCLUSIONS

We present the results from the first systematic parametric analysis focused on the life-cycle of small-scale thermal upper mantle anomalies (so-called 'baby' plumes) and their impact on the style of lithosphere rifting and continental break-up. In this study, we have tested four controlling parameters including: (1) temperature and (2) diameter of the plume, (3) rheological structure of the overlying lithospheric plate and (4) style of intraplate tectonics. From this, we draw the following conclusions:

1. Under a tectonically neutral regime, the life span of 'baby' plumes is mainly conditioned by their buoyancy (which, in turn, depends on initial size and temperature), varying over a wide range of time intervals (from ∼20 to >200 Myr). Seismically detectable thermal anomalies can thus be sustained over geologically long timescales (>100 Myr).
2. In the case of extensional tectonic settings, even relatively small (100 km diameter) and moderately hot (temperature contrast of 150–200 °C) thermal anomalies ('baby' plumes) are shown to be sufficient to localize deformation in the lithosphere directly above them, triggering rifting and subsequent break-up.
3. The duration of the pre-break-up stage (time interval between onset of extension and lithosphere break-up) is a function of the level of external stresses, initial temperature of the plume and the integrated strength of the overlying lithosphere, varying from 10 to >300 Myr.
4. Lithospheric rupture in the experiments with a long-lasting phase (a few hundreds of Myr) of pre-break-up rifting is accompanied by modest amounts of melts within depleted asthenospheric upper mantle whereas a relatively fast (tens of Myr) transition to break-up promotes decompressional melting of enriched plume material.
5. Our findings have important implications for the styles of rifting induced by small thermal anomalies, leading to the recognition of two novel intermediate modes of rifting and break-up: 'semi-active' and 'semi-passive', complementing classical 'passive' versus 'active' concepts. Several segments of the passive margins formed during Pangea fragmentation have been developed under these intermediate regimes, which could, therefore, be potentially quite common in geological history.

ACKNOWLEDGEMENTS

This study is cofunded by an Alexander von Humboldt Foundation fellowship (A. Koptev), ERC Consolidator grant 615703 EXTREME (T. A. Ehlers, A. Koptev), the Distinguished Guest Scientist Fellowship Program of the Hungarian Academy of Sciences (S. Cloetingh), an Alexander von Humboldt Research Award (S. Cloetingh), and a German Science Foundation grant DFG-EH329/19–1 (T. A. Ehlers). The numerical simulations were performed on the University of Tübingen cluster. We thank Taras Gerya for providing the numerical code I3ELVIS. Discussions with Istvan Kovács and Christoph Glotzbach are appreciated. We thank Antonio Cordoba and Marzieh Baes for very insightful and constructive reviews.

Author contributions: A. Koptev and S. Cloetingh elaborated the conceptual idea and model. A. Koptev and T. A. Ehlers developed methods and modelling strategy. A. Koptev designed and conducted experiments and took the lead in writing the manuscript. All authors discussed the results and implications and commented on the manuscript at all stages.

DATA AVAILABILITY

The figures in the supporting information contain the numerical simulation data. The computer code I3ELVIS used to generate our thermomechanical numerical models is provided in Gerya (2010).

REFERENCES

Amaru, M.L., 2007. Global travel time tomography with 3-D reference models, *PhD thesis*, Utrecht University, 174pp.

Anderson, D.L., 2000. The thermal state of the upper mantle; no role for mantle plumes, *Geophys. Res. Lett.,* **27**(22), 3623–3626.

Artemieva, I.M., 2006. Global 1×1 thermal model TC1 for the continental lithosphere: implications for lithosphere secular evolution, *Tectonophysics,* **416**(1–4), 245–277.

Artemieva, I.M. & Mooney, W.D., 2001. Thermal thickness and evolution of Precambrian lithosphere: a global study, *J. geophys. Res.,* **106**(B8), 16387–16414.

Azevedo, R.P.D., 1991. Tectonic evolution of Brazilian equatorial continental margin basins, *PhD thesis*. London Royal School of Mines, Imperial College, 455pp.

Babuška, V., Plomerová, J. & Vecsey, L., 2008. Mantle fabric of western Bohemian Massif (central Europe) constrained by 3D seismic P and S anisotropy, *Tectonophysics,* **462**(1–4), 149–163.

Baes, M., Gerya, T. & Sobolev, S.V., 2016. 3-D thermo-mechanical modeling of plume-induced subduction initiation, *Earth planet. Sci. Lett.,* **453,** 193–203.

Baes, M., Sobolev, S., Gerya, T. & Brune, S., 2020a. Plume-induced subduction initiation: single-slab or multi-slab subduction?, *Geochem. Geophys. Geosyst.,* **21**(2), e2019GC008663, doi:10.1029/2019GC008663.

Baes, M., Sobolev, S.V., Gerya, T. & Brune, S., 2020b. Subduction initiation by plume-plateau interaction: insights from numerical models, *Geochem. Geophys. Geosyst.,* **21**(8), e2020GC009119, doi:10.1029/2020GC009119.

Baes, M., Sobolev, S., Gerya, T., Stern, R. & Brune, S., 2021. Plate motion and plume-induced subduction initiation. *Gondwana Research,* doi:10.1016/j.gr.2021.06.007.

Bahadori, A. & Holt, W.E., 2019. Geodynamic evolution of southwestern North America since the Late Eocene, *Nat. Commun.,* **10**(1), 1–18.

Ball, P., Eagles, G., Ebinger, C., McClay, K. & Totterdell, J., 2013. The spatial and temporal evolution of strain during the separation of Australia and Antarctica, *Geochem. Geophys. Geosyst.,* **14**(8), 2771–2799.

Basile, C., Mascle, J. & Guiraud, R., 2005. Phanerozoic geological evolution of the Equatorial Atlantic domain, *J. Afr. Earth Sci.,* **43**(1–3), 275–282.
Beniest, A., Koptev, A. & Burov, E., 2017a. Numerical models for continental break-up: implications for the South Atlantic, *Earth planet. Sci. Lett.,* **461,** 176–189.
Beniest, A., Koptev, A., Leroy, S., Sassi, W. & Guichet, X., 2017b. Two-branch break-up systems by a single mantle plume: insights from numerical modeling, *Geophys. Res. Lett.,* **44**(19), 9589–9597.
Berberich, G.M., Berberich, M.B., Ellison, A.M. & Wöhler, C., 2019. First identification of periodic degassing rhythms in three mineral springs of the East Eifel Volcanic Field (EEVF, Germany), *Geosciences,* **9**(4), 189.
Bercovici, D. & Long, M.D., 2014. Slab rollback instability and supercontinent dispersal, *Geophys. Res. Lett.,* **41**(19), 6659–6666.
Bijwaard, H. & Spakman, W., 1999. Tomographic evidence for a narrow whole mantle plume below Iceland, *Earth planet. Sci. Lett.,* **166**(3–4), 121–126.
Bird, P., Liu, Z. & Rucker, W.K., 2008. Stresses that drive the plates from below: definitions, computational path, model optimization, and error analysis, *J. geophys. Res.,* **113**(B11), B11406.
Boger, S.D., 2011. Antarctica – before and after Gondwana, *Gondwana Res.,* **19**(2), 335–371.
Bourgeois, O., Ford, M., Diraison, M., De Veslud, C.L.C., Gerbault, M., Pik, R., Rubi, N. & Bonnet, S., 2007. Separation of rifting and lithospheric folding signatures in the NW-Alpine foreland, *Int. J. Earth Sci.,* **96**(6), 1003–1031.
Bradley, D.C., 2011. Secular trends in the geologic record and the supercontinent cycle, *Earth Sci. Rev.,* **108**(1–2), 16–33.
Bredow, E. & Steinberger, B., 2018. Variable melt production rate of the Kerguelen hotspot due to long-term plume-ridge interaction, *Geophys. Res. Lett.,* **45**(1), 126–136.
Bredow, E., Steinberger, B., Gassmöller, R. & Dannberg, J., 2017. How plume-ridge interaction shapes the crustal thickness pattern of the Réunion hotspot track, *Geochem. Geophys. Geosyst.,* **18**(8), 2930–2948.
Bronner, A., Sauter, D., Manatschal, G., Péron-Pinvidic, G. & Munschy, M., 2011. Magmatic breakup as an explanation for magnetic anomalies at magma-poor rifted margins, *Nat. Geosci.,* **4**(8), 549–553.
Brune, S., 2014. Evolution of stress and fault patterns in oblique rift systems: 3-D numerical lithospheric-scale experiments from rift to breakup, *Geochem. Geophys. Geosyst.,* **15**(8), 3392–3415.
Brune, S. & Autin, J., 2013. The rift to break-up evolution of the Gulf of Aden: insights from 3D numerical lithospheric-scale modelling, *Tectonophysics,* **607,** 65–79.
Brune, S., Heine, C., Clift, P.D. & Pérez-Gussinyé, M., 2017. Rifted margin architecture and crustal rheology: reviewing Iberia-Newfoundland, central South Atlantic, and South China Sea, *Mar. Pet. Geol.,* **79,** 257–281.
Brune, S., Popov, A.A. & Sobolev, S.V., 2013. Quantifying the thermo-mechanical impact of plume arrival on continental break-up, *Tectonophysics,* **604,** 51–59.
Brune, S., Popov, A.A. & Sobolev, S.V., 2012. Modeling suggests that oblique extension facilitates rifting and continental break-up, *J. geophys. Res.,* **117**(B8), B08402, doi:10.1029/2011JB008860.
Bryan, S.E. & Ernst, R.E., 2008. Revised definition of Large Igneous Provinces (LIPs), *Earth Sci. Rev.,* **86**(1–4), 175–202.
Buikin, A., Trieloff, M., Hopp, J., Althaus, T., Korochantseva, E., Schwarz, W.H. & Altherr, R., 2005. Noble gas isotopes suggest deep mantle plume source of late Cenozoic mafic alkaline volcanism in Europe, *Earth planet. Sci. Lett.,* **230**(1–2), 143–162.
Buiter, S.J. & Torsvik, T.H., 2014. A review of Wilson Cycle plate margins: a role for mantle plumes in continental break-up along sutures?, *Gondwana Res.,* **26**(2), 627–653.
Burbidge, D.R., 2004. Thin plate neotectonic models of the Australian Plate, *J. geophys. Res.,* **109**(B10), B10405.
Burke, K., 2011. Plate tectonics, the Wilson Cycle, and mantle plumes: geodynamics from the top, *Annu. Rev. Earth planet. Sci.,* **39,** 1–29.
Burke, K. & Torsvik, T.H., 2004. Derivation of large igneous provinces of the past 200 million years from long-term heterogeneities in the deep mantle, *Earth planet. Sci. Lett.,* **227**(3–4), 531–538.
Burov, E.B., 2011. Rheology and strength of the lithosphere, *Mar. Pet. Geol.,* **28**(8), 1402–1443.
Burov, E. & Cloetingh, S., 2009. Controls of mantle plumes and lithospheric folding on modes of intraplate continental tectonics: differences and similarities, *Geophys. J. Int.,* **178**(3), 1691–1722.
Burov, E. & Cloetingh, S., 2010. Plume-like upper mantle instabilities drive subduction initiation, *Geophys. Res. Lett.,* **37**(3), L03309.
Burov, E. & Gerya, T., 2014. Asymmetric three-dimensional topography over mantle plumes, *Nature,* **513**(7516), 85–89.
Burov, E. & Guillou-Frottier, L., 2005. The plume head-continental lithosphere interaction using a tectonically realistic formulation for the lithosphere, *Geophys. J. Int.,* **161**(2), 469–490.
Callot, J.P., Geoffroy, L. & Brun, J.P., 2002. Development of volcanic passive margins: three-dimensional laboratory models, *Tectonics,* **21**(6), 1052.
Cammarano, F., Goes, S., Vacher, P. & Giardini, D., 2003. Inferring upper-mantle temperatures from seismic velocities, *Phys. Earth planet. Inter.,* **138**(3–4), 197–222.
Campbell, I.H., 2007. Testing the plume theory, *Chem. Geol.,* **241**(3–4), 153–176.
Campbell, I.H. & Davies, G.F., 2006. Do mantle plumes exist?, *Episodes,* **29**(3), 162–168.
Campbell, I.H. & Griffiths, R.W., 1990. Implications of mantle plume structure for the evolution of flood basalts, *Earth planet. Sci. Lett.,* **99**(1–2), 79–93.
Caracausi, A., Avice, G., Burnard, P.G., Füri, E. & Marty, B., 2016. Chondritic xenon in the Earth's mantle, *Nature,* **533**(7601), 82–85.
Cebriá, J.M., Lopez-Ruiz, J., Doblas, M., Martins, L.T. & Munha, J., 2003. Geochemistry of the early Jurassic Messejana-Plasencia dyke (Portugal-Spain); implications on the origin of the Central Atlantic Magmatic Province, *J. Petrol.,* **44**(3), 547–568.
Chu, R., Leng, W., Helmberger, D.V. & Gurnis, M., 2013. Hidden hotspot track beneath the eastern United States, *Nat. Geosci.,* **6**(11), 963–966.
Cloetingh, S. *et al.*, 2021. Plume-induced sinking of intracontinental lithospheric mantle: an overlooked mechanism of subduction initiation?, *Geochem. Geophys. Geosyst.,* **22**(2), e2020GC009482, doi:10.1029/2020GC009482.
Cloetingh, S.A.P.L., Van Wees, J.D., Van der Beek, P.A. & Spadini, G., 1995. Role of pre-rift rheology in kinematics of extensional basin formation: constraints from thermomechanical models of Mediterranean and intracratonic basins, *Mar. Pet. Geol.,* **12**(8), 793–807.
Cloetingh, S. & Wortel, R., 1986. Stress in the Indo-Australian plate, *Tectonophysics,* **132**(1–3), 49–67.
Cloetingh, S.A.P.L. & Ziegler, P.A., 2009. TOPO-EUROPE: coupled deep earth-surface processes in Europe, *Eur. Rev.,* **17**(3), 517–540.
Coblentz, D.D., Richardson, R.M. & Sandiford, M., 1994. On the gravitational potential of the Earth's lithosphere, *Tectonics,* **13**(4), 929–945.
Coblentz, D.D. & Richardson, R.M., 1996. Analysis of the South American intraplate stress field, *J. geophys. Res.,* **101**(B4), 8643–8657.
Coblentz, D.D. & Sandiford, M., 1994. Tectonic stresses in the African plate: constraints on the ambient lithospheric stress state, *Geology,* **22**(9), 831–834.
Coffin, M.F. & Eldholm, O., 1994. Large igneous provinces: crustal structure, dimensions, and external consequences, *Rev. Geophys.,* **32**(1), 1–36.
Coffin, M.F., Pringle, M.S., Duncan, R.A., Gladczenko, T.P., Storey, M., Müller, R.D. & Gahagan, L.A., 2002. Kerguelen hotspot magma output since 130 Ma, *J. Petrol.,* **43**(7), 1121–1137.
Coffin, M.F. & Rabinowitz, P.D., 1988. Evolution of the conjugate East African-Madagascar margins and western Somali Basin, *Geol. Soc. Am. Spec. Papers,* **226,** 77.
Collins, W.J., 2003. Slab pull, mantle convection, and Pangaean assembly and dispersal, *Earth planet. Sci. Lett.,* **205**(3–4), 225–237.
Connolly, J.A., 2005. Computation of phase equilibria by linear programming: a tool for geodynamic modeling and its application to subduction zone decarbonation, *Earth planet. Sci. Lett.,* **236**(1–2), 524–541.
Conrad, C.P. & Lithgow-Bertelloni, C., 2002. How mantle slabs drive plate tectonics, *Science,* **298**(5591), 207–209.
Córdoba, A.M.-C. & Ballmer, M.D., 2019. The origin of Western Atlantic volcanic archipelagos by interaction of edge-driven convection and mantle

plumes, in *Proceedings of the 21st EGU General Assembly, EGU2019,* held 7–12 April, 2019, Vienna, Austria, id.15332.
Córdoba, A.M.-C. & Ballmer, M.D., 2021. The role of edge-driven convection in the generation of volcanism – Part 1: a 2D systematic study, *Solid Earth,* **12**(3), 613–632.
Courtillot, V., Davaille, A., Besse, J. & Stock, J., 2003. Three distinct types of hotspots in the Earth's mantle, *Earth planet. Sci. Lett.,* **205**(3–4), 295–308.
Courtillot, V., Jaupart, C., Manighetti, I., Tapponnier, P. & Besse, J., 1999. On causal links between flood basalts and continental breakup, *Earth planet. Sci. Lett.,* **166**(3–4), 177–195.
Cox, R.T. & Van Arsdale, R.B., 2002. The Mississippi Embayment, North America: a first order continental structure generated by the Cretaceous superplume mantle event, *J. Geodyn.,* **34**(2), 163–176.
Crameri, F. *et al.*, 2012. A comparison of numerical surface topography calculations in geodynamic modelling: an evaluation of the "sticky air" method, *Geophys. J. Int.,* **189**(1), 38–54.
d'Acremont, E., Leroy, S. & Burov, E.B., 2003. Numerical modelling of a mantle plume: the plume head-lithosphere interaction in the formation of an oceanic large igneous province, *Earth planet. Sci. Lett.,* **206**(3–4), 379–396.
Cucciniello, C., Langone, A., Melluso, L., Morra, V., Mahoney, J.J., Meisel, T. & Tiepolo, M., 2010. U-Pb Ages, Pb-Os isotope ratios, and Platinum-Group Element (PGE) composition of the west-central Madagascar flood basalt province, *J. Geol.,* **118**(5), 523–541.
Cucciniello, C., Morra, V., Melluso, L. & Jourdan, F., 2021. *Constraints on duration, age and migration of the feeder systems of the Madagascan flood basalt province from high-precision 40Ar/39Ar chronology,* Geol. Soc.: London. Spec. Publ., 518, doi:10.1144/SP518-2020-275.
Dal Zilio, L., Faccenda, M. & Capitanio, F., 2018. The role of deep subduction in supercontinent breakup, *Tectonophysics,* **746,** 312–324.
Dang, Z., Zhang, N., Li, Z.-X., Huang, C., Spencer, C.J. & Liu, Y., 2020. Where a supercontinent breaks up: triggered by mantle plumes but guided by old scars, *Commun. Earth Environ.,* **1**(1), 51, 1–11.
Davaille, A. & Romanowicz, B., 2020. Deflating the LLSVPs: bundles of mantle thermochemical plumes rather than thick stagnant "piles", *Tectonics,* **39**(10), e2020TC006265.
Davis, J.K., Bécel, A. & Buck, W.R., 2018. Estimating emplacement rates for seaward-dipping reflectors associated with the US East Coast Magnetic Anomaly, *Geophys. J. Int.,* **215**(3), 1594–1603.
Dobretsov, N.L., Kirdyashkin, A.A., Kirdyashkin, A.G., Vernikovsky, V.A. & Gladkov, I.N., 2008. Modelling of thermochemical plumes and implications for the origin of the Siberian traps, *Lithos,* **100**(1–4), 66–92.
Dordevic, M. & Georgen, J., 2016. Dynamics of plume-triple junction interaction: results from a series of three-dimensional numerical models and implications for the formation of oceanic plateaus, *J. geophys. Res.,* **121**(3), 1316–1342.
Doubrovine, P.V., Steinberger, B. & Torsvik, T.H., 2012. Absolute plate motions in a reference frame defined by moving hot spots in the Pacific, Atlantic, and Indian oceans, *J. geophys. Res.,* **117**(B9), B09101, doi:10.1029/2011JB009072.
Doubrovine, P.V., Steinberger, B. & Torsvik, T.H., 2016. A failure to reject: Testing the correlation between large igneous provinces and deep mantle structures with EDF statistics, *Geochem. Geophys. Geosyst.,* **17**(3), 1130–1163.
Dubinin, E.P., Grokholsky, A.L. & Makushkina, A.I., 2018. Physical modeling of the formation conditions of microcontinents and continental marginal plateaus, *Izvestiya, Phys. Solid Earth,* **54**(1), 66–78.
Duncan, R.A., Hooper, P.R., Rehacek, J., Marsh, J. & Duncan, A.R., 1997. The timing and duration of the Karoo igneous event, southern Gondwana, *J. geophys. Res.,* **102**(B8), 18 127–18 138.
Dupré, S., Bertotti, G. & Cloetingh, S., 2007. Tectonic history along the South Gabon Basin: anomalous early post-rift subsidence, *Mar. Pet. Geol.,* **24**(3), 151–172.
Dupré, S., Cloetingh, S. & Bertotti, G., 2011. Structure of the Gabon Margin from integrated seismic reflection and gravity data, *Tectonophysics,* **506**(1–4), 31–45.
Duretz, T., May, D.A., Gerya, T.V. & Tackley, P.J., 2011. Discretization errors and free surface stabilization in the finite difference and marker-in-cell method for applied geodynamics: a numerical study, *Geochem. Geophys. Geosyst.,* **12**(7), Q07004, doi:10.1029/2011GC003567.
Dziewonski, A.M., Lekic, V. & Romanowicz, B.A., 2010. Mantle anchor structure: an argument for bottom up tectonics, *Earth planet. Sci. Lett.,* **299**(1–2), 69–79.
Ebinger, C.J. & Sleep, N.H., 1998. Cenozoic magmatism throughout east Africa resulting from impact of a single plume, *Nature,* **395**(6704), 788–791.
Ellam, R.M., Carlson, R.W. & Shirey, S.B., 1992. Evidence from Re-Os isotopes for plume-lithosphere mixing in Karoo flood basalt genesis, *Nature,* **359**(6397), 718–721.
Ernst, R.E., 2014. *Large Igneous Provinces*. Cambridge Univ. Press, 666pp.
Ershov, A.V. & Stephenson, R.A., 2006. Implications of a visco-elastic model of the lithosphere for calculating yield strength envelopes, *J. Geodyn.,* **42**(1–3), 12–27.
Faccenna, C., Becker, T.W., Jolivet, L. & Keskin, M., 2013. Mantle convection in the Middle East: reconciling Afar upwelling, Arabia indentation and Aegean trench rollback, *Earth planet. Sci. Lett.,* **375,** 254–269.
Farnetani, C.G. & Richards, M.A., 1994. Numerical investigations of the mantle plume initiation model for flood basalt events, *J. geophys. Res.,* **99**(B7), 13 813–13 833.
Fauquette, S. *et al.*, 2020. Pliocene uplift of the Massif Central (France) constrained by the palaeoelevation quantified from the pollen record of sediments preserved along the Cantal Stratovolcano (Murat area), *J. Geol. Soc.,* **177,** 923–938.
Fei, H., Yamazaki, D., Sakurai, M., Miyajima, N., Ohfuji, H., Katsura, T. & Yamamoto, T., 2017. A nearly water-saturated mantle transition zone inferred from mineral viscosity, *Sci. Adv.,* **3**(6), e1603024, doi:10.1126/sciadv.1603024Article.
Finn, C.A., Goodge, J.W., Damaske, D. & Fanning, C.M., 2006. Scouting craton's edge in paleo-Pacific Gondwana, in *Antarctica,* pp. 165–173, eds Fütterer, D.K., Damaske, D., Kleinschmidt, G., Miller, H. & Tessensohn, F., Springer.
Fitton, J.G., 1983. Active versus passive continental rifting: evidence from the West African rift system, *Tectonophysics,* **94**(1–4), 473–481.
Flesch, L.M., Haines, A.J. & Holt, W.E., 2001. Dynamics of the India-Eurasia collision zone, *J. geophys. Res.,* **106**(B8), 16 435–16 460.
Fomin, I. & Schiffer, C., 2019. Water, hydrous melting, and teleseismic signature of the mantle transition zone, *Geosciences,* **9**(12), 505.
Forsyth, D. & Uyeda, S., 1975. On the relative importance of the driving forces of plate motion, *Geophys. J. Int.,* **43**(1), 163–200.
Foulger, G.R. & Anderson, D.L., 2005. A cool model for the Iceland hotspot, *J. Volc. Geotherm. Res.,* **141**(1–2), 1–22.
Foulger, G.R. & Hamilton, W.B., 2014. Plume hypothesis challenged, *Nature,* **505**(7485), 618–618.
Foulger, G.R. *et al.*, 2000. The seismic anomaly beneath Iceland extends down to the mantle transition zone and no deeper, *Geophys. J. Int.,* **142**(3), F1–F5.
François, T., Koptev, A., Cloetingh, S., Burov, E. & Gerya, T., 2018. Plume-lithosphere interactions in rifted margin tectonic settings: inferences from thermo-mechanical modelling, *Tectonophysics,* **746,** 138–154.
Franke, D., 2013. Rifting, lithosphere breakup and volcanism: comparison of magma-poor and volcanic rifted margins, *Mar. Pet. Geol.,* **43,** 63–87.
Franke, D., Neben, S., Schreckenberger, B., Schulze, A., Stiller, M. & Krawczyk, C.M., 2006. Crustal structure across the Colorado Basin, offshore Argentina, *Geophys. J. Int.,* **165**(3), 850–864.
Franke, D., Neben, S., Ladage, S., Schreckenberger, B. & Hinz, K., 2007. Margin segmentation and volcano-tectonic architecture along the volcanic margin off Argentina/Uruguay, South Atlantic, *Mar. Geol.,* **244**(1–4), 46–67.
French, S.W. & Romanowicz, B., 2015. Broad plumes rooted at the base of the Earth's mantle beneath major hotspots, *Nature,* **525**(7567), 95–99.
Friedrich, A.M., Bunge, H.P., Rieger, S.M., Colli, L., Ghelichkhan, S. & Nerlich, R., 2018. Stratigraphic framework for the plume mode of mantle convection and the analysis of interregional unconformities on geological maps, *Gondwana Res.,* **53,** 159–188.

Funck, T., Erlendsson, Ö., Geissler, W.H., Gradmann, S., Kimbell, G.S., McDermott, K. & Petersen, U.K., 2017. A review of the NE Atlantic conjugate margins based on seismic refraction data, *Geol. Soc., Lond., Spec. Publ.,* **447**(1), 171–205.

Gac, S. & Geoffroy, L., 2009. 3D Thermo-mechanical modelling of a stretched continental lithosphere containing localized low-viscosity anomalies (the soft-point theory of plate break-up), *Tectonophysics,* **468**(1–4), 158–168.

Garcia-Castellanos, D., Cloetingh, S. & Van Balen, R., 2000. Modelling the Middle Pleistocene uplift in the Ardennes-Rhenish Massif: thermo-mechanical weakening under the Eifel?, *Global Planet. Change,* **27**(1–4), 39–52.

Gassmöller, R., Dannberg, J., Bredow, E., Steinberger, B. & Torsvik, T.H., 2016. Major influence of plume-ridge interaction, lithosphere thickness variations, and global mantle flow on hotspot volcanism – The example of Tristan, *Geochem. Geophys. Geosyst.,* **17**(4), 1454–1479.

Geldmacher, J., Hoernle, K., Bogaard, P., Duggen, S. & Werner, R., 2005. New 40Ar/39Ar age and geochemical data from seamounts in the Canary and Madeira volcanic provinces: support for the mantle plume hypothesis, *Earth planet. Sci. Lett.,* **237**(1–2), 85–101.

Geoffroy, L., 2001. The structure of volcanic margins: some problematics from the North-Atlantic/Labrador-Baffin system, *Mar. Pet. Geol.,* **18**(4), 463–469.

Geoffroy, L., 2005. Volcanic passive margins, *C.R. Geosci.,* **337**(16), 1395–1408.

Georgen, J.E., 2011. Lithospheric control on the spatial pattern of Azores hotspot seafloor anomalies: constraints from a model of plume-triple junction interaction, *Geophys. Res. Lett.,* **38**(19), L19305.

Georgen, J.E., Lin, J. & Dick, H.J., 2001. Evidence from gravity anomalies for interactions of the Marion and Bouvet hotspots with the Southwest Indian Ridge: effects of transform offsets, *Earth planet. Sci. Lett.,* **187**(3–4), 283–300.

Gerya, T.V., 2013a. Initiation of transform faults at rifted continental margins: 3D petrological-thermomechanical modeling and comparison to the Woodlark Basin, *Petrology,* **21**(6), 550–560.

Gerya, T.V., 2010. *Introduction to Numerical Geodynamic Modelling*. Cambridge Univ. Press, 358pp.

Gerya, T.V., 2013b. Three-dimensional thermomechanical modeling of oceanic spreading initiation and evolution, *Phys. Earth planet. Inter.,* **214,** 35–52.

Gerya, T. & Burov, E., 2018. Nucleation and evolution of ridge-ridge-ridge triple junctions: thermomechanical model and geometrical theory, *Tectonophysics,* **746,** 83–105.

Gerya, T.V. & Meilick, F.I., 2011. Geodynamic regimes of subduction under an active margin: effects of rheological weakening by fluids and melts, *J. Metamorph. Geol.,* **29**(1), 7–31.

Gerya, T.V., Stern, R.J., Baes, M., Sobolev, S.V. & Whattam, S.A., 2015. Plate tectonics on the Earth triggered by plume-induced subduction initiation, *Nature,* **527**(7577), 221–225.

Gerya, T.V. & Yuen, D.A., 2007. Robust characteristics method for modelling multiphase visco-elasto-plastic thermo-mechanical problems, *Phys. Earth planet. Inter.,* **163**(1–4), 83–105.

Gibson, S.A. & Richards, M.A., 2018. Delivery of deep-sourced, volatile-rich plume material to the global ridge system, *Earth planet. Sci. Lett.,* **499,** 205–218.

Goes, S., Govers, R. & Vacher, P., 2000. Shallow mantle temperatures under Europe from P and S wave tomography, *J. geophys. Res.,* **105**(B5), 11 153–11 169.

Goes, S., Spakman, W. & Bijwaard, H., 1999. A lower mantle source for central European volcanism, *Science,* **286**(5446), 1928–1931.

Göğüş, O.H., 2020. Geodynamic experiments suggest that mantle plume caused Late Permian Emeishan Large Igneous Province in Southern China, *Int. Geol. Rev.,* doi:10.1080/00206814.2020.1855602.

Granet, M., Wilson, M. & Achauer, U., 1995. Imaging a mantle plume beneath the French Massif Central, *Earth planet. Sci. Lett.,* **136**(3–4), 281–296.

Griffiths, R.W. & Campbell, I.H., 1990. Stirring and structure in mantle starting plumes, *Earth planet. Sci. Lett.,* **99**(1–2), 66–78.

Griffiths, R.W., Gurnis, M. & Eitelberg, G., 1989. Holographic measurements of surface topography in laboratory models of mantle hotspots, *Geophys. J. Int.,* **96**(3), 477–495.

Guillou-Frottier, L., Burov, E., Nehlig, P. & Wyns, R., 2007. Deciphering plume-lithosphere interactions beneath Europe from topographic signatures, *Global Planet. Change,* **58**(1–4), 119–140.

Guan, H., Geoffroy, L. & Xu, M., 2021. Magma-assisted fragmentation of Pangea: continental breakup initiation and propagation, *Gondwana Res.,* **96,** 56–75.

Harper, J.F., 1975. On the driving forces of plate tectonics, *Geophys. J. Int.,* **40**(3), 465–474.

Hart, S.R. & Zindler, A., 1986. In search of a bulk-Earth composition, *Chem. Geol.,* **57**(3–4), 247–267.

Hassan, R., Williams, S.E., Gurnis, M. & Müller, D., 2020. East African topography and volcanism explained by a single, migrating plume, *Geosci. Front.,* **5,** 1669–1680.

Heine, C. & Brune, S., 2014. Oblique rifting of the Equatorial Atlantic: why there is no Saharan Atlantic Ocean, *Geology,* **42**(3), 211–214.

Helffrich, G.R. & Wood, B.J., 2001. The Earth's mantle, *Nature,* **412**(6846), 501–507.

Heron, P.J., Lowman, J.P. & Stein, C., 2015. Influences on the positioning of mantle plumes following supercontinent formation, *J. geophys. Res.,* **120**(5), 3628–3648.

Herzberg, C. & Gazel, E., 2009. Petrological evidence for secular cooling in mantle plumes, *Nature,* **458**(7238), 619–622.

Hetényi, G., Stuart, G.W., Houseman, G.A., Horváth, F., Hegedűs, E. & Brückl, E., 2009. Anomalously deep mantle transition zone below Central Europe: evidence of lithospheric instability, *Geophys. Res. Lett.,* **36**(21), L21307, doi:10.1029/2009GL040171.

Hill, R.I., 1991. Starting plumes and continental break-up, *Earth planet. Sci. Lett.,* **104**(2–4), 398–416.

Hinzen, K., Reamer, S.K., Stein, S. & Mazzotti, S., 2007. Seismicity, seismotectonics, and seismic hazard in the northern Rhine area, *Geol. Soc. Am. Spec. Papers,* **425,** 225–242.

Hoernle, K.A.J., Zhang, Y.S. & Graham, D., 1995. Seismic and geochemical evidence for large-scale mantle upwelling beneath the eastern Atlantic and western and central Europe, *Nature,* **374**(6517), 34–39.

Holland, T.J.B. & Powell, R.T.J.B., 1998. An internally consistent thermodynamic data set for phases of petrological interest, *J. Metamorph. Geol.,* **16**(3), 309–343.

Holmes, A., 1965. *Principles of Physical Geology*. Ronald Press, 1288pp.

Holt, A.F., Becker, T.W. & Buffett, B.A., 2015. Trench migration and overriding plate stress in dynamic subduction models, *Geophys. J. Int.,* **201**(1), 172–192.

Huang, C., Zhang, N., Li, Z.X., Ding, M., Dang, Z., Pourteau, A. & Zhong, S., 2019. Modeling the inception of supercontinent breakup: stress state and the importance of orogens, *Geochem. Geophys. Geosyst.,* **20**(11), 4830–4848.

Huismans, R.S. & Beaumont, C., 2002. Asymmetric lithospheric extension: the role of frictional plastic strain softening inferred from numerical experiments, *Geology,* **30**(3), 211–214.

Huismans, R.S., Podladchikov, Y.Y. & Cloetingh, S., 2001. Transition from passive to active rifting: relative importance of asthenospheric doming and passive extension of the lithosphere, *J. geophys. Res.,* **106**(B6), 11 271–11 291.

Jackson, M.G., Carlson, R.W., Kurz, M.D., Kempton, P.D., Francis, D. & Blusztajn, J., 2010. Evidence for the survival of the oldest terrestrial mantle reservoir, *Nature,* **466**(7308), 853–856.

Jackson, M.G., Konter, J.G. & Becker, T.W., 2017. Primordial helium entrained by the hottest mantle plumes, *Nature,* **542**(7641), 340–343.

Janney, P.E. & Castillo, P.R., 2001. Geochemistry of the oldest Atlantic oceanic crust suggests mantle plume involvement in the early history of the central Atlantic Ocean, *Earth planet. Sci. Lett.,* **192**(3), 291–302.

Japsen, P. & Chalmers, J.A., 2000. Neogene uplift and tectonics around the North Atlantic: overview, *Global Planet. Change,* **24**(3–4), 165–173.

Jolivet, L., Menant, A., Clerc, C., Sternai, P., Bellahsen, N., Leroy, S., Pik, R., Stab, M., Faccenna, C. & Gorini, C., 2018. Extensional crustal tectonics

and crust-mantle coupling, a view from the geological record, *Earth Sci. Rev.,* **185,** 1187–1209.
Jordan, B.T., Grunder, A.L., Duncan, R.A. & Deino, A.L., 2004. Geochronology of age-progressive volcanism of the Oregon High Lava Plains: implications for the plume interpretation of Yellowstone, *J. geophys. Res.,* **109**(B10), B10202, doi:10.1029/2003JB002776.
Karato, S., 2008. *Deformation of Earth Materials*. Cambridge Univ. Press, 482pp.
Karato, S.I., 1986. Does partial melting reduce the creep strength of the upper mantle?, *Nature,* **319**(6051), 309–310.
Karato, S.I. & Wu, P., 1993. Rheology of the upper mantle: a synthesis, *Science,* **260**, 771–778.
Katsura, T., Yoneda, A., Yamazaki, D., Yoshino, T. & Ito, E., 2010. Adiabatic temperature profile in the mantle, *Phys. Earth planet. Inter.,* **183**(1–2), 212–218.
Katz, R.F., Spiegelman, M. & Langmuir, C.H., 2003. A new parameterization of hydrous mantle melting, *Geochem. Geophys. Geosyst.,* **4**(9), 1073.
Klitgord, K.D. & Schouten, H., 1986. Plate kinematics of the central Atlantic, in *The Western North Atlantic Region, Geology of North America,* pp. 351–378, eds Vogt, P.R. & Tucholke, B. E., Geological Society of America.
Koppers, A.A.P., *et al.*. 2021. Mantle plumes and their role in Earth processes, *Nat. Rev. Earth Environ.,* **2**(6), 382–401.
Koptev, A., Beniest, A., Gerya, T., Ehlers, T.A., Jolivet, L. & Leroy, S., 2019. Plume-induced breakup of a subducting plate: microcontinent formation without cessation of the subduction process, *Geophys. Res. Lett.,* **46**(7), 3663–3675.
Koptev, A., Burov, E., Calais, E., Leroy, S., Gerya, T., Guillou-Frottier, L. & Cloetingh, S., 2016. Contrasted continental rifting via plume-craton interaction: applications to Central East African Rift, *Geoscience Frontiers,* **7**(2), 221–236.
Koptev, A., Burov, E., Gerya, T., Le Pourhiet, L., Leroy, S., Calais, E. & Jolivet, L., 2018a. Plume-induced continental rifting and break-up in ultra-slow extension context: insights from 3D numerical modeling, *Tectonophysics,* **746,** 121–137.
Koptev, A., Calais, E., Burov, E., Leroy, S. & Gerya, T., 2018b. Along-axis variations of rift width in a coupled lithosphere-mantle system, application to East Africa, *Geophys. Res. Lett.,* **45**(11), 5362–5370.
Koptev, A., Calais, E., Burov, E., Leroy, S. & Gerya, T., 2015. Dual continental rift systems generated by plume-lithosphere interaction, *Nat. Geosci.,* **8**(5), 388–392.
Koptev, A., Cloetingh, S., Burov, E., François, T. & Gerya, T., 2017. Long-distance impact of Iceland plume on Norway's rifted margin, *Sci. Rep.,* **7,** 1–11.
Koptev, A., Cloetingh, S., Gerya, T., Calais, E. & Leroy, S., 2018c. Non-uniform splitting of a single mantle plume by double cratonic roots: insight into the origin of the central and southern East African Rift System, *Terra Nova,* **30**(2), 125–134.
Koptev, A., Cloetingh, S., Kovács, I.J., Gerya, T. & Ehlers, T.A., 2021. Controls by rheological structure of the lithosphere on the temporal evolution of continental magmatism: inferences from the Pannonian Basin system, *Earth planet. Sci. Lett.,* **565,** 116925.
Koptev, A.I. & Ershov, A.V., 2010. The role of the gravitational potential of the lithosphere in the formation of a global stress field, *Izvestiya, Phys. Solid Earth,* **46**(12), 1080–1094.
Koptev, A.I. & Ershov, A.V., 2011. Thermal thickness of the Earth's lithosphere: a numerical model, *Moscow Univ. Geol. Bull.,* **66**(5), 323–330.
Koptev, A., Gerya, T., Calais, E., Leroy, S. & Burov, E., 2018d. Afar triple junction triggered by plume-assisted bi-directional continental break-up, *Sci. Rep.,* **8,** 1–7.
Kovács, I. *et al.*, 2020. The role of water and compression in the genesis of alkaline basalts: inferences from the Carpathian-Pannonian region, *Lithos,* **354–355,** 105323.
Koulakov, I., Kaban, M.K., Tesauro, M. & Cloetingh, S.A.P.L., 2009. P-and S-velocity anomalies in the upper mantle beneath Europe from tomographic inversion of ISC data, *Geophys. J. Int.,* **179**(1), 345–366.
Kreemer, C., Blewitt, G. & Davis, P.M., 2020. Geodetic evidence for a buoyant mantle plume beneath the Eifel volcanic area, NW Europe, *Geophys. J. Int.,* **222**(2), 1316–1332.
Kuritani, T., Sakuyama, T., Kamada, N., Yokoyama, T. & Nakagawa, M., 2017. Fluid-fluxed melting of mantle versus decompression melting of hydrous mantle plume as the cause of intraplate magmatism over a stagnant slab: implications from Fukue Volcano Group, SW Japan, *Lithos,* **282,** 98–110.
Kuritani, T. *et al.*, 2019. Buoyant hydrous mantle plume from the mantle transition zone, *Sci. Rep.,* **9,** 1–7.
Labails, C., Olivet, J.L., Aslanian, D. & Roest, W.R., 2010. An alternative early opening scenario for the Central Atlantic Ocean, *Earth planet. Sci. Lett.,* **297**(3–4), 355–368.
Leleu, S., Hartley, A.J., van Oosterhout, C., Kennan, L., Ruckwied, K. & Gerdes, K., 2016. Structural, stratigraphic and sedimentological characterisation of a wide rift system: the Triassic rift system of the Central Atlantic Domain, *Earth Sci. Rev.,* **158,** 89–124.
Lenardic, A., 2017. Plate tectonics: a supercontinental boost, *Nat. Geosci.,* **10**(1), 4–5.
Li, S., Weng, A., Zhang, Y., Schultz, A., Li, Y., Tang, Y., Zou, Z. & Zhou, Z., 2020. Evidence of Bermuda hot and wet upwelling from novel three-dimensional global mantle electrical conductivity image, *Geochem. Geophys. Geosyst.,* **21**(6), e2020GC009016, doi:10.1029/2020GC009016.
Li, Z.X. *et al.*, 2008. Assembly, configuration, and break-up history of Rodinia: a synthesis, *Precambrian Res.,* **160**(1–2), 179–210.
Li, Z.X., Li, X.H., Kinny, P.D. & Wang, J., 1999. The breakup of Rodinia: did it start with a mantle plume beneath South China?, *Earth planet. Sci. Lett.,* **173**(3), 171–181.
Lithgow-Bertelloni, C. & Guynn, J.H., 2004. Origin of the lithospheric stress field, *J. geophys. Res.,* **109**(B1), B01408, doi:10.1029/2003JB002467.
Liu, Z. & Bird, P., 2002. Finite element modeling of neotectonics in New Zealand, *J. geophys. Res.,* **107**(B12), ETG–1.
Long, X., Ballmer, M.D., Córdoba, A.M.-C. & Li, C.F., 2019. Mantle melting and intraplate volcanism due to self-buoyant hydrous upwellings from the stagnant slab that are conveyed by small-scale convection, *Geochem. Geophys. Geosyst.,* **20**(11), 4972–4997.
Long, X., Geldmacher, J., Hoernle, K., Hauff, F., Wartho, J.A. & Garbe-Schönberg, D., 2020. Origin of isolated seamounts in the Canary Basin (East Atlantic): the role of plume material in the origin of seamounts not associated with hotspot tracks, *Terra Nova,* **32**(5), 390–398.
Lundin, E.R. & Doré, A.G., 2005. NE Atlantic break-up: a re-examination of the Iceland mantle plume model and the Atlantic-Arctic linkage, in *Geological Society, London, Petroleum Geology Conference Series,* Vol. **6,** pp. 739–754.
Lustrino, M. & Carminati, E., 2007. Phantom plumes in Europe and the circum-Mediterranean region, *Geol. Soc. Am. Spec. Papers* **430,** 723–745.
Marzoli, A., Callegaro, S., Dal Corso, J., Davies, J.H., Chiaradia, M., Youbi, N., Bertrand, H., Reisberg, L., Merle, R. & Jourdan, F., 2018. The Central Atlantic magmatic province (CAMP): a review, in *The Late Triassic World,* pp. 91–125, ed. Tanner, L., Springer.
Marzoli, A., Renne, P.R., Piccirillo, E.M., Ernesto, M., Bellieni, G. & De Min, A., 1999. Extensive 200-million-year-old continental flood basalts of the Central Atlantic Magmatic Province, *Science,* **284**(5414), 616–618.
Max, M.D., Ghidella, M., Kovacs, L., Paterlini, M. & Valladares, J.A., 1999. Geology of the Argentine continental shelf and margin from aeromagnetic survey, *Mar. Pet. Geol.,* **16**(1), 41–64.
McHone, J.G., 2003. Volatile emissions from Central Atlantic Magmatic Province basalts: mass assumptions and environmental consequences, *AGU, Geophys. Monogr.,* **136,** 241–254.
McKenzie, D., 1978. Some remarks on the development of sedimentary basins, *Earth planet. Sci. Lett.,* **40**(1), 25–32.
Meigs, A. *et al.*, 2009. Geological and geophysical perspectives on the magmatic and tectonic development, High Lava Plains and northwest Basin and Range, in *Volcanoes to Vineyards: Geologic Field Trips Through the Dynamic Landscape of the Pacific Northwest,* Vol. **15,** pp. 435–470, Geological Society of America Field Guide.
Mjelde, R., Faleide, J.I., Breivik, A.J. & Raum, T., 2009. Lower crustal composition and crustal lineaments on the Vøring Margin, NE Atlantic: a review, *Tectonophysics,* **472**(1–4), 183–193.

Mjelde, R., Kvarven, T., Faleide, J.I. & Thybo, H., 2016. Lower crustal high-velocity bodies along North Atlantic passive margins, and their link to Caledonian suture zone eclogites and Early Cenozoic magmatism, *Tectonophysics,* **670,** 16–29.

Montelli, R., Nolet, G., Dahlen, F.A. & Masters, G., 2006. A catalogue of deep mantle plumes: new results from finite-frequency tomography, *Geochem. Geophys. Geosyst.,* **7**(11), Q11007.

Morgan, W.J., 1971. Convection plumes in the lower mantle, *Nature,* **230**(5288), 42–43.

Morgan, W.J., 1972. Plate motions and deep mantle convection, *Geol. Soc. Am. Mem.,* **132,** 7–22.

Müller, R.D., Roest, W.R., Royer, J.Y., Gahagan, L.M. & Sclater, J.G., 1997. Digital isochrons of the world's ocean floor, *J. geophys. Res.,* **102**(B2), 3211–3214.

Müntener, O. & Hermann, J., 2001. The role of lower crust and continental upper mantle during formation of non-volcanic passive margins: evidence from the Alps, *Geol. Soc., Lond., Spec. Publ.,* **187**(1), 267–288.

Mutter, J.C., Talwani, M. & Stoffa, P.L., 1982. Origin of seaward-dipping reflectors in oceanic crust off the Norwegian margin by "subaerial seafloor spreading", *Geology,* **10**(7), 353–357.

Mutter, J.C. & Zehnder, C.M., 1988. Deep crustal structure and magmatic processes: the inception of seafloor spreading in the Norwegian-Greenland Sea, *Geol. Soc., Lond., Spec. Publ.,* **39**(1), 35–48.

Naliboff, J.B., Lithgow-Bertelloni, C., Ruff, L.J. & de Koker, N., 2012. The effects of lithospheric thickness and density structure on Earth′ s stress field, *Geophys. J. Int.,* **188**(1), 1–17.

Nemčok, M. *et al.*, 2013. East Indian margin evolution and crustal architecture: integration of deep reflection seismic interpretation and gravity modelling, *Geol. Soc., Lond., Spec. Publ.,* **369**(1), 477–496.

Neuharth, D., Brune, S., Glerum, A., Heine, C. & Welford, J.K., 2021. Formation of continental microplates through rift linkage: numerical modelling and its application to the Flemish Cap and Sao Paulo Plateau, *Geochem. Geophys. Geosyst.,* **22**(4), e2020GC009615, doi:10.1029/2020GC009615.

Niu, Y., 2018. Origin of the LLSVPs at the base of the mantle is a consequence of plate tectonics – a petrological and geochemical perspective, *Geosci. Front.,* **9**(5), 1265–1278.

Olsen, P.E., 1997. Stratigraphic record of the early Mesozoic breakup of Pangea in the Laurasia-Gondwana rift system, *Annu. Rev. Earth planet. Sci.,* **25**(1), 337–401.

Peace, A., McCaffrey, K., Imber, J., Hobbs, R., van Hunen, J. & Gerdes, K., 2017. Quantifying the influence of sill intrusion on the thermal evolution of organic-rich sedimentary rocks in nonvolcanic passive margins: an example from ODP 210–1276, offshore Newfoundland, Canada, *Basin Res.,* **29**(3), 249–265.

Peace, A.L. *et al.*, 2020. A review of Pangaea dispersal and Large Igneous Provinces – In search of a causative mechanism, *Earth Sci. Rev.,* **206,** 102902.

Pérez-Gussinyé, M., Morgan, J.P., Reston, T.J. & Ranero, C.R., 2006. The rift to drift transition at non-volcanic margins: insights from numerical modelling, *Earth planet. Sci. Lett.,* **244**(1–2), 458–473.

Plomerová, J., Achauer, U., Babuška, V. & Vecsey, L. BOHEMA Working Group, 2007. Upper mantle beneath the Eger Rift (Central Europe): plume or asthenosphere upwelling?, *Geophys. J. Int.,* **169**(2), 675–682.

Plomerová, J., Munzarová, H., Vecsey, L., Kissling, E., Achauer, U. & Babuška, V., 2016. Cenozoic volcanism in the Bohemian Massif in the context of P- and S-velocity high-resolution teleseismic tomography of the upper mantle, *Geochem. Geophys. Geosyst.,* **17**(8), 3326–3349.

Précigout, J., Gueydan, F., Gapais, D., Garrido, C.J. & Essaifi, A., 2007. Strain localisation in the subcontinental mantle – a ductile alternative to the brittle mantle, *Tectonophysics,* **445**(3–4), 318–336.

Rainbird, R.H. & Ernst, R.E., 2001. The sedimentary record of mantle-plume uplift, in *GSA Special Papers: Mantle Plumes: Their Identification Through Time,* Vol. **352,** pp. 227–246, eds Ernst R. E. & Buchan K. L., Geological Society of America.

Rajabi, M., Tingay, M., Heidbach, O., Hillis, R. & Reynolds, S., 2017. The present-day stress field of Australia, *Earth Sci. Rev.,* **168,** 165–189.

Ranalli, G., 1995. *Rheology of the Earth*. Chapman and Hall, 413pp.

Reemst, P. & Cloetingh, S., 2000. Polyphase rift evolution of the Vøring margin (mid-Norway): constraints from forward tectonostratigraphic modeling, *Tectonics,* **19**(2), 225–240.

Reynolds, S.D., Coblentz, D.D. & Hillis, R.R., 2002. Tectonic forces controlling the regional intraplate stress field in continental Australia: results from new finite element modeling, *J. geophys. Res.,* **107**(B7), ETG–1.

Richards, M.A., Duncan, R.A. & Courtillot, V.E., 1989. Flood basalts and hot-spot tracks: plume heads and tails, *Science,* **246**(4926), 103–107.

Richardson, R.M. & Reding, L.M., 1991. North American plate dynamics, *J. geophys. Res.,* **96**(B7), 12 201–12 223.

Richardson, R.M., Solomon, S.C. & Sleep, N.H., 1979. Tectonic stress in the plates, *Rev. Geophys.,* **17**(5), 981–1019.

Rickers, F., Fichtner, A. & Trampert, J., 2013. The Iceland-Jan Mayen plume system and its impact on mantle dynamics in the North Atlantic region: evidence from full-waveform inversion, *Earth planet. Sci. Lett.,* **367,** 39–51.

Riley, T.R., Leat, P.T., Curtis, M.L., Millar, I.L., Duncan, R.A. & Fazel, A., 2005. Early-Middle Jurassic dolerite dykes from Western Dronning Maud Land (Antarctica): identifying mantle sources in the Karoo large igneous province, *J. Petrol.,* **46**(7), 1489–1524.

Ritter, J.R.R., 2005. Small-scale mantle plumes: imaging and geodynamic aspects, in *Perspectives in Modern Seismology,* pp. 69–94, ed. Wenzel, F., Springer.

Ritter, J.R.R., 2007. The seismic signature of the Eifel plume, in *Mantle Plumes: A Multidisciplinary Approach,* pp. 379–404, eds Ritter, J.R.R. & Christensen, U.R., Springer.

Ritter, J.R., Achauer, U. & Christensen, U.R. Eifel Plume Team., 2000. The teleseismic tomography experiment in the Eifel region, Central Europe: design and first results, *Seismol. Res. Lett.,* **71**(4), 437–443.

Ritter, J.R., Jordan, M., Christensen, U.R. & Achauer, U., 2001. A mantle plume below the Eifel volcanic fields, Germany, *Earth planet. Sci. Lett.* **186**(1), 7–14.

Rohrman, M. & van der Beek, P., 1996. Cenozoic postrift domal uplift of North Atlantic margins: an asthenospheric diapirism model, *Geology,* **24**(10), 901–904.

Rohrman, M., van der Beek, P., Andriessen, P. & Cloetingh, S., 1995. Meso-Cenozoic morphotectonic evolution of southern Norway: neogene domal uplift inferred from apatite fission track thermochronology, *Tectonics,* **14**(3), 704–718.

Romanowicz, B. & Gung, Y., 2002. Superplumes from the core-mantle boundary to the lithosphere: implications for heat flux, *Science,* **296**(5567), 513–516.

Ryan, P.D. & Dewey, J.F., 1997. Continental eclogites and the Wilson Cycle, *J. Geol. Soc.,* **154**(3), 437–442.

Sahabi, M., Aslanian, D. & Olivet, J.L., 2004. Un nouveau point de départ pour l'histoire de l'Atlantique central, *C.R. Geosci.,* **336**(12), 1041–1052.

Saki, M., Thomas, C., Nippress, S.E. & Lessing, S., 2015. Topography of upper mantle seismic discontinuities beneath the North Atlantic: the Azores, Canary and Cape Verde plumes, *Earth planet. Sci. Lett.,* **409,** 193–202.

Saunders, A.D., Fitton, J.G., Kerr, A.C., Norry, M.J. & Kent, R.W., 1997. The North Atlantic Igneous Province, *AGU, Geophys. Monogr.,* **100,** 45–93.

Schellart, W.P. & Moresi, L., 2013. A new driving mechanism for backarc extension and backarc shortening through slab sinking induced toroidal and poloidal mantle flow: results from dynamic subduction models with an overriding plate, *J. geophys. Res.,* **118**(6), 3221–3248.

Schilling, J.G., 1991. Fluxes and excess temperatures of mantle plumes inferred from their interaction with migrating mid-ocean ridges, *Nature,* **352**(6334), 397–403.

Schlindwein, V. & Jokat, W., 1999. Structure and evolution of the continental crust of northern east Greenland from integrated geophysical studies, *J. geophys. Res.,* **104**(B7), 15 227–15 245.

Schnabel, M. *et al.*, 2008. The structure of the lower crust at the Argentine continental margin, South Atlantic at 44 S, *Tectonophysics,* **454**(1–4), 14–22.

Scrutton, R.A., 1973. The age relationship of igneous activity and continental break-up, *Geol. Mag.,* **110**(3), 227–234.

Şengör, A.C., 2001. Elevation as indicator of mantle-plume activity, *Geol. Soc. Am. Spec. Papers,* **352,** 183–225.

Şengör, A.C. & Burke, K., 1978. Relative timing of rifting and volcanism on Earth and its tectonic implications, *Geophys. Res. Lett.,* **5**(6), 419–421.

Seton, M. *et al.*, 2012. Global continental and ocean basin reconstructions since 200 Ma, *Earth Sci. Rev.,* **113**(3–4), 212–270.

Silveira, G., Stutzmann, E., Davaille, A., Montagner, J.P., Mendes-Victor, L. & Sebai, A., 2006. Azores hotspot signature in the upper mantle, *J. Volc. Geotherm. Res.,* **156**(1–2), 23–34.

Sinha, S.T., Nemčok, M., Choudhuri, M., Sinha, N. & Rao, D.P., 2016. The role of break-up localization in microcontinent separation along a strike-slip margin: the East India-Elan Bank case study, *Geol. Soc., Lond., Spec. Publ.,* **431**(1), 95–123.

Skogseid, J., 2001. Volcanic margins: geodynamic and exploration aspects, *Mar. Pet. Geol.,* **18**(4), 457–461.

Sleep, N.H., 2003. Geodynamic implications of xenolith geotherms, *Geochem. Geophys. Geosyst.,* **4**(9), 1079.

Sleep, N.H., 1997. Lateral flow and ponding of starting plume material, *J. geophys. Res.,* **102**(B5), 10 001–10 012.

Sleep, N.H., 1996. Lateral flow of hot plume material ponded at sublithospheric depths, *J. geophys. Res.,* **101**(B12), 28 065–28 083.

Smith, R.B. *et al.*, 2009. Geodynamics of the Yellowstone hotspot and mantle plume: seismic and GPS imaging, kinematics, and mantle flow, *J. Volc. Geotherm. Res.,* **188**(1–3), 26–56.

Sobolev, S.V., Sobolev, A.V., Kuzmin, D.V., Krivolutskaya, N.A., Petrunin, A.G., Arndt, N.T., Radko, V.A. & Vasiliev, Y.R., 2011. Linking mantle plumes, large igneous provinces and environmental catastrophes, *Nature,* **477**(7364), 312–316.

Sobolev, S.V., Zeyen, H., Granet, M., Achauer, U., Bauer, C., Werling, F., Altherr, R. & Fuchs, K., 1997. Upper mantle temperatures and lithosphere-asthenosphere system beneath the French Massif Central constrained by seismic, gravity, petrologic and thermal observations, *Tectonophysics,* **275**(1–3), 143–164.

Steinberger, B., Sutherland, R. & O'Connell, R.J., 2004. Prediction of Emperor-Hawaii seamount locations from a revised model of global plate motion and mantle flow, *Nature,* **430**(6996), 167–173.

Steinberger, B. & Torsvik, T.H., 2012. A geodynamic model of plumes from the margins of Large Low Shear Velocity Provinces, *Geochem. Geophys. Geosyst.,* **13**(1), Q01W09, doi:10.1029/2011GC003808.

Stern, T., Lamb, S., Moore, J.D., Okaya, D. & Hochmuth, K., 2020. High mantle seismic P-wave speeds as a signature for gravitational spreading of superplumes, *Sci. Adv.,* **6**(22), eaba7118, doi:10.1126/sciadv.aba7118.

Stixrude, L. & Lithgow-Bertelloni, C., 2005. Mineralogy and elasticity of the oceanic upper mantle: origin of the low-velocity zone, *J. geophys. Res.,* **110**(B3), B03204, doi:10.1029/2004JB002965.

Storey, M., Duncan, R.A. & Tegner, C., 2007. Timing and duration of volcanism in the North Atlantic Igneous Province: implications for geodynamics and links to the Iceland hotspot, *Chem. Geol.,* **241**(3–4), 264–281.

Swanson, M.T., 1986. Preexisting fault control for Mesozoic basin formation in eastern North America, *Geology,* **14**(5), 419–422.

Tang, Y. *et al.*, 2014. Changbaishan volcanism in northeast China linked to subduction-induced mantle upwelling, *Nat. Geosci.,* **7**(6), 470–475.

Tesauro, M., Kaban, M.K. & Cloetingh, S.A., 2009a. A new thermal and rheological model of the European lithosphere, *Tectonophysics,* **476**(3–4), 478–495.

Tesauro, M., Kaban, M.K. & Cloetingh, S.A., 2009b. How rigid is Europe's lithosphere?, *Geophys. Res. Lett.,* **36**(16), L16303.

Thompson, R.N. & Gibson, S.A., 2000. Transient high temperatures in mantle plume heads inferred from magnesian olivines in Phanerozoic picrites, *Nature,* **407**(6803), 502–506.

Torsvik, T.H., Burke, K., Steinberger, B., Webb, S.J. & Ashwal, L.D., 2010. Diamonds sampled by plumes from the core-mantle boundary, *Nature,* **466**(7304), 352–355.

Torsvik, T.H., Doubrovine, P.V., Steinberger, B., Gaina, C., Spakman, W. & Domeier, M., 2017. Pacific plate motion change caused the Hawaiian-Emperor Bend, *Nat. Commun.,* **8**(1), 1–12.

Torsvik, T.H., Smethurst, M.A., Burke, K. & Steinberger, B., 2006. Large igneous provinces generated from the margins of the large low-velocity provinces in the deep mantle, *Geophys. J. Int.,* **167**(3), 1447–1460.

Torsvik, T.H., Smethurst, M.A., Burke, K. & Steinberger, B., 2008. Long term stability in deep mantle structure: evidence from the ~300 Ma Skagerrak-Centered Large Igneous Province (the SCLIP), *Earth planet. Sci. Lett.,* **267**(3–4), 444–452.

Torsvik, T.H., Steinberger, B., Ashwal, L.D., Doubrovine, P.V. & Trønnes, R.G., 2016. Earth evolution and dynamics – a tribute to Kevin Burke, *Can. J. Earth Sci.,* **53**(11), 1073–1087.

Torsvik, T.H., Tucker, R.D., Ashwal, L.D., Carter, L.M., Jamtveit, B., Vidyadharan, K.T. & Venkataramana, P., 2000. Late Cretaceous India-Madagascar fit and timing of break-up related magmatism, *Terra Nova,* **12**(5), 220–224.

Torsvik, T.H., Tucker, R.D., Ashwal, L.D., Eide, E.A., Rakotosolofo, N.A. & De Wit, M.J., 1998. Late Cretaceous magmatism in Madagascar: palaeomagnetic evidence for a stationary Marion hotspot, *Earth planet. Sci. Lett.,* **164**(1–2), 221–232.

Torsvik, T.H. *et al.*, 2014. Deep mantle structure as a reference frame for movements in and on the Earth, *Proc. Natl. Acad. Sci.,* **111**(24), 8735–8740.

Tugend, J. *et al.*, 2020. Reappraisal of the magma-rich versus magma-poor rifted margin archetypes, *Geol. Soc., Lond., Spec. Publ.,* **476**(1), 23–47.

Tunini, L., Jiménez-Munt, I., Fernandez, M., Vergés, J. & Bird, P., 2017. Neotectonic deformation in central Eurasia: a geodynamic model approach, *J. geophys. Res.,* **122**(11), 9461–9484.

Turcotte, D.L. & Schubert, G., 2002. *Geodynamics*. Cambridge Univ. Press, 863pp.

Ueda, K., Gerya, T. & Sobolev, S.V., 2008. Subduction initiation by thermal-chemical plumes: numerical studies, *Phys. Earth planet. Inter.,* **171**(1–4), 296–312.

Ulrych, J., Dostal, J., Adamovič, J., Jelínek, E., Špaček, P., Hegner, E. & Balogh, K., 2011. Recurrent Cenozoic volcanic activity in the Bohemian Massif (Czech Republic), *Lithos,* **123**(1–4), 133–144.

Van Avendonk, H.J., Davis, J.K., Harding, J.L. & Lawver, L.A., 2017. Decrease in oceanic crustal thickness since the breakup of Pangaea, *Nat. Geosci.,* **10**(1), 58–61.

Veevers, J.J., 2012. Reconstructions before rifting and drifting reveal the geological connections between Antarctica and its conjugates in Gondwanaland, *Earth Sci. Rev.,* **111**(3–4), 249–318.

Vicente de Gouveia, S., Besse, J., de Lamotte, D.F., Greff-Lefftz, M., Lescanne, M., Gueydan, F. & Leparmentier, F., 2018. Evidence of hotspot paths below Arabia and the Horn of Africa and consequences on the Red Sea opening, *Earth planet. Sci. Lett.,* **487,** 210–220.

Wagner, L., Forsyth, D.W., Fouch, M.J. & James, D.E., 2010. Detailed three-dimensional shear wave velocity structure of the northwestern United States from Rayleigh wave tomography, *Earth planet. Sci. Lett.,* **299**(3–4), 273–284.

Westaway, R., 1993. Forces associated with mantle plumes, *Earth planet. Sci. Lett.,* **119**(3), 331–348.

White, R. & McKenzie, D., 1989. Magmatism at rift zones: the generation of volcanic continental margins and flood basalts, *J. geophys. Res.,* **94**(B6), 7685–7729.

White, R.S. & McKenzie, D., 1995. Mantle plumes and flood basalts, *J. geophys. Res.,* **100**(B9), 17 543–17 585.

White, R.S., Smith, L.K., Roberts, A.W., Christie, P.A.F. & Kusznir, N.J., 2008. Lower-crustal intrusion on the North Atlantic continental margin, *Nature,* **452**(7186), 460–464.

Williams, S.E., Whittaker, J.M., Granot, R. & Müller, D.R., 2013. Early India-Australia spreading history revealed by newly detected Mesozoic magnetic anomalies in the Perth Abyssal Plain, *J. geophys. Res.,* **118**(7), 3275–3284.

Wilson, J.T., 1963. A possible origin of the Hawaiian Islands, *Can. J. Phys.,* **41**(6), 863–870.

Wilson, J.T., 1966. Did the Atlantic close and then re-open?, *Nature,* **211**(5050), 676–681.

Wilson, M. & Downes, H., 1992. Mafic alkaline magmatism associated with the European Cenozoic rift system, *Tectonophysics,* **208**(1–3), 173–182.

Wilson, R.C.L., Manatschal, G. & Wise, S., 2001. Rifting along non-volcanic passive margins: stratigraphic and seismic evidence from the Mesozoic successions of the Alps and western Iberia, *Geol. Soc., Lond., Spec. Publ.,* **187**(1), 429–452.

Wortel, M.J.R. & Cloetingh, S.A.P.L., 1985. Accretion and lateral variations in tectonic structure along the Peru-Chile Trench, *Tectonophysics,* **112**(1–4), 443–462.

Xia, S., Zhao, D., Sun, J. & Huang, H., 2016. Teleseismic imaging of the mantle beneath southernmost China: new insights into the Hainan plume, *Gondwana Res.,* **36,** 46–56.

Yang, T. & Gurnis, M., 2016. Dynamic topography, gravity and the role of lateral viscosity variations from inversion of global mantle flow, *Geophys. J. Int.,* **207**(2), 1186–1202.

Yang, T. & Leng, W., 2014. Dynamics of hidden hotspot tracks beneath the continental lithosphere, *Earth planet. Sci. Lett.,* **401,** 294–300.

Yoshida, M., 2017. Trench dynamics: effects of dynamically migrating trench on subducting slab morphology and characteristics of subduction zones systems, *Phys. Earth planet. Inter.,* **268,** 35–53.

Yoshida, M. & Santosh, M., 2011. Supercontinents, mantle dynamics and plate tectonics: a perspective based on conceptual vs numerical models, *Earth Sci. Rev.,* **105**(1–2), 1–24.

Zhang, N., Dang, Z., Huang, C. & Li, Z.X., 2018. The dominant driving force for supercontinent breakup: plume push or subduction retreat?, *Geosci. Front.,* **9**(4), 997–1007.

Zhang, N., Zhong, S., Leng, W. & Li, Z.X., 2010. A model for the evolution of the Earth's mantle structure since the Early Paleozoic, *J. geophys. Res.,* **115**(B6), B06401.

Zhong, S., Zhang, N., Li, Z.X. & Roberts, J.H., 2007. Supercontinent cycles, true polar wander, and very long-wavelength mantle convection, *Earth planet. Sci. Lett.,* **261**(3–4), 551–564.

Ziegler, P.A. & Cloetingh, S., 2004. Dynamic processes controlling evolution of rifted basins, *Earth Sci. Rev.,* **64**(1–2), 1–50.

Ziegler, P.A. & Dèzes, P., 2007. Cenozoic uplift of Variscan Massifs in the Alpine foreland: timing and controlling mechanisms, *Global Planet. Change,* **58**(1–4), 237–269.

SUPPORTING INFORMATION

Supplementary data are available at *GJI* online.

Figure A1. Temporal evolution of model **1** (T_{init}: 1500 °C; d_{init}: 100 km; type of lithosphere: 'Variscan'; V_{ext}: 0 mm × yr^{-1}): (a) material phase field. Given its limited buoyancy, the mantle plume keeps its original circular configuration over the entire modelling time; (b) distribution of the temperatures (T); (c) temperature contrasts (ΔT). Black line in the panels 'b' and 'c' corresponds to an isotherm of 1300 °C which is, by definition, an equivalent of the LAB (see Methods).

Figure A2. Temporal evolution of model **3** (T_{init}: 1700 °C; d_{init}: 100 km; type of lithosphere: 'Variscan'; V_{ext}: 0 mm × yr^{-1}): (a) material phase field. A heart-like shape of the plume body at 15 Myr is further transformed into a quasi-elliptical configuration that remains unchanged since 60 Myr; (b) distribution of the temperatures (T); (c) temperature contrasts (ΔT).

Figure A3. Temporal evolution of the experiments characterized by T_{init} of 1500 °C and different d_{init}: (a) model **4** (d_{init}: 80 km; *); (b) model **1** (d_{init}: 100 km; *) and (c) model **7** (d_{init}: 116 km; *) represented by parameters derived from ΔT. Figure conventions as in Fig. 5. *Other experimental parameters: type of lithosphere: 'Variscan'; V_{ext}: 0 mm × yr^{-1}.

Figure A4. Temporal evolution of the experiments 1 characterized by T_{init} of 1700 °C and different d_{init}: (a) model **6** (d_{init}: 80 km; *); (b) model **3** (d_{init}: 100 km; *); and (c) model **9** (d_{init}: 116 km; *) represented by parameters derived from ΔT. Figure conventions as in Fig. 5. *Other experimental parameters: type of lithosphere: 'Variscan'; V_{ext}: 0 mm × yr^{-1}.

Figure A5. Temporal evolution of the experiments characterized by 'Cratonic' type of lithosphere and different T_{init} (a) model **10** (T_{init}: 1500 °C; *); (b) model **11** (T_{init}: 1600 °C; *); and (c) model **12** (T_{init}: 1700 °C; *) represented by parameters derived from ΔT. Figure conventions as in Fig. 5. *Other experimental parameters: d_{init}: 100 km; V_{ext}: 0 mm × yr^{-1}.

Figure A6. Temporal evolution of the experiments characterized by 'Mesozoic' type of lithosphere and different T_{init}: (a) model **13** (T_{init}: 1500 °C; *); (b) model **14** (T_{init}: 1600 °C; *); and (c) model **15** (T_{init}: 1700 °C; *) represented by parameters derived from ΔT. Figure conventions as in Fig. 5. *Other experimental parameters: d_{init}: 100 km; V_{ext}: 0 mm × yr^{-1}.

Figure A7. Temporal evolution of the experiments characterized by oceanic type of lithosphere and different T_{init}: (a) model **16** (T_{init}: 1500 °C; *); (b) model **17** (T_{init}: 1600 °C; *); and (c) model **18** (T_{init}: 1700 °C; *) represented by parameters derived from ΔT. Figure conventions as in Fig. 5. *Other experimental parameters: d_{init}: 100 km; V_{ext}: 0 mm × yr^{-1}.

Figure A8. Temporal evolution of model **19** (T_{init}: 1500 °C; type of lithosphere: 'Variscan'; V_{ext}: 2 mm × yr^{-1}; d_{init}: 100 km): (a) material phase field; (b) temperature contrasts (ΔT); (c) strain rate ($\dot{\varepsilon}$).

Figure A9. Temporal evolution of model **21** (T_{init}: 1700 °C; type of lithosphere: 'Variscan'; V_{ext}: 2 mm × yr^{-1}; d_{init}: 100 km): (a) material phase field; (b) temperature contrasts (ΔT); (c) strain rate ($\dot{\varepsilon}$).

Figure A10. Temporal evolution of the experiments characterized by T_{init} of 1500 °C, 'Variscan' type of lithosphere and different V_{ext}: (a) model **1** (V_{ext}: 0 mm × yr^{-1}; d_{init}: 100 km); (b) model **19** (V_{ext}: 2 mm × yr^{-1}; d_{init}: 100 km); and (c) model **22** (V_{ext}: 3 mm × yr^{-1}; d_{init}: 100 km) represented by parameters derived from ΔT. Figure conventions as in Fig. 5.

Figure A11. Temporal evolution of the experiments characterized by T_{init} of 1600 °C, 'Variscan' type of lithosphere and different V_{ext}: (a) model **2** (V_{ext}: 0 mm × yr^{-1}; d_{init}: 100 km); (b) model **20** (V_{ext}: 2 mm × yr^{-1}; d_{init}: 100 km); and (c) model **23** (V_{ext}: 3 mm × yr^{-1}; d_{init}: 100 km) represented by parameters derived from ΔT. Figure conventions as in Fig. 6.

Figure A12. Temporal evolution of the experiments characterized by T_{init} of 1700 °C, 'Variscan' type of lithosphere and different V_{ext}: (a) model **3** (V_{ext}: 0 mm × yr^{-1}; d_{init}: 100 km); (b) model **21** (V_{ext}: 2 mm × yr^{-1}; d_{init}: 100 km); and (c) model **24** (V_{ext}: 3 mm × yr^{-1}; d_{init}: 100 km) represented by parameters derived from ΔT. Figure conventions as in Fig. 5.